Dielectric, metallo-dielectric, and liquid crystal-infilled 2D photonic crystals: homogenization and tuning for in-plane and axial propagation.

By:

Jorge Antonio Reyes Avendaño

Thesis submitted in partial fulfillment of the requirements for the degree of

Doctor of Sciences in Electronics

in the

National Institute of Astrophysics, Optics and Electronics

Advisor:

Dr. Peter Halevi
Department of Electronics
INAOE

Abstract

This thesis is devoted to the study of two-dimensional photonic crystals in the long wavelength limit and to the tuning of their effective parameters. Using a very general mean field theory, the effective permittivity, permeability, and magnetoelectric dyadics are computed for several dielectric and metallo-dielectric structures. The results are in agreement with other theories in the literature and show an interesting magnetic behavior in structures made of metallic wires. In the special case of axial propagation, an extension to the general theory is presented. This extension allows to obtain the effective permittivity without requiring that the wave vector remain small as is required in the general theory. Nevertheless, it is important to say that the frequency must to remain small enough.

In this work it is also shown how the effective parameters can be tuned by using a liquid crystal as an element in the periodic structure. An external electric field can change the direction of the molecules of a nematic liquid crystal within the cylinders forming a photonic crystal, thus the effective parameters of the system are modified. Moreover, using a two-step homogenization process, is shown that, for sufficiently low frequencies, such a structure can be represented by two field-dependent effective refractive indices. It is demonstrate that the direction of the ordinary and extraordinary refracted rays can be sensitively tuned by varying the magnitude of the applied field.

The results presented in this thesis could pave the way to the design novel devices to control the flux of light. Moreover, the homogenization theory studied here is a powerful tool for the analysis of metamaterials which are a hot topic in the scientist community.

Resumen

Esta tesis está dedicada al estudio de cristales fotónicos bidimensionales en el límite de grandes longitudes de onda. Usando una teoría muy general de homogenización, los diádicos efectivos para la permitividad y permeabilidad, y los diádicos magneto-eléctricos son calculados para diversas estructuras dieléctricas y metalo-dieléctricas. Los resultados obtenidos están en acuerdo con otras teorías de homogenización en la literatura y muestran un comportamiento magnético muy interesante en estructuras de alambres metálicos. En el caso especial de la propagación axial, se presenta una extensión a la teoría general. Esta extensión permite calcular la permitividad efectiva sin la necesidad de restringir la magnitud del vector de la onda a valores pequeños como es requerido en la teoría general. Sin embargo, es importante decir que la frecuencia se debe mantener lo suficientemente pequeña para que el proceso de homogenización de resultados confiables.

En este trabajo de tesis también se muestra como usando un cristal líquido como parte de la estructura periódica se pueden sintonizar los parámetros efectivos. Un campo eléctrico externo puede cambiar la dirección de las moléculas de cristal líquido que se encuentran dentro de los cilindros que forman un cristal fotónico y en consecuencia, los parámetros efectivos del sistema son modificados. Además, usando un proceso de homogenización de dos pasos, se muestra que para frecuencias lo suficientemente bajas, tal estructura puede ser representada por dos índices de refracción que dependen del campo eléctrico. Se demuestra que la dirección de los haces refractados (ordinario y extraordinario) pueden ser modificados cuando se varia la magnitud del campo aplicado. Los resultados que se presentan en esta tesis pueden ser usados para el diseño de nuevos dispositivos destinados a controlar el flujo de la luz. Además, la teoría de homogenización que aquí se estudia es una herramienta poderosa para el análisis de metamateriales, los cuales son de gran interés para la comunidad científica.

Agradecimientos

A Conacyt.

A INAOE.

A mi asesor Dr. Peter Halevi por el apoyo brindado a los largo de estos años.

Dedicatorias

A mi esposa.

A mis padres.

A mis hermanos.

Preface

In 2004 my advisor gave me a copy in color of the cover article in Physics Today titled “Reversing Light With Negative Refraction” written by John B. Pendry and David R. Smith. In this paper the authors give an introduction to composite materials that give rise to negative refraction and show experimental results that confirm the prediction made by Victor Veselago 76 years before about the possibility of materials having a negative refractive index. This was my first reading about metamaterials and marked the start of this thesis. In the same year, in a workshop at INAOE, my advisor Dr. P. Halevi and Dr. F. Pérez-Rodríguez presented a homogenization theory that can be used to obtain the effective parameters of metamaterials. Because my master degree thesis was focused on the electrical tuning of bi-dimensional photonic crystals infilled with liquid crystals, it was natural to combine the new homogenization theory with the tuning effect achieved through the liquid crystal infiltration. Then, the subject of this thesis was defined as the study of two-dimensional photonic crystals by using a mean field theory as well as the tuning of the effective parameters by an external agent.

During the last six years I have been engaged in studies of two-dimensional photonic crystals in the long wavelength limit and in the tuning of the effective parameters involving liquid crystal infilling. As a result, with the exception of the Introduction and the Conclusions, every chapter in this thesis corresponds to one article written in collaboration with other authors: two are already published, one has been submitted, and the last one is in preparation. The articles that correspond to the second, third, fourth and fifth chapter are, respectively:

- J.A. Reyes-Avendaño, U. Algredo-Badillo, P. Halevi, and F. Pérez-Rodríguez, “From photonic crystals to metamaterials: the bi-anisotropic response”. (submitted to New J. Phys.)

- J.A. Reyes-Avendaño and P. Halevi, “Mean-field description of two-dimensional photonic crystals: Axial propagation.” (in preparation)

- Juan Adrian Reyes, J. A. Reyes-Avendaño, P. Halevi, “Electrical tuning of photonic crystals infilled with liquid crystals”, Opt. Comm., **281**, 2535(2008).
- J.A. Reyes-Avendaño and P. Halevi, “Electrical tuning of refraction in a two dimensional photonic crystal infilled with a liquid crystal”, Rev. Mex. Fís. **54**(6), 407-410(2008).

It is important to clarify that not all the results presented in chapters 2 and 4 correspond to this thesis, but have been included in order to give a complete description for each topic. In particular, in chapter 2 my contribution is limited to the computation of the effective parameters of two-dimensional photonic crystals and in chapter 4, the analysis of an infinite cylinder infilled with a nematic liquid crystal is not a result of my thesis.

Table of Contents

Abstract .... **iii**

Resumen .... **v**

Preface .... **xi**

CHAPTER 1 INTRODUCTION **1**

1.1 Photonic crystals **3**

1.2 Photonic crystals in the long-wavelength limit **5**

1.3 Tuning the optical properties **8**

1.4 Scope of the thesis **9**

CHAPTER 2 FROM PHOTONIC CRYSTALS TO METAMATERIALS: THE BI-ANISOTROPIC RESPONSE **11**

2.1 Introduction **12**

2.2 Mean-field theory **16**

2.3 Dielectric response **22**

2.4 Bi-anisotropic metamaterial response **24**

2.5 Dispersion relation of the homogenized medium **30**

2.6 Analytic results for special cases **30**
- 2.6.1 Generalities 31
  - *2.6.1.a Inversion Symmetry 31*
  - *2.6.1.b Cubic symmetry 32*
  - *2.6.1.c Mutually perpendicular mirror planes (2D photonic crystals) 33*

2.6.2 Specific systems 35

2.6.2.a Small spheres in a cubic lattice 35

2.6.2.b Cubic lattice of metallic wires 36

2.7 Numerical results 37

2.7.1 Two-dimensional dielectric cylinders 37

2.7.2 Three-dimensional dielectric spheres 38

2.7.3 Two-dimensional metallic wires 39

2.7.4 3D crosses of continuous and cut wires 43

2.7.5 Doubly negative (left-handed) behavior 48

2.8 Conclusion 50

CHAPTER 3 MEAN-FIELD DESCRIPTION OF TWO-DIMENSIONAL PHOTONIC CRYSTALS: AXIAL PROPAGATION. **53**

3.1 Introduction 54

3.2 Homogenization process 57

3.3 Numerical results 62

3.4 Comparison with experimental results 68

3.4 Conclusions 69

CHAPTER 4 ELECTRICAL TUNING OF PHOTONIC CRYSTALS INFILLED WITH LIQUID CRYSTALS **71**

4.1 Introduction 72

4.2 Model and basic equations for nematic liquid crystal cylinder 76

4.3 Nematic Configurations 79

4.4 Phase transition from escaped radial to the axial configuration 86

4.5 Photonic crystal composed of nematic liquid crystal cylinders 92

4.6 Approximate photonic band structure 102

4.7 Graphical results 104

4.8 Conclusions 107

CHAPTER 5 ELECTRICAL TUNING OF REFRACTION IN A TWO-DIMENSIONAL PHOTONIC CRYSTAL INFILLED WITH A LIQUID CRYSTAL **111**

5.1 Introduction........ 112

5.2 Homogenization process and tuning 113

5.3 Conclusions 119

CHAPTER 6 CONCLUSIONS **121**

APPENDIXES **127**

A Derivation of Eq. (2.25)........ 127

B Expansion of $\overleftrightarrow{\Sigma}(\mathbf{k})$ in powers of k........ 129

C Determination of $p = 1/2$ by imposing the Onsager symmetry relations........ 131

D Proof of Eq. (2.81) 132

E Proof of Eq. (2.84) 137

F Analysis of in-plane convergence 141

G Band structure computation for the axial propagation........ 143

H Analysis of convergence for the Γ bands........ 148

List of figures........ 155

List of tables 159

Resumen en extenso en español 161

List of references 171

Chapter 1

Introduction

The knowledge about how the electromagnetic waves (EWs) propagate in matter has played a fundamental role in the scientific advance. In different technological areas as telecommunications, aeronautics, medicine, optics or electronics –just for mention a few–, it is possible to find applications that have been developed or improved trough a deep understanding of the interaction between EWs and matter. In fact, because the EWs have an infinite spectral range, their study opens the door to an incommensurable number of possible applications.

Any theoretical study about the propagation of EWs is based on the solution of the set of four equations published in 1864 by James Clark Maxwell known as The Maxwell Equations [1]. These equations govern the propagation of EWs and in a macroscopic media and can be written as:

$$\nabla \cdot \mathbf{D} = \rho , \tag{1.1}$$

$$\nabla \cdot \mathbf{B} = 0 , \tag{1.2}$$

$$\nabla \times \mathbf{H} = \mathbf{J} + \frac{\partial \mathbf{D}}{\partial t} , \tag{1.3}$$

$$\nabla \times \mathbf{E} + \frac{\partial \mathbf{B}}{\partial t} = 0 . \tag{1.4}$$

Here **E**, **B**, **D** and **H** are the electric field, the magnetic induction, the displacement vector and the magnetic field respectively, ρ is the free charge density and **J** is the current density. In order to solve the Maxwell's Equations it is necessary to define the relations among the macroscopic fields. Such definitions are known as the constitutive relations and, in the most general case have the form [2]

$$\mathbf{D} = \overset{\leftrightarrow}{\boldsymbol{\varepsilon}} \cdot \mathbf{E} + \overset{\leftrightarrow}{\boldsymbol{\gamma}} \cdot \mathbf{H} , \tag{1.5}$$

$$\mathbf{B} = \overset{\leftrightarrow}{\boldsymbol{\delta}} \cdot \mathbf{E} + \overset{\leftrightarrow}{\boldsymbol{\mu}} \cdot \mathbf{H} , \tag{1.6}$$

where $\overset{\leftrightarrow}{\boldsymbol{\varepsilon}}$ is the electric permittivity dyadic, $\overset{\leftrightarrow}{\boldsymbol{\mu}}$ is the magnetic permeability dyadic, and, $\overset{\leftrightarrow}{\boldsymbol{\gamma}}$ and $\overset{\leftrightarrow}{\boldsymbol{\delta}}$ are the magneto-electric dyadics. These four parameters completely define the electromagnetic properties of the medium and depend in general on the wave vector and frequency of the EW that propagates. The value and characteristics of each dyadic can be obtained through experiments, numerically or in some cases analytically. Nowadays it is possible to design artificial materials with specific parameters, for example with a negative value of ε, or μ, or both. Another possibility is to obtain materials whose parameters are a periodic function in space. These materials are known as photonic crystals.

1.1 Photonic crystals

Photonic crystals (PCs) are artificial materials that offer the possibility of light control. Their principal characteristic is the periodicity in their structure which can be in one-, two-, or three-dimensions. They are built by the periodic repetition of a basic building block known as unit cell. The Fig. 1.1 shows simple forms of PCs for the three cases [3].

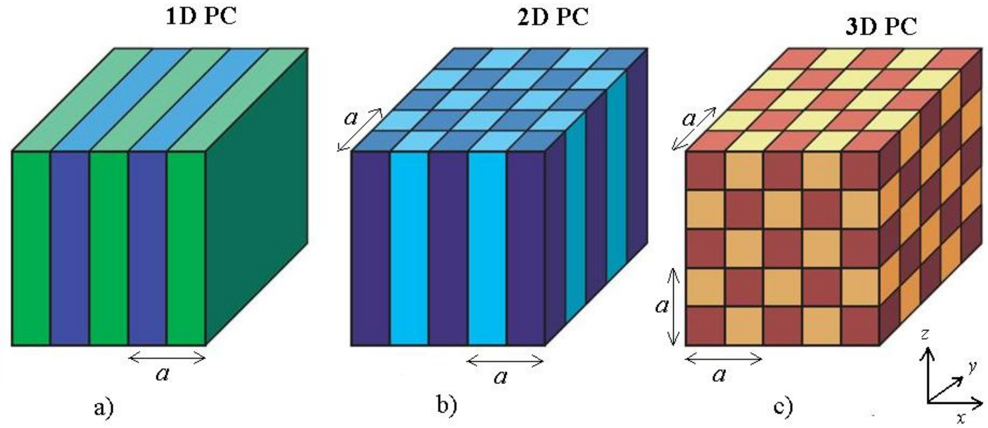

Fig. 1.1 Simple forms of photonic crystals. The arrow shows the unit cell of size *a*. Each color in the figure represents a different material.

Part a) in the figure shows a one-dimensional photonic crystal with periodicity in the *x* direction and uniformity in the *y* and *z* direction. The arrow indicates the length of the unit cell formed by 2 materials represented with different colors. A two-dimensional PC (part b) has periodicity in 2 directions (*x* and *y*) and translational invariance in the *z* direction. Finally, a three dimensional photonic crystal (part c) exhibits periodicity in all three directions. In these simple structures, the unit cell is formed by two materials, but in general, it can be constructed from many materials with a much more complicated unit cell.

PCs have received a lot of attention because with an appropriate selection of the materials and shape of the unit cell, it is possible to obtain a photonic band gap. This is a frequency region where the propagation of EWs through the structure is forbidden. As was mentioned before, the EW propagation is governed by the Maxwell Equations. Therefore, the calculation of photonic band gaps involves solving the Maxwell Equations for the PC. A common assumption in a photonic crystal is that the density of charge and the density of current are both zero and that he fields are proportional to *exp*(-*iωt*). With these assumptions and solving Eqs. (1.3) and (1.4) for the **E** the following wave equation is derived for the electric field:

$$\nabla \times \nabla \times \mathbf{E}(\mathbf{r}) = \frac{\omega^2}{c^2} \varepsilon(\mathbf{r}) \mathbf{E}(\mathbf{r}) . \tag{1.7}$$

Similar equations can be derived for the others fields. Here it is important to note that each material in the PC is assumed to be characterized by a scalar value of the permittivity, although it is possible to include materials with magnetic properties. The solutions of Eq. (1.7) give the modes that can propagate trough the PC. A usual form to render the solutions of Eq. (1.7) is called the band structure. For example, in Fig. 1.2 the band structure is presented for a triangular lattice of holes in a dielectric medium. This structure is studied in detail in Ref. [3] and it is important to note that there is a frequency region around the normalized frequency $\omega a/2\pi c = 0.47$ where no real solution of the Eq. (1.7) exist, corresponding to a band gap. Improved mirrors, wave guides, optical switches, and lasers [4-7], among other applications, have been developed taking advantage of this kind of structure possessing a photonic band gap.

A final observation must be underlined here. The photonic band gaps in dielectric structures appear in a frequency region where the wavelength λ is of the same order as the lattice constant *a*. In *dielectric* photonic crystals the propagation of electromagnetic waves is always allowed for the region of low frequencies where λ >> *a*.

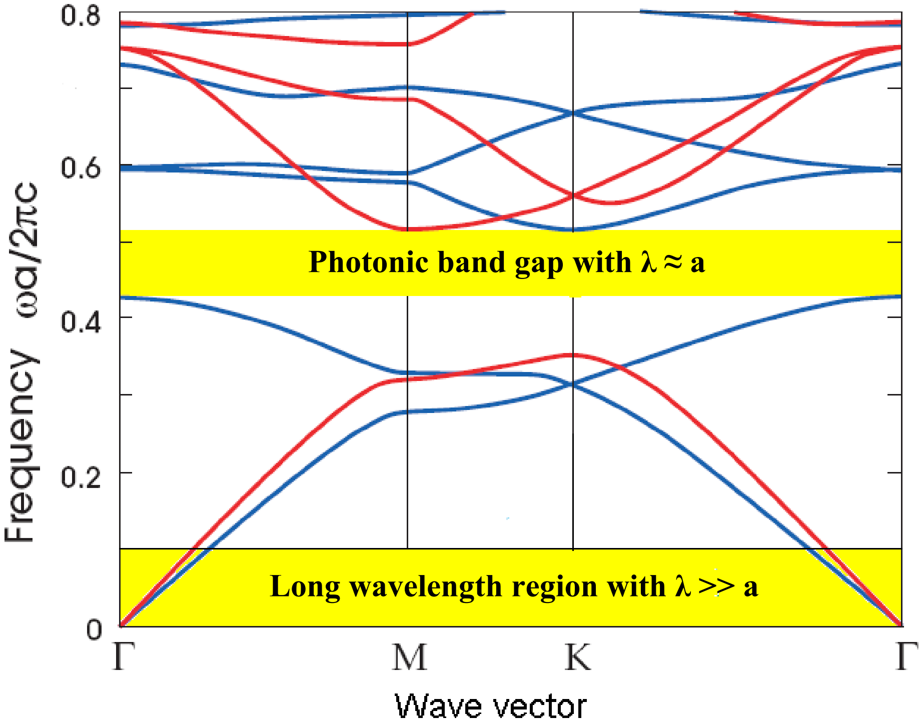

Fig. 1.2 Photonic band structure of a triangular lattices of circular holes in a dielectric medium (ε = 13) as in Ref. [3]. The structure posses a photonic band gap around the normalized frequency 0.47.In the figure the long wavelength region has been also shaded.

1.2 Photonic crystals in the long-wavelength limit

In the Fig. 1.2 the long wavelength region characterized by $\lambda >> a$ has been shaded. This condition has strong repercussions in the wave propagation. For instance, the electromagnetic wave is unable to "observe" the small details within the unit cell and perceives the photonic crystal as if it were homogeneous. This situation is illustrated in Fig 1.3. In part *a*, a three-dimensional photonic crystal is "observed" with a wavelength which is the same order as the lattice constant and it is possible to resolve the small details within the unit cell. In part *b*, the same PC is “observed” with a wavelength which is much larger than the lattice constant and the structure seems as if it were homogeneous. In consequence, the optical properties can be studied by using the effective parameters of the system, namely, the effective permittivity, the effective permeability, and the effective magneto electric dyadics [see Eqs. (1.5) and (1.6)].

In the long wavelength limit, PCs can be used as conventional optical devises such as lenses, prisms or polarizers but with characteristics designed by selecting the form and ingredients in the unit cell [8-10].

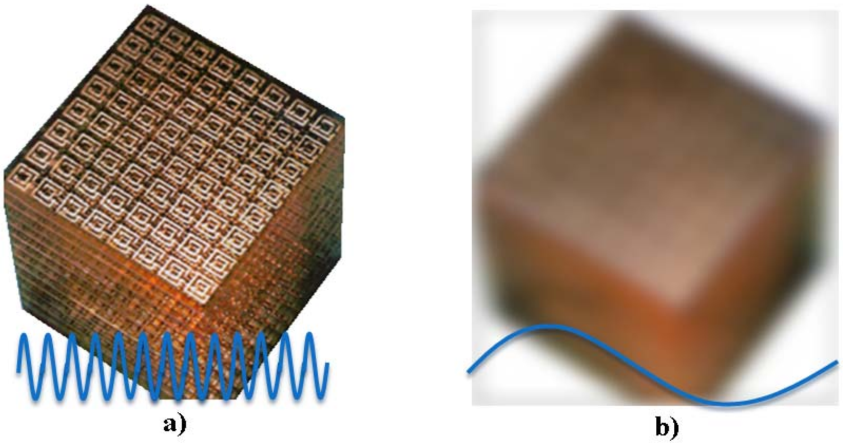

Fig. 1.3 Representation of the homogenization process. In part *a*, the PC is “observed” with a wavelength of the same order as the lattice constant and it is possible to see the small details. In part *b*, the same PC is observed with a long wavelength and the system seems to be homogeneous. Therefore can be represented by effective parameters.

In the recent years, the long wavelength limit has called the attention of the scientific community as a consequence of the experimental results published by Smith and collaborators [11-13]. They demonstrated that it is possible to fabricate an artificial composite possessing negative values of the permittivity and the permeability in the same range of frequencies and in consequence, a material having a negative effective refractive index. This frequency range has been found in the long wavelength region. A picture of the artificial material used in the experiment is shown in Fig. 1.4. The system is a combination of a two-dimensional photonic crystal of metallic wires and a three dimensional photonic crystal formed by the so-called split ring resonators [14].

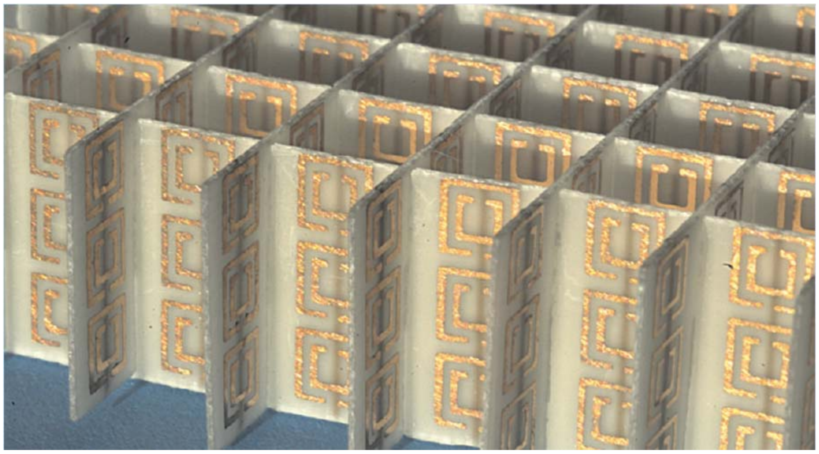

Fig. 1.4 Artificial material created by Smith and collaborators possessing a negative refractive index [14].

These new kinds of materials are usually called metamaterials because their properties are not found in nature. Their novel properties have been used to propose very interesting applications like a *perfect lens* which can overcome the diffraction limit of conventional lenses [15].

Now there emerges an important question: how to obtain the effective parameters of these novel structures? In the literature there can be found many different methods for this purpose. They can be classified in three main groups: experimental derivation, numerical methods and mean-field theories. In the experimental derivation the effective refractive index is obtained from transmission experiments [16, 17] but it has the disadvantage that it is necessary first to fabricate the sample. On the other side, there are numerous homogenization methods which are based in powerful numerical tools [18-22]. In these methods it is only necessary to define the components and the structure of the system, and then the software yields the results. Even though these are very convenient methods, they have the disadvantage that all the physical meaning is implicit and the interpretation can be incomplete. Finally, in the mean field theories the effective parameters are derived from first principles. These theories bring the possibility of a deep understanding about the physical origin of the effective parameters. Although there is a variety of mean field theories, most of them are focused in very specific systems or present problems of convergence in some cases [23-27].

1.3 Tuning the optical properties

Generally, once fabricated, the optical properties of a photonic crystal remain unchanged. Therefore, it is very convenient to obtain a *dynamic* structure whose optical properties can be changed by the action of an external agent. For example, this tuning effect can be used to open and close a photonic band gap, or to change the value of the effective parameters of the PC and change the refraction angle. The latter can be achieved by changing the PC's structure or by changing the properties of an ingredient material. For example, a structural change can be obtained by applying pressure to the system as has been proposed by Yoshino et al [28], or by incorporating a piezoelectric material in the init cell in order to induce a deformation, as in Ref. [29]. On the other hand, it is possible to build the photonic crystal using magnetic materials and then use an external magnetic field to modify the optical properties as was proposed by Figotin et al [30]. A similar approach has been suggested by Halevi and Ramos-Mendieta [31]. They proposed a PC with semiconductor constituents. An increment in the temperature change the free electron concentration and in consequence there is a change in the optical behavior of the structure. Another alternative to change the optical properties is to use a liquid crystal as an element in the system. It is well known that the liquid crystals possess strong sensibility to electric and magnetic fields as well as to change in the temperature. Therefore, all these external agents can be used to tune the optical properties. For example, Leonard et al [32] infiltrated a liquid crystal into the air pores of a 2D macroporous silicon PC. A strong tuning of the band edges was obtained by heating the sample. A similar approach was presented by Bush and John [33], who tuned the photonic band gap by applying an external electric field.

With very few exceptions [34-38], the studies of tuning have centered they attention on the photonic band gaps, developing devices like optical switches, or on polarizers. Nevertheless, in the long wavelength limit the tuning effect could lead many interesting applications.

In this thesis the tuning effect is explored in the long wavelength limit and also a novel electro-optic device is proposed with potential applications for ray steering, optical multiplexers, logic gates or switches. The system consists in a two-dimensional photonic crystal (PC) infilled by a liquid-crystal. Then, by applying a direct-current electric field, the angle of refraction is tuned in the long wavelength limit. The analysis of this structure requires two main studies: the homogenization process and the tuning of photonic crystals. Both areas have been studied in detail in this thesis.

1.4 Scope of the thesis

In chapter 2 is presented the very general homogenization process proposed by P. Halevi and F. Pérez-Rodríguez. This chapter also includes numerical results for dielectric and metallo-dielectric photonic crystals with periodicity in one-, two-, and three-dimensions. In this chapter, the propagation is restricted to directions of periodicity. This implies that, in the case of one-dimensional photonic crystals, only the axial propagation is considered, and in the case of two-dimensional photonic crystals, the study is restricted to in-plane propagation.

In chapter 3 the axial propagation of electromagnetic waves in the long-wavelength limit is studied in detail for two-dimensional photonic crystals. Using the same ideas presented in chapter 2 but taking into account the special behavior of the wave vector, the general formulas of homogenization are derived for the system. In addition, an analysis of the polarization is given for the first two bands. This analysis determines which element in the permittivity dyadic is involved in the wave propagation. Both, dielectric and metallo-dielectric structures are investigated.

Chapter 4 is devoted to the study of the electrical tuning of two dimensional photonic crystals infilled with liquid crystals. First is analyzed the configuration adopted by the molecules of the nematic liquid crystal 5CB within a single cylinder and their dependence with the external applied electric field. Then, this information is used to compute the photonic band structure for a specific magnitude of the external DC electric field.

In chapter 5 the homogenization process given in chapter 2 and 3 is employed, as well as the tuning effect showed in chapter 4 in order to obtain a novel system that can tune the angle of refraction by means of an external electric field. In addition, an alternative system of metallic wires surrounded by the nematic liquid crystal is analyzed. In this system, the optical properties can be switched by inducing a phase transition in the nematic liquid crystal by increasing the temperature.

Finally, the proof of several formulas in chapter 2, the general method used to compute the off-plane band structure and an analysis of convergence for the numerical results are given en several appendixes.

Chapter 2

From photonic crystals to metamaterials: the bi-anisotropic response

(MS with the same title by J.A. Reyes-Avendaño, U. Algredo-Badillo, P. Halevi, and F. Pérez-Rodríguez, submitted to New J. Phys.)

Metamaterials are usually characterized by the *bi-anisotropic response* $\mathbf{D} = \overleftrightarrow{\boldsymbol{\varepsilon}} \cdot \mathbf{E} + \overleftrightarrow{\boldsymbol{\gamma}} \cdot \mathbf{H}$, $\mathbf{B} = \overleftrightarrow{\boldsymbol{\delta}} \cdot \mathbf{E} + \overleftrightarrow{\boldsymbol{\mu}} \cdot \mathbf{H}$ that relates the displacement vector $\mathbf{D}$ and the magnetic induction $\mathbf{B}$ to the electric and magnetic fields $\mathbf{E}$ and $\mathbf{H}$ via the permittivity, permeability and the magnetoelectric dyadics, respectively $\overleftrightarrow{\boldsymbol{\varepsilon}}$, $\overleftrightarrow{\boldsymbol{\mu}}$, and $\overleftrightarrow{\boldsymbol{\gamma}}\,(= -\overleftrightarrow{\boldsymbol{\delta}}_T)$. For the first time, these dyadics have been derived with great generality from first principles, namely from the photonic crystal (PC) description. The PC can have one- (1D), two- (2D), or three-dimensional (3D) periodicity with arbitrary

Bravais lattice and arbitrary shape of the inclusions in the unit cell, and these inclusions can be dielectric or metallic. Moreover, unlike most theories of homogenization, our theory is applicable not only to “acoustic bands” with linear dispersion. The starting point is the generalized conductivity $\hat{\sigma}(\mathbf{r})$ at every point in the unit cell, and it relates $\overleftrightarrow{\boldsymbol{\varepsilon}}$, $\overleftrightarrow{\boldsymbol{\mu}}$ and $\overleftrightarrow{\boldsymbol{\gamma}}$ analytically to $\hat{\sigma}(\mathbf{r})$. The long wavelength limit having been taken, these dyadics depend only on the direction of the Bloch wave vector $\mathbf{k}$, not however of its magnitude. In case of inversion symmetry, the bi-anisotropic response simplifies to $\mathbf{D} = \overleftrightarrow{\boldsymbol{\varepsilon}} \cdot \mathbf{E}$, $\mathbf{B} = \overleftrightarrow{\boldsymbol{\mu}} \cdot \mathbf{H}$. Applying this theory to a 2D array of metallic wires, shows that the response is paramagnetic or diamagnetic, depending on whether it is the electric or the magnetic field that is parallel to the wires. For a 3D array of mutually perpendicular wires (3D crosses), the behavior is found to change from plasma-like to free-photon-like when the wires are severed, leading to a spectral region where ε and μ are both negative. Finally, this theory confirms several well known results for particular PCs and inclusions.

2.1 Introduction

During the last 30 years, photonic crystals (PC’s) have been intensively studied because they offer the possibility of light control [3]. The way in which these artificial periodic structures interact with an electromagnetic wave strongly depends on the ratio between the lattice constant a and the electromagnetic wavelength λ. When $\lambda \lessapprox a$, light traveling through the PC experiences strongly the dielectric contrast between the different materials forming the periodic structure, in the same way as electrons “feel” the periodic potential in a semiconductor crystal. For sufficiently strong dielectric contrast and appropriate choice of geometric parameters, it is possible to obtain artificial materials possessing a frequency region in which the light cannot propagate through the structure. This region is usually called photonic band gap (PBG). Improved mirrors, wave guides, optical switches, and lasers [4-7], among other applications, have been developed taking advantage of this PBG region. On the other hand, when $\lambda \gg a$, another situation is observed. Long wavelength light traveling through the structure does not experience the details of the structure of the artificial material and the PC behaves as if it were homogeneous. Therefore, the optical properties can be well described by employing Maxwell’s Equations for the average electromagnetic fields together with macroscopic constitutive relations [1, 39]. In this frequency region (long-wavelength limit) PCs are used as conventional optical devices like lenses, prisms, or polarizers but with unusual behaviors. The properties of PCs can be custom tailored by suitable selection of their parameters [8-10].

Since Smith and collaborators [11-13] demonstrated the existence of arrays of conducting elements possessing a negative effective refractive index (corresponding to negative permittivity and negative permeability in the same range of frequency) the number of papers dealing with PCs in the long-wavelength limit has undergone exponential growth. The idea of negative refraction has a very interesting history, recently reviewed by Agranovich and Gartstein [40]. It goes back to the mention of such a possibility by Schuster [41] in 1909 and a thorough analysis by Mandel'shtam [42] in 1945, also published later in book form [43]. More recently, negative refraction was discussed by Sivukhin [44] and by Pafomov [45-47], to be finally rediscovered by Veselago [48]. Many years later, Pendry and collaborators [49, 50] showed that negative-index materials are viable in practice. New kinds of materials, called *metamaterials*, opened the door to a wholly new field in optics, where Snell’s law applies with a negative index of refraction. Consequently, many efforts have been devoted to developing theoretical and numerical methods that can predict the effective permittivity, permeability, etc. of metamaterials, leading to convenience in understanding and design of these interesting structures.

Numerous works are dedicated to mean-field theories for selected types of PCs, using miscellaneous approximations, such as the Lorentz approach [51], the Clausius-

Mosotti method [52], the Maxwell Garnett approximation [53], the spectral representation method [54], and transmission line studies [55]. Further, several homogenization theories have focused on arbitrary dielectric [10, 23-25] or metallic [26, 27] inclusions in the long-wavelength limit. The aforementioned homogenization theories all limit the generality to one or more of the following aspects: the form of the inclusion, type of material, filling fraction, and photonic band.

Also available are two approaches to homogenization that are of much wider generality: the effective parameter retrieval (EPR) method and the field averaging (FA) method. The EPR method [18-20] determines the effective parameters, $\varepsilon(\omega)$ and $\mu(\omega)$, by requiring that the scattering spectra of an inhomogeneous medium slab coincide with those of the corresponding homogeneous medium. On the other hand, the FA method is based on the averaging of the PC's electromagnetic fields in a unit cell. Initiated by Pendry and collaborators, it has been inspired by finite-difference solutions of Maxwell's Equations [21, 22, 50]. Both, the EPR method and the FA method, are numerical methods for the determination of effective parameters, rather than mean-field (homogenization) theories. An approach similar to FA has been used by Silveirinha and Fernandes [56-58] for the case of wire media. More recently, Silveirinha [59] has proposed a source-driven approach to homogenization, leading to an integral equation that can be solved in closed form for the effective dielectric tensor $\ddot{\boldsymbol{\varepsilon}}(\mathbf{k})$. This led to generalized Lorentz-Lorenz formulas [60] and to numerical implementation (by a finite-difference frequency-domain method) of the aforementioned approach [61]. We also note that homogenization theories are available for non-periodic (random) media as well [62-64]. The very general dielectric homogenization theory by Mochan and Barrera [64] was recently adapted to periodic PCs [65]. In the latter paper by Ortiz et al. [65] the effective dielectric tensor is derived by a method of projection operators. We note that the expressions for $\ddot{\boldsymbol{\varepsilon}}(\mathbf{k})$ in the refs. 59 and 65 are equivalent to this work for the *dielectric response*, rather than the *bi-anisotropic* response. The latter response was also studied by a numerical current-driven approach [66].

There exist, in principle, many ways for defining the effective parameters by suitably relating the macroscopic constitutive fields, namely the dielectric displacement **D** and the magnetic field **H**, to the physical macroscopic fields, namely the electric field **E** and the magnetic induction **B**. Perhaps the most general linear constitutive relation is the so-called bi-anisotropic response [2, 20, 62, 67-69],

$$\mathbf{D} = \overleftrightarrow{\boldsymbol{\varepsilon}}\cdot\mathbf{E} + \overleftrightarrow{\boldsymbol{\gamma}}\cdot\mathbf{H}, \quad \mathbf{B} = \overleftrightarrow{\boldsymbol{\delta}}\cdot\mathbf{E} + \overleftrightarrow{\boldsymbol{\mu}}\cdot\mathbf{H}\,.$$

On the other hand, in nominally nonmagnetic media (especially in Solid State Physics and in Crystal Optics) it is common to take into account *small* magnetic effects by employing only a *non-local* effective dielectric tensor $\overleftrightarrow{\boldsymbol{\varepsilon}}(\mathbf{k})$ [63, 67, 70-72]:

$$\mathbf{D} = \overleftrightarrow{\boldsymbol{\varepsilon}}(\mathbf{k})\cdot\mathbf{E}, \quad \mathbf{B} = \mu_0\mathbf{H}\,.$$

These magnetic effects being small –unlike the usual situation with metamaterials– it is convenient to “hide” them in the wavevector dependence of the effective dielectric tensor. Furthermore, because of the smallness of the ratio a/λ, the effects of spatial dispersion, which can be associated with the magnetic field, turn out to be rather weak.

In this work we present a mean-field theory of PCs which goes beyond conventional ones. This is a theory for an unbounded PC, abstraction made in the tradition of Crystal Optics theories for a bulk medium [70]. By assuming that the Bloch wavelength is much greater than the lattice constant of the periodic artificial structure, are derived analytic results for the effective tensors of both the bi-anisotropic response $(\overleftrightarrow{\boldsymbol{\varepsilon}},\ \overleftrightarrow{\boldsymbol{\gamma}},\ \overleftrightarrow{\boldsymbol{\delta}},\ \overleftrightarrow{\boldsymbol{\mu}})$ and for the nonlocal dielectric response $(\overleftrightarrow{\boldsymbol{\varepsilon}}(\mathbf{k}))$. These are determined for arbitrary periodicity (1D, 2D, and 3D) of the PC, for an arbitrary Bravais lattice, and for arbitrary structure of the unit cell. Considering isotropic and nonmagnetic materials in the unit cell of the photonic crystal, it is shown that the use of the bi-anisotropic response allows to distinguish clearly the magnetic effects and, consequently, to characterize more properly the electromagnetic metamaterial properties. This chapter derives the bi-anisotropic response from the PC or "micro-level", for the first time on the basis of a very general set of assumptions. The effective permittivity and permeability for specific dielectric and metallo-dielectic photonic crystals are calculated, analyzed and, in some cases compared with other theories in the literature.

The chapter is organized as follows. In Sec. 2.2 we describe the general approach to homogenization, from which both the dielectric response (Sec. 2.3) and the bianisotropic response (Sec. 2.4) are derived. In Sec. 2.5 is presented the corresponding dispersion relation for the homogenized medium. Sec. 2.6 is devoted to the analysis of some important special cases in which the general formulas are simplified and reduced to analytical results. In Sec. 2.7 we give numerical results for two simple systems that are compared with other work and also present the effective permittivity and permeability spectra for a few metallo-dielectric structures that present metamaterial behavior. The conclusions are given in Sec. 2.8. Finally, the proofs of several formulas and a study of convergence have been relegated to the appendices.

2.2 Mean-field theory

Lets to consider a boundless photonic crystal (PC) composed, in general, of metallic and dielectric components. The form of the inclusions in the unit cell and the Bravais lattice are assumed to be completely arbitrary. Besides, the inclusions can be either isolated or in contact. For simplicity, is also assumed that the component materials are isotropic and that the metal has no magnetic properties. Such a photonic crystal can be described by only a single material scalar field, namely the position-dependent generalized conductivity:

$$\hat{\sigma}(\mathbf{r}) = \sigma(\mathbf{r}) - i\omega\varepsilon_0\chi(\mathbf{r}), \qquad (2.1)$$

having the same periodicity as the PC. $\sigma(\mathbf{r})$ and $\chi(\mathbf{r})$ in Eq. (2.1) are, correspondingly, the usual conductivity and susceptibility for isotropic materials in the unit cell. In Eq. (2.1) a metallic component is usually characterized by $\chi(\mathbf{r}) = 0$, while a dielectric component is described by $\sigma(\mathbf{r}) = 0$. For vacuum both $\sigma(\mathbf{r})$ and $\chi(\mathbf{r})$ vanish, thus $\hat{\sigma}(\mathbf{r}) = 0$. Hence, this description covers both metallo-dielectric and dielectric PCs. In the following the term "micro-level" is used to define the PC level of description in which the inhomogeneous medium is described by the position-dependent conductivity Eq. (2.1). On the other hand, the term "macro-level" is used in the long wavelength limit, when the structure is described by position-independent effective parameters. The macro-level thus corresponds to an effectively uniform –but not necessarily isotropic– medium, called "metamaterial" if possessing unusual properties.

The electromagnetic fields inside the PC are governed by Maxwell's Equations at the "micro-level" which, according to the later assumptions, can be written in the form:

$$\nabla \times \mathbf{b}(\mathbf{r}) = \mu_0 \mathbf{j}(\mathbf{r}) - \mu_0 i\omega\varepsilon_0 \mathbf{e}(\mathbf{r}), \qquad (2.2)$$

$$\nabla \cdot \mathbf{e}(\mathbf{r}) = -\frac{i}{\varepsilon_0 \omega} \nabla \cdot \mathbf{j}(\mathbf{r}), \qquad (2.3)$$

$$\nabla \times \mathbf{e}(\mathbf{r}) = i\omega \mathbf{b}(\mathbf{r}), \qquad (2.4)$$

$$\nabla \cdot \mathbf{b}(\mathbf{r}) = 0 . \tag{2.5}$$

Here, the requirement of charge conservation $(i\omega\rho = \nabla \cdot \mathbf{j})$ has been used, the fields are proportional to, $\exp(-i\omega t)$ MKS units are employed, and the current density $\mathbf{j}$ is

$$\mathbf{j}(\mathbf{r}) = \hat{\sigma}(\mathbf{r})\mathbf{e}(\mathbf{r}) . \tag{2.6}$$

By Eq.(2.6), this current density is produced by the electric field $\mathbf{e}(\mathbf{r})$ of the PC which, in turn, is supposed to be the consequence of some virtual, unspecified excitation.

Because of the periodicity, the generalized conductivity can be expanded in a Fourier series,

$$\hat{\sigma}(\mathbf{r}) = \sum_{\mathbf{G}} \hat{\sigma}(\mathbf{G}) e^{i\mathbf{G}\cdot\mathbf{r}} , \tag{2.7}$$

and the “micro-level” fields $\mathbf{e}(\mathbf{r})$ and $\mathbf{b}(\mathbf{r})$ obey the Bloch theorem. Hence,

$$\mathbf{e}(\mathbf{r}) = \sum_{\mathbf{G}} \mathbf{e}(\mathbf{G}) e^{i(\mathbf{k}+\mathbf{G})\cdot\mathbf{r}} = \mathbf{e}(\mathbf{G}=0) e^{i\mathbf{k}\cdot\mathbf{r}} + \sum_{\mathbf{G}}{}' \, \mathbf{e}(\mathbf{G}) e^{i(\mathbf{k}+\mathbf{G})\cdot\mathbf{r}} , \tag{2.8}$$

$$\mathbf{b}(\mathbf{r}) = \sum_{\mathbf{G}} \mathbf{b}(\mathbf{G}) e^{i(\mathbf{k}+\mathbf{G})\cdot\mathbf{r}} = \mathbf{b}(\mathbf{G}=0) e^{i\mathbf{k}\cdot\mathbf{r}} + \sum_{\mathbf{G}}{}' \, \mathbf{b}(\mathbf{G}) e^{i(\mathbf{k}+\mathbf{G})\cdot\mathbf{r}} , \tag{2.9}$$

where the primes indicate that the term with $\mathbf{G} = 0$ is excluded from the sums. Here $\mathbf{k}$ is the Bloch wave vector, which is the only wave vector characterizing the propagation.

For Bloch wavelengths $2\pi/k$ much larger than the lattice constant *a*,

$$ka \ll 1, \tag{2.10}$$

in the case of 3D periodicity the “macro-level” electric field **E**(r) and magnetic induction **B**(r) can be obtained by averaging the micro-level fields **e**(r) (Eq. (2.8)) and **b**(r) (Eq. (2.9)) over a spherical volume of radius *R* much larger than *a*, but much smaller than the wavelength $2\pi/k$ $(a \ll R \ll 2\pi/k)$. This averaging procedure smooths out the rapid oscillations of the micro-level fields inside the volume of the chosen radius *R*. The rapid oscillations are described by the terms with $\mathbf{G} \neq 0$ in Eqs. (2.8) and (2.9). Therefore,

$$\mathbf{E}(\mathbf{r}) \equiv \left\langle \mathbf{e}(\mathbf{r}) \right\rangle = \mathbf{e}(\mathbf{G}=0)e^{i\mathbf{k}\cdot\mathbf{r}} = \mathbf{E}_0 e^{i\mathbf{k}\cdot\mathbf{r}}, \tag{2.11}$$

$$\mathbf{B}(\mathbf{r}) \equiv \left\langle \mathbf{b}(\mathbf{r}) \right\rangle = \mathbf{b}(\mathbf{G}=0)e^{i\mathbf{k}\cdot\mathbf{r}} = \mathbf{B}_0 e^{i\mathbf{k}\cdot\mathbf{r}}, \tag{2.12}$$

where <…> indicates the volumetric averaging. In the case of 2D (1D) periodicity the averaging is performed within a circle (segment). It is significant that, as consequence of our averaging procedure, the Bloch wave vector became the ordinary wave vector of a plane wave in Eqs. (2.11) and (2.12).

The Maxwell Equations for the fields at the macro-level are derived by averaging the micro-level Eqs. (2.2)-(2.5). We get

$$\mathbf{k} \times \mathbf{B} = -i\mu_0 \left\langle \mathbf{j} \right\rangle - \mu_0 \omega \varepsilon_0 \mathbf{E}, \tag{2.13}$$

$$\mathbf{k} \cdot \mathbf{E} = -\frac{i}{\varepsilon_0 \omega} \mathbf{k} \cdot \left\langle \mathbf{j} \right\rangle, \tag{2.14}$$

$$\mathbf{k} \times \mathbf{E} = \omega \mathbf{B} , \tag{2.15}$$

$$\mathbf{k} \cdot \mathbf{B} = 0 . \tag{2.16}$$

In obtaining the Eqs. (2.13)-(2.16), is took into account the fact that the derivatives and the averaging commute [1, 39].

Now, in order to determine the material equation for the homogenized photonic crystal, it is necessary to establish the relation between the macroscopic current density $\langle \mathbf{j} \rangle = \mathbf{j}_0 \exp(i\mathbf{k} \cdot \mathbf{r})$ and the electric field $\mathbf{E}(\mathbf{r})$ (Eq. (2.11)). As follows from Eqs. (2.6) and (2.7), the amplitude $\mathbf{j}_0$ can be written as

$$\mathbf{j}_0 = \hat{\sigma}(\mathbf{G}=0)\mathbf{e}(\mathbf{G}=0) + \sum_{\mathbf{G}}{}' \hat{\sigma}(-\mathbf{G})\mathbf{e}(\mathbf{G}) . \tag{2.17}$$

To express the quantities $\mathbf{e}(\mathbf{G} \neq 0)$ in terms of, $\mathbf{e}(\mathbf{G}=0)$ is used the wave equation

$$\nabla \times \nabla \times \mathbf{e}(\mathbf{r}) = \left[i\mu_0 \omega \hat{\sigma}(\mathbf{r}) + k_0^2 \right] \mathbf{e}(\mathbf{r}) , \tag{2.18}$$

which is obtained by eliminating the magnetic induction $\mathbf{b}(\mathbf{r})$ from de Ampére-Maxwell law Eq. (2.2) and Faraday's law Eq. (2.4) with $k_0^2 = \mu_0 \varepsilon_0 \omega^2$. Afterwards, it is necessary to substitute the Eqs. (2.8) and (2.7) into Eq. (2.18) and finally get

$$(\mathbf{k}+\mathbf{G}) \times (\mathbf{k}+\mathbf{G}) \times \mathbf{e}(\mathbf{G}) + k_0^2 \mathbf{e}(\mathbf{G}) = -i\omega\mu_0 \sum_{\mathbf{G}'} \hat{\sigma}(\mathbf{G}-\mathbf{G}')\mathbf{e}(\mathbf{G}') . \tag{2.19}$$

This equation can be rewritten in dyadic notation as

$$\sum_{\mathbf{G}'}{}^{'}\overleftrightarrow{\mathbf{M}}(\mathbf{k};\mathbf{G},\mathbf{G}')\cdot\mathbf{e}(\mathbf{G}')=i\omega\mu_0\hat{\sigma}(\mathbf{G})\mathbf{e}(0),\quad \mathbf{G}\neq 0\,, \tag{2.20}$$

where the dyadic $\overleftrightarrow{\mathbf{M}}(\mathbf{k};\mathbf{G},\mathbf{G}')$ is defined for $\mathbf{G}\neq 0$ and $\mathbf{G}'\neq 0$ as

$$\overleftrightarrow{\mathbf{M}}(\mathbf{k};\mathbf{G},\mathbf{G}')=\left[\left(\left|\mathbf{k}+\mathbf{G}\right|^2-k_0^2\right)\overleftrightarrow{\mathbf{I}}-\left(\mathbf{k}+\mathbf{G}\right)\left(\mathbf{k}+\mathbf{G}\right)\right]\delta_{\mathbf{G},\mathbf{G}'}-i\omega\mu_0\hat{\sigma}(\mathbf{G}-\mathbf{G}')\overleftrightarrow{\mathbf{I}}\;. \tag{2.21}$$

Here, $\overleftrightarrow{\mathbf{I}}$ and $\delta_{\mathbf{G},\mathbf{G}'}$ are, respectively, the unit dyadic and the Kronecker delta. Solving Eq. (2.20) for $\mathbf{e}(\mathbf{G}\neq 0)$, is found the expression

$$\mathbf{e}(\mathbf{G})=i\omega\mu_0\sum_{\mathbf{G}'}{}^{'}\overleftrightarrow{\mathbf{M}}^{-1}(\mathbf{k};\mathbf{G},\mathbf{G}')\hat{\sigma}(\mathbf{G}')\cdot\mathbf{e}(0),\quad \mathbf{G}\neq 0\,. \tag{2.22}$$

After substituting this expression into Eq. (2.17), is finally obtained the macroscopic current density in the form

$$\mathbf{j}_0=\overleftrightarrow{\mathbf{\Sigma}}(\mathbf{k})\cdot\mathbf{E}_0\,, \tag{2.23}$$

where $\overleftrightarrow{\mathbf{\Sigma}}(\mathbf{k})$ is the effective conductivity dyadic:

$$\overleftrightarrow{\mathbf{\Sigma}}(\mathbf{k})=\hat{\sigma}(\mathbf{G}=0)\overleftrightarrow{\mathbf{I}}+i\omega\mu_0\sum_{\mathbf{G},\mathbf{G}'}{}^{'}\hat{\sigma}(-\mathbf{G})\overleftrightarrow{\mathbf{M}}^{-1}(\mathbf{k};\mathbf{G},\mathbf{G}')\hat{\sigma}(\mathbf{G}')\,. \tag{2.24}$$

It is also possible to derive an equivalent formula for $\overleftrightarrow{\mathbf{\Sigma}}(\mathbf{k})$ which can be written as:

$$\overleftrightarrow{\mathbf{\Sigma}}(\mathbf{k})=\frac{i}{\omega\mu_0}\left[\left\{\overleftrightarrow{\mathbf{N}}^{-1}(\mathbf{k};0,0)\right\}^{-1}-\left(k^2-k_0^2\right)\overleftrightarrow{\mathbf{I}}+\mathbf{k}\mathbf{k}\right], \tag{2.25}$$

where $\overleftrightarrow{\mathbf{N}}(\mathbf{k};\mathbf{G},\mathbf{G}')$ is given by Eq. (2.21) $\left(\overleftrightarrow{\mathbf{N}}(\mathbf{k};\mathbf{G},\mathbf{G}') = \overleftrightarrow{\mathbf{M}}(\mathbf{k};\mathbf{G},\mathbf{G}')\right)$, now however $\mathbf{G}$ and $\mathbf{G}'$ range over all the vectors of the reciprocal lattice (i.e., including $\mathbf{G} = 0$ and $\mathbf{G}' = 0$). The last equation may result more convenient from the computational point of view because the double sum in Eq. (2.24) is avoided and only one 3×3 matrix block of the inverse matrix $\overleftrightarrow{\mathbf{N}}^{-1}(\mathbf{k};\mathbf{G},\mathbf{G}')$ must be obtained. The derivation of Eq. (2.25) is given in Appendix A.

Employing Eq. (2.24) or Eq. (2.25), substitution of Eq. (2.23) in the Maxwell's Equations (2.13)-(2.16) gives

$$\mathbf{k} \times \mathbf{B}_0 = -\mu_0 \left[\omega\varepsilon_0 \overleftrightarrow{\mathbf{I}} + i\overleftrightarrow{\mathbf{\Sigma}}(\mathbf{k}) \right] \cdot \mathbf{E}_0 , \tag{2.26}$$

$$\mathbf{k} \cdot \left[\omega\varepsilon_0 \overleftrightarrow{\mathbf{I}} + i\overleftrightarrow{\mathbf{\Sigma}}(\mathbf{k}) \right] \cdot \mathbf{E}_0 = 0 , \tag{2.27}$$

$$\mathbf{k} \times \mathbf{E}_0 = \omega \mathbf{B}_0 , \tag{2.28}$$

$$\mathbf{k} \cdot \mathbf{B}_0 = 0 . \tag{2.29}$$

2.3 Dielectric response

A very convenient way to determine the effective material response is to compare the average Maxwell Equations, derived in the preceding section (see Eqs. (2.26)-(2.29)), with the corresponding equations for a macroscopic homogeneous medium:

$$\mathbf{k} \times \mathbf{H} = -\omega \mathbf{D} , \tag{2.30}$$

$$\mathbf{k} \cdot \mathbf{D} = 0 , \tag{2.31}$$

$$\mathbf{k} \times \mathbf{E} = \omega \mathbf{B} , \tag{2.32}$$

$$\mathbf{k} \cdot \mathbf{B} = 0 . \tag{2.33}$$

So, it should define a relation between the auxiliary fields **D** and **H** and the physical fields **E** and **B**. However, the form of the material response is *not* unique. One of the possibilities is to write the constitutive relations as [39, 70-72]:

$$\mathbf{D} = \overset{\leftrightarrow}{\boldsymbol{\varepsilon}}(\mathbf{k}, \omega) \cdot \mathbf{E} , \tag{2.34}$$

$$\mathbf{B} = \mu_0 \mathbf{H} . \tag{2.35}$$

This choice, evidently, does not take into account explicitly magnetic effects. The electromagnetic properties of the homogeneous material depend only on the form of the wave vector-dependent, in general, dielectric dyadic $\overset{\leftrightarrow}{\boldsymbol{\varepsilon}}(\mathbf{k}, \omega)$. If are substituted the Eqs. (2.34) and (2.35) in the Eqs. (2.30) and (2.31), comparison with the Eqs. (2.26) and (2.27) shows that this dyadic is

$$\overset{\leftrightarrow}{\boldsymbol{\varepsilon}}(\mathbf{k}, \omega) = \varepsilon_0 \overset{\leftrightarrow}{\mathbf{I}} + \frac{i}{\omega} \overset{\leftrightarrow}{\boldsymbol{\Sigma}}(\mathbf{k}, \omega) \tag{2.36}$$

with $\overset{\leftrightarrow}{\boldsymbol{\Sigma}}(\mathbf{k}, \omega)$ given by the Eqs. (2.24) and (2.21).

Now, although the derivation from Eq. (2.17) to Eq. (2.24) does not involve any approximation, this mean-field approach relies on the smallness of k, namely Eq. (2.10). For this reason, it makes sense to expand $\overset{\leftrightarrow}{\boldsymbol{\Sigma}}(\mathbf{k}, \omega)$ in powers of the small parameter ka:

$$\overset{\leftrightarrow}{\mathbf{\Sigma}}(\mathbf{k}) = \overset{\leftrightarrow}{\mathbf{\Sigma}}^{(0)} + k\overset{\leftrightarrow}{\mathbf{\Sigma}}^{(1)}(\hat{\mathbf{k}}) + k^2\overset{\leftrightarrow}{\mathbf{\Sigma}}^{(2)}(\hat{\mathbf{k}}) + \cdots \tag{2.37}$$

Note that the dyadics $\overset{\leftrightarrow}{\mathbf{\Sigma}}^{(1)}$ and $\overset{\leftrightarrow}{\mathbf{\Sigma}}^{(2)}$, although independent of the magnitude of $\mathbf{k}$, do depend on its direction, namely on the unit vector $\hat{\mathbf{k}} = \mathbf{k}/k$. As for the frequency ω, which is regarded independent of $\mathbf{k}$ in expanding $\overset{\leftrightarrow}{\mathbf{\Sigma}}(\mathbf{k},\omega)$ (2.37), it must also be small enough ($\omega << 2\pi c/a$).

In the next section will be derived the effective conductivity dyadic $\overset{\leftrightarrow}{\mathbf{\Sigma}}(\mathbf{k},\omega)$ (2.24) in the quadratic approximation, Eq. (2.37). This of course, also determines the dielectric tensor $\overset{\leftrightarrow}{\boldsymbol{\varepsilon}}(\mathbf{k},\omega)$ (Eq.(2.36) of the dielectric response in the same order of $\mathbf{k}$. In particular, in the long-wavelength limit, the resulting expression $\overset{\leftrightarrow}{\boldsymbol{\varepsilon}}(\mathbf{k} \to 0, \omega \to 0)$ from the later formulas, correctly yields the effective dielectric function, calculated previously for 3D [24] and 2D [10, 25] dielectric PCs. Besides, the expression obtained here for the effective permittivity tensor $\overset{\leftrightarrow}{\boldsymbol{\varepsilon}}(\mathbf{k},\omega)$ is consistent with the results of Ref. [69] in the case of nonmagnetic dielectric PCs. The dyadic $\overset{\leftrightarrow}{\mathbf{\Sigma}}$ will also lead us to relate the bi-anisotropic response to the PC "micro-level".

2.4 Bi-anisotropic response

There exists another form, called bianisotropic, for expressing the material response of the homogenized material. The bianisotropic response establishes the relation between D, H, E and B, by employing four dyadics:

$$\mathbf{D} = \overset{\leftrightarrow}{\boldsymbol{\varepsilon}} \cdot \mathbf{E} + \overset{\leftrightarrow}{\boldsymbol{\gamma}} \cdot \mathbf{H}, \tag{2.38}$$

$$\mathbf{B} = \overset{\leftrightarrow}{\boldsymbol{\delta}} \cdot \mathbf{E} + \overset{\leftrightarrow}{\boldsymbol{\mu}} \cdot \mathbf{H}. \tag{2.39}$$

Here, $\overleftrightarrow{\boldsymbol{\varepsilon}}$ is the permittivity, $\overleftrightarrow{\boldsymbol{\mu}}$ is the permeability, and $\overleftrightarrow{\boldsymbol{\gamma}}$ and $\overleftrightarrow{\boldsymbol{\delta}}$ are the “crossed” magneto-electric dyadics.

To derive the bi-anisotropic material response in the long wavelength limit, it is necessary to use the expansion of the effective conductivity dyadic $\overleftrightarrow{\boldsymbol{\Sigma}}(\mathbf{k})$, Eq. (2.37). Below, are considered only the first three terms of Eq. (2.37). By Eq. (2.24), the zero-order term is

$$\overleftrightarrow{\boldsymbol{\Sigma}}^{(0)} = \overleftrightarrow{\boldsymbol{\Sigma}}(0) = \hat{\sigma}(\mathbf{G}=0)\overleftrightarrow{\mathbf{I}} + i\omega\mu_0 \sum_{\mathbf{G}}{}' \hat{\sigma}(\mathbf{G})\overleftrightarrow{\mathbf{C}}_1(\mathbf{G}), \tag{2.40}$$

$$\overleftrightarrow{\mathbf{C}}_1(\mathbf{G}) = \sum_{\mathbf{G}'}{}' \hat{\sigma}(-\mathbf{G}')\overleftrightarrow{\mathbf{M}}_0^{-1}(\mathbf{G}',\mathbf{G}), \tag{2.41}$$

where, by Eq. (2.21),

$$\overleftrightarrow{\mathbf{M}}_0(\mathbf{G},\mathbf{G}') \equiv \overleftrightarrow{\mathbf{M}}(\mathbf{k}=0;\mathbf{G},\mathbf{G}') = \left[\left(G^2 - k_0^2\right)\overleftrightarrow{\mathbf{I}} - \mathbf{G}\mathbf{G}\right]\delta_{\mathbf{G},\mathbf{G}'} - i\omega\mu_0\hat{\sigma}(\mathbf{G}-\mathbf{G}')\overleftrightarrow{\mathbf{I}}. \tag{2.42}$$

Note that $\overleftrightarrow{\boldsymbol{\Sigma}}^{(0)}$ can also be obtained from Eq. (2.25) by substituting $k=0$. We get

$$\overleftrightarrow{\boldsymbol{\Sigma}}^{(0)} = \frac{i}{\omega\mu_0}\left[\left\{\overleftrightarrow{\mathbf{N}}^{-1}(\mathbf{k}=0;0,0)\right\}^{-1} + k_0^2\overleftrightarrow{\mathbf{I}}\right]. \tag{2.43}$$

As is shown in Appendix B, the linear term in the expansion Eq. (2.37) of $\overleftrightarrow{\boldsymbol{\Sigma}}(\mathbf{k})$ is

$$\overleftrightarrow{\boldsymbol{\Sigma}}^{(1)}(\hat{\mathbf{k}}) \equiv -i\omega\mu_0 \sum_{\mathbf{G}}{}' \overleftrightarrow{\mathbf{C}}_1(\mathbf{G})\cdot\overleftrightarrow{\mathbf{L}}(\hat{\mathbf{k}},\mathbf{G})\cdot\overleftrightarrow{\mathbf{C}}_2(\mathbf{G}), \tag{2.44}$$

$$\overleftrightarrow{\mathbf{L}}(\hat{\mathbf{k}},\mathbf{G}) = 2\left(\hat{\mathbf{k}}\cdot\mathbf{G}\right)\overleftrightarrow{\mathbf{I}} - \left(\hat{\mathbf{k}}\mathbf{G}+\mathbf{G}\hat{\mathbf{k}}\right), \tag{2.45}$$

$$\overleftrightarrow{\mathbf{C}}_2(\mathbf{G}) = \sum_{\mathbf{G}'}{}' \overleftrightarrow{\mathbf{M}}_0^{-1}(\mathbf{G},\mathbf{G}')\hat{\sigma}(\mathbf{G}') . \tag{2.46}$$

The dyadic $\overleftrightarrow{\boldsymbol{\Sigma}}^{(2)}(\hat{\mathbf{k}})$ in Eq. (2.37), also derived in Appendix B, can be written as

$$\begin{aligned}\overleftrightarrow{\boldsymbol{\Sigma}}^{(2)}(\hat{\mathbf{k}}) \equiv i\omega\mu_0 \sum_{\mathbf{G},\mathbf{G}'}{}' \overleftrightarrow{\mathbf{C}}_1(\mathbf{G})\cdot\Big[\overleftrightarrow{\mathbf{L}}(\hat{\mathbf{k}},\mathbf{G})\cdot\overleftrightarrow{\mathbf{M}}_0^{-1}(\mathbf{G},\mathbf{G}')\cdot\overleftrightarrow{\mathbf{L}}(\hat{\mathbf{k}},\mathbf{G}') \\ -\left(\overleftrightarrow{\mathbf{I}}-\hat{\mathbf{k}}\hat{\mathbf{k}}\right)\delta_{\mathbf{G},\mathbf{G}'}\Big]\cdot\overleftrightarrow{\mathbf{C}}_2(\mathbf{G}).\end{aligned} \tag{2.47}$$

Next, it is convenient to rewrite the dyadics $\overleftrightarrow{\boldsymbol{\Sigma}}^{(1)}$ and $\overleftrightarrow{\boldsymbol{\Sigma}}^{(2)}$ formally as follows:

$$\overleftrightarrow{\boldsymbol{\Sigma}}^{(1)} \equiv p\overleftrightarrow{\mathbf{I}}\cdot\overleftrightarrow{\boldsymbol{\Sigma}}^{(1)} + (1-p)\overleftrightarrow{\boldsymbol{\Sigma}}^{(1)}\cdot\overleftrightarrow{\mathbf{I}}\,, \tag{2.48}$$

$$\overleftrightarrow{\boldsymbol{\Sigma}}^{(2)} \equiv \overleftrightarrow{\mathbf{I}}\cdot\overleftrightarrow{\boldsymbol{\Sigma}}^{(2)}\cdot\overleftrightarrow{\mathbf{I}}\,. \tag{2.49}$$

Here, the artificially introduced fraction *p* can take, for the moment, any value. Its value will be determined below by imposing the Onsager symmetry relations [39 ,73]. Employing the identities

$$\overleftrightarrow{\mathbf{I}} = \hat{\mathbf{k}}\hat{\mathbf{k}} - \hat{\mathbf{k}}\times\hat{\mathbf{k}}\times\overleftrightarrow{\mathbf{I}} \tag{2.50}$$

and Eq. (2.48), together with Faraday's law (Eq. (2.28)), we can express $k\overleftrightarrow{\boldsymbol{\Sigma}}^{(1)}\cdot\mathbf{E}$ as

$$k\overleftrightarrow{\boldsymbol{\Sigma}}^{(1)}\cdot\mathbf{E}=p\left[\mathbf{k}\hat{\mathbf{k}}\cdot\overleftrightarrow{\boldsymbol{\Sigma}}^{(1)}\cdot\mathbf{E}-\mathbf{k}\times\hat{\mathbf{k}}\times\overleftrightarrow{\boldsymbol{\Sigma}}^{(1)}\cdot\mathbf{E}\right]+(1-p)\left[\overleftrightarrow{\boldsymbol{\Sigma}}^{(1)}\cdot\hat{\mathbf{k}}\mathbf{k}\cdot\mathbf{E}-\omega\overleftrightarrow{\boldsymbol{\Sigma}}^{(1)}\cdot\hat{\mathbf{k}}\times\mathbf{B}\right].\tag{2.51}$$

In a similar way, $k^2\overleftrightarrow{\boldsymbol{\Sigma}}^{(2)}\cdot\mathbf{E}$ can be transformed. Then

$$k^2\overleftrightarrow{\boldsymbol{\Sigma}}^{(2)}\cdot\mathbf{E}=\mathbf{k}\hat{\mathbf{k}}\cdot\overleftrightarrow{\boldsymbol{\Sigma}}^{(2)}\cdot\hat{\mathbf{k}}\mathbf{k}\cdot\mathbf{E}-\omega\mathbf{k}\hat{\mathbf{k}}\cdot\overleftrightarrow{\boldsymbol{\Sigma}}^{(2)}\cdot\hat{\mathbf{k}}\times\mathbf{B}-\mathbf{k}\times\hat{\mathbf{k}}\times\overleftrightarrow{\boldsymbol{\Sigma}}^{(2)}\cdot\left(\hat{\mathbf{k}}\mathbf{k}\cdot\mathbf{E}-\omega\hat{\mathbf{k}}\times\mathbf{B}\right).\tag{2.52}$$

Substituting Eqs. (2.51) and (2.52) into Eq. (2.37) and this, in turn, into the Ampére-Maxwell law (Eq. (2.26)), and writing all the terms of $\overleftrightarrow{\boldsymbol{\Sigma}}(\mathbf{k})$ which are of the form $\mathbf{k}\times\overleftrightarrow{\boldsymbol{\Lambda}}(\mathbf{k})$ on the left side, is obtained

$$\begin{aligned}&\mathbf{k}\times\left\{\mathbf{B}-\mu_0 i\hat{\mathbf{k}}\times\left[p\overleftrightarrow{\boldsymbol{\Sigma}}^{(1)}\cdot\mathbf{E}+\overleftrightarrow{\boldsymbol{\Sigma}}^{(2)}\cdot\hat{\mathbf{k}}\mathbf{k}\cdot\mathbf{E}-\omega\overleftrightarrow{\boldsymbol{\Sigma}}^{(2)}\cdot\left(\hat{\mathbf{k}}\times\mathbf{B}\right)+\cdots\right]\right\}=\\&-\omega\mu_0\left\{\varepsilon_0\mathbf{E}+\frac{i}{\omega}\left[\overleftrightarrow{\boldsymbol{\Sigma}}^{(0)}\cdot\mathbf{E}+p\mathbf{k}\hat{\mathbf{k}}\cdot\overleftrightarrow{\boldsymbol{\Sigma}}^{(1)}\cdot\mathbf{E}+(1-p)\overleftrightarrow{\boldsymbol{\Sigma}}^{(1)}\cdot\hat{\mathbf{k}}\mathbf{k}\cdot\mathbf{E}+\mathbf{k}\hat{\mathbf{k}}\cdot\overleftrightarrow{\boldsymbol{\Sigma}}^{(2)}\cdot\hat{\mathbf{k}}\mathbf{k}\cdot\mathbf{E}\right.\right.\\&\left.\left.-(1-p)\omega\overleftrightarrow{\boldsymbol{\Sigma}}^{(1)}\cdot\left(\hat{\mathbf{k}}\times\mathbf{B}\right)-\omega\mathbf{k}\hat{\mathbf{k}}\cdot\overleftrightarrow{\boldsymbol{\Sigma}}^{(2)}\cdot\left(\hat{\mathbf{k}}\times\mathbf{B}\right)+\cdots\right]\right\}.\end{aligned}\tag{2.53}$$

Comparing with Eq. (2.30), it can identified the expression in the curly brackets on the left side of this equation as the vector $\mu_0\mathbf{H}$:

$$\mu_0\mathbf{H}\equiv\mathbf{B}-\mu_0 i\hat{\mathbf{k}}\times\left[p\overleftrightarrow{\boldsymbol{\Sigma}}^{(1)}\cdot\mathbf{E}+\overleftrightarrow{\boldsymbol{\Sigma}}^{(2)}\cdot\hat{\mathbf{k}}\mathbf{k}\cdot\mathbf{E}-\omega\overleftrightarrow{\boldsymbol{\Sigma}}^{(2)}\cdot\left(\hat{\mathbf{k}}\times\mathbf{B}\right)+\cdots\right].\tag{2.54}$$

The comparison of the Eqs. (2.53) and (2.30) also identifies the displacement vector D as

$$\mathbf{D} \equiv \varepsilon_0 \mathbf{E} + \frac{i}{\omega}\Big[\overleftrightarrow{\boldsymbol{\Sigma}}^{(0)} \cdot \mathbf{E} + p k \hat{\mathbf{k}} \cdot \overleftrightarrow{\boldsymbol{\Sigma}}^{(1)} \cdot \mathbf{E} + (1-p) \overleftrightarrow{\boldsymbol{\Sigma}}^{(1)} \cdot \hat{\mathbf{k}} \mathbf{k} \cdot \mathbf{E} + \mathbf{k} \hat{\mathbf{k}} \cdot \overleftrightarrow{\boldsymbol{\Sigma}}^{(2)} \cdot \hat{\mathbf{k}} \mathbf{k} \cdot \mathbf{E} \\ -(1-p)\omega \overleftrightarrow{\boldsymbol{\Sigma}}^{(1)} \cdot \left(\hat{\mathbf{k}} \times \mathbf{B} \right) - \omega \mathbf{k} \hat{\mathbf{k}} \cdot \overleftrightarrow{\boldsymbol{\Sigma}}^{(2)} \cdot \left(\hat{\mathbf{k}} \times \mathbf{B} \right) + \cdots \Big]. \tag{2.55}$$

Due to the assumption of Eq. (2.10), it is of particular interest to determine the material equations in the limit $k \to 0$. The resulting expressions for D and H in this limit are:

$$\mathbf{D} \equiv \varepsilon_0 \mathbf{E} + \frac{i}{\omega}\left[\overleftrightarrow{\boldsymbol{\Sigma}}^{(0)} \cdot \mathbf{E} - (1-p)\omega \overleftrightarrow{\boldsymbol{\Sigma}}^{(1)} \cdot \left(\hat{\mathbf{k}} \times \mathbf{B} \right) \right], \tag{2.56}$$

$$\mu_0 \mathbf{H} \equiv \mathbf{B} - \mu_0 i \hat{\mathbf{k}} \times \left[p \overleftrightarrow{\boldsymbol{\Sigma}}^{(1)} \cdot \mathbf{E} - \omega \overleftrightarrow{\boldsymbol{\Sigma}}^{(2)} \cdot \left(\hat{\mathbf{k}} \times \mathbf{B} \right) \right]. \tag{2.57}$$

Note that in the Eqs. (2.56) and (2.57) the terms proportional to ω have been kept because for optical bands they can be of the same order as the first terms. These expressions can be rewritten in the form of the *magneto-dielectric* response

$$\mathbf{D} = \overleftrightarrow{\boldsymbol{\alpha}} \cdot \mathbf{E} + \overleftrightarrow{\boldsymbol{\beta}} \cdot \mathbf{B}, \qquad \mathbf{H} = \overleftrightarrow{\boldsymbol{\phi}} \cdot \mathbf{E} + \overleftrightarrow{\boldsymbol{\psi}} \cdot \mathbf{B}, \tag{2.58}$$

$$\overleftrightarrow{\boldsymbol{\alpha}} = \varepsilon_0 \overleftrightarrow{\mathbf{I}} + (i/\omega) \overleftrightarrow{\boldsymbol{\Sigma}}^{(0)}, \tag{2.59}$$

$$\overleftrightarrow{\boldsymbol{\beta}} = -i(1-p) \overleftrightarrow{\boldsymbol{\Sigma}}^{(1)}(\hat{\mathbf{k}}) \cdot \left(\hat{\mathbf{k}} \times \overleftrightarrow{\mathbf{I}} \right), \tag{2.60}$$

$$\overleftrightarrow{\boldsymbol{\phi}} = -ip \hat{\mathbf{k}} \times \overleftrightarrow{\boldsymbol{\Sigma}}^{(1)}(\hat{\mathbf{k}}), \tag{2.61}$$

$$\overleftrightarrow{\boldsymbol{\psi}} = \left(1/\mu_0 \right) \overleftrightarrow{\mathbf{I}} + i\omega \hat{\mathbf{k}} \times \overleftrightarrow{\boldsymbol{\Sigma}}^{(2)}(\hat{\mathbf{k}}) \cdot \left(\hat{\mathbf{k}} \times \overleftrightarrow{\mathbf{I}} \right). \tag{2.62}$$

Comparing the magneto-electric response (Eq. (2.58)) with the conventional bianisotropic response (Eqs. (2.38) and (2.39)), it is straightforward to establish the relations, also derived in Ref. 51,

$$\overleftrightarrow{\boldsymbol{\varepsilon}} = \overleftrightarrow{\boldsymbol{\alpha}} - \overleftrightarrow{\boldsymbol{\beta}} \cdot \overleftrightarrow{\boldsymbol{\psi}}^{-1} \cdot \overleftrightarrow{\boldsymbol{\phi}}, \quad \overleftrightarrow{\boldsymbol{\gamma}} = \overleftrightarrow{\boldsymbol{\beta}} \cdot \overleftrightarrow{\boldsymbol{\psi}}^{-1}, \quad \overleftrightarrow{\boldsymbol{\delta}} = -\overleftrightarrow{\boldsymbol{\psi}}^{-1} \cdot \overleftrightarrow{\boldsymbol{\phi}}, \quad \overleftrightarrow{\boldsymbol{\mu}} = \overleftrightarrow{\boldsymbol{\psi}}^{-1}. \tag{2.63}$$

The artificially introduced parameter p is determined by imposing the Onsager symmetry relations [39, 73],

$$\overleftrightarrow{\boldsymbol{\varepsilon}} = \overleftrightarrow{\boldsymbol{\varepsilon}}_T, \quad \overleftrightarrow{\boldsymbol{\mu}} = \overleftrightarrow{\boldsymbol{\mu}}_T, \quad \overleftrightarrow{\boldsymbol{\delta}} = -\overleftrightarrow{\boldsymbol{\gamma}}_T, \tag{2.64}$$

where the subscripts T denote transpositions of the dyadics. It is shown in Appendix C that these relations between the effective dyadics of the bi-anisotropic response are satisfied only for $p = 1/2$.

It is interesting to note that the effective dyadics $\overleftrightarrow{\boldsymbol{\varepsilon}}$, $\overleftrightarrow{\boldsymbol{\gamma}}$, and $\overleftrightarrow{\boldsymbol{\mu}}$ depend on the *direction* of the wave vector k, which introduces anisotropy additional to that of the lattice. It means that, in general, these dyadics diagonalize in different coordinate systems. This must have important consequences for the response at the macro-level. Nevertheless, the dyadics defining the bi-anisotropic response (as well as those of the magneto-dielectric response) are independent of the *magnitude* of the wave vector k. On the other hand, as we have seen in sec. 2.3, the dielectric response, *to the same physical precision*, incorporates terms in $\overleftrightarrow{\boldsymbol{\varepsilon}}(\mathbf{k},\omega)$ that are linear and quadratic in k.

2.5 Dispersion relation of the homogenized medium

The dispersion relation for the electromagnetic modes in the homogenized medium can be obtained substituting the bi-anisotropic response (Eq. (2.58)) into the macroscopic Maxwell Equations (Eqs. (2.30)-(2.33)). Solving for the macroscopic electric field E we get:

$$\left[\omega^2\overset{\leftrightarrow}{\boldsymbol{\alpha}}+\omega\mathbf{k}\times\overset{\leftrightarrow}{\boldsymbol{\phi}}(\hat{\mathbf{k}})+\left(\omega\overset{\leftrightarrow}{\boldsymbol{\beta}}(\hat{\mathbf{k}})+\mathbf{k}\times\overset{\leftrightarrow}{\boldsymbol{\psi}}(\hat{\mathbf{k}})\right)\cdot\left(\mathbf{k}\times\overset{\leftrightarrow}{\mathbf{I}}\right)\right]\cdot\mathbf{E}=0\,. \tag{2.65}$$

Even though, the material dyadics are complicated functions of ω and $\hat{\mathbf{k}}$, in principle it is possible to solve Eq. (2.65) for any given ω or $\mathbf{k}$. It is important to remark that, *for transverse modes*, the substitution of Eqs. (2.59) - (2.62) in Eq. (2.65) is equivalent to the band structure problem in the limit $\mathbf{k}\to 0$; on the other hand, this substitution may not always render the *longitudinal modes* with sufficient precision. The use of Eq. (2.65) can result in an important simplification for high symmetry systems. In such cases it is possible to calculate the effective permeability from the band structure and the effective permittivity, rather than using the direct procedure, namely, the substitution of Eq. (2.62) in the last Eq. (2.63). The evaluation of $\overset{\leftrightarrow}{\boldsymbol{\Sigma}}^{(2)}$ is thus avoided and computation time saved.

2.6 Analytic results for special cases

In this section will be analyzed the bi-anisotropic response in several important cases, considering first generalities (sub-section 2.6.1) and later specific systems (sub-section 2.6.2).

2.6.1. Generalities

2.6.1.a Inversion Symmetry

If the unit cell of the homogenized PC is composed of inclusions possessing inversion symmetry, then $\overleftrightarrow{\boldsymbol{\Sigma}}(-\mathbf{k}) = \overleftrightarrow{\boldsymbol{\Sigma}}(\mathbf{k})$. Hence, it follows from Eq. (2.37) that

$$\overleftrightarrow{\boldsymbol{\Sigma}}_1(\hat{\mathbf{k}}) = 0\,. \tag{2.66}$$

Hence, by the Eqs. (2.60) and (2.61), also $\overleftrightarrow{\boldsymbol{\beta}} = \overleftrightarrow{\boldsymbol{\phi}} = 0$ and, using Eq. (2.63), the conventional bi-anisotropic response acquires the form

$$\begin{aligned} &\mathbf{D} = \overleftrightarrow{\boldsymbol{\varepsilon}} \cdot \mathbf{E}, \qquad && \overleftrightarrow{\boldsymbol{\varepsilon}} = \varepsilon_0 \overleftrightarrow{\mathbf{I}} + \left(i/\omega\right) \overleftrightarrow{\boldsymbol{\Sigma}}^{(0)}; \\ &\mathbf{B} = \overleftrightarrow{\boldsymbol{\mu}}(\hat{\mathbf{k}}) \cdot \mathbf{H}, && \overleftrightarrow{\boldsymbol{\mu}}^{-1}(\hat{\mathbf{k}}) = \left(1/\mu_0\right) \overleftrightarrow{\mathbf{I}} + i\omega \hat{\mathbf{k}} \times \overleftrightarrow{\boldsymbol{\Sigma}}^{(2)}(\hat{\mathbf{k}}) \cdot \left(\hat{\mathbf{k}} \times \overleftrightarrow{\mathbf{I}}\right). \end{aligned} \tag{2.67}$$

Here, it can be seen that the permittivity tensor $\overleftrightarrow{\boldsymbol{\varepsilon}}$, being independent of the unit vector $\hat{\mathbf{k}}$, must be diagonal in some coordinate system that is embedded in the PC. On the other hand, the permeability dyadic $\overleftrightarrow{\boldsymbol{\mu}}(\hat{\mathbf{k}})$ diagonalizes in a coordinate system which has one axis parallel to $\hat{\mathbf{k}}$. This is seen from the fact that, for any unit vector $\hat{\mathbf{l}} \perp \hat{\mathbf{k}}$, the following off-diagonal matrix elements vanish:

$$(\overleftrightarrow{\boldsymbol{\mu}}^{-1})_{\hat{\mathbf{k}}\hat{\mathbf{l}}} = (\overleftrightarrow{\boldsymbol{\mu}}^{-1})_{\hat{\mathbf{l}}\hat{\mathbf{k}}} = 0\,, \tag{2.68}$$

as follows from the last Eq. (2.67). As for the corresponding diagonal element,

$$\left(\overleftrightarrow{\boldsymbol{\mu}}^{-1}\right)_{\hat{\mathbf{k}}\hat{\mathbf{k}}} = \hat{\mathbf{k}} \cdot \overleftrightarrow{\boldsymbol{\mu}}^{-1}(\hat{\mathbf{k}}) \cdot \hat{\mathbf{k}} = \left(1/\mu_0\right). \tag{2.69}$$

However, this element has no repercussions because Eq. (2.30) gives the same result if it is omitted. The reason for the element $\left(\overleftrightarrow{\mu}^{-1}\right)_{\hat{\mathbf{k}}\hat{\mathbf{k}}}$ having no physical relevance is that the Maxwell law (Eq. (2.30)) has nothing to say about a component of H parallel to k, and such a component cannot exist. In fact, this is even true in the absence of inversion symmetry and is a result of the non-existence of magnetic charges, $\nabla \cdot \mathbf{B} = 0$. [Indeed, it follows from Eq. (2.54) that $\mathbf{H} \cdot \hat{\mathbf{k}} = \mathbf{B} \cdot \hat{\mathbf{k}} = 0$.]

In a system possessing inversion symmetry, the general dispersion relation (Eq. (2.65)) simplifies to

$$\omega^2 \overleftrightarrow{\boldsymbol{\varepsilon}} \cdot \mathbf{E} + \mathbf{k} \times \overleftrightarrow{\boldsymbol{\mu}}^{-1}(\hat{\mathbf{k}}) \cdot \left(\mathbf{k} \times \mathbf{E}\right) = 0 . \qquad (2.70)$$

This result has been derived previously by Amirkhizi and Nemat-Nasser [74].

2.6.1.b Cubic symmetry

Now, will be considered the case of cubic symmetry, according to which the permittivity and permeability tensors have the form

$$\overleftrightarrow{\boldsymbol{\varepsilon}} = \varepsilon \overleftrightarrow{\mathbf{I}} , \qquad (2.71)$$

$$\overleftrightarrow{\boldsymbol{\mu}}^{-1}(\hat{\mathbf{k}}) = \left(1/\mu_0\right)\hat{\mathbf{k}}\hat{\mathbf{k}} + \left(1/\mu\right)\left(\overleftrightarrow{\mathbf{I}} - \hat{\mathbf{k}}\hat{\mathbf{k}}\right). \qquad (2.72)$$

The first term of Eq. (2.72) follows from Eq. (2.69). However, because this term does not contribute [as pointed out after Eq. (2.69)], in practice we can replace μ_0 by μ and write, simply

$$\mathbf{D} = \varepsilon\mathbf{E}, \qquad \mathbf{B} = \mu\mathbf{H}. \tag{2.73}$$

So, for the cubic symmetry the material response is isotropic. Obviously, the dispersion relation for the electromagnetic waves in the homogenized material is given by

$$k^2 = \omega^2 \varepsilon\mu. \tag{2.74}$$

2.6.1.c Mutually perpendicular mirror planes (2D photonic crystal)

Consider a 2D PC of cylinders parallel to *z* axis and possessing mirror planes perpendicular to the *x* and *y* axes. Such a structure has inversion symmetry (Eq. (2.66)) and also satisfies the following equation:

$$\hat{\sigma}(-\mathbf{G}_x, \mathbf{G}_y) = \hat{\sigma}(\mathbf{G}_x, \mathbf{G}_y) = \hat{\sigma}(\mathbf{G}_x, -\mathbf{G}_y). \tag{2.75}$$

As a consequence of Eq. (2.75), $\ddot{\boldsymbol{\varepsilon}}$ is always a diagonal tensor in the natural PC coordinate system $(\hat{\mathbf{x}}, \hat{\mathbf{y}}, \hat{\mathbf{z}})$. Again, $\ddot{\boldsymbol{\mu}}(\hat{\mathbf{k}})$ can be diagonal only in a reference system $(\hat{\mathbf{k}}, \hat{\mathbf{l}}, \hat{\mathbf{m}})$ in which one of the axes is parallel to $\hat{\mathbf{k}}$. Of course, when an electromagnetic wave propagates in a high symmetry direction, both dyadics $\ddot{\boldsymbol{\varepsilon}}$ and $\ddot{\boldsymbol{\mu}}$ are diagonal.

For example, consider an electromagnetic wave propagating in the $\hat{\mathbf{x}}$ direction, i.e. $\hat{\mathbf{k}} = \hat{\mathbf{x}}$. Equations (2.59) and (2.62) result in diagonal tensors and, because of the mirror planes considered (equivalent to a four-fold rotation axis z), $\varepsilon_{xx} = \varepsilon_{yy} \equiv \varepsilon_{\perp}$, $\mu_{xx} = \mu_{yy} \equiv \mu_{\perp}$, $\varepsilon_{zz} \equiv \varepsilon_{\parallel}$, $\mu_{zz} \equiv \mu_{\parallel}$; in dyadic notation

$$\vec{\vec{\boldsymbol{\varepsilon}}} = \varepsilon_{\perp}\left(\hat{\mathbf{x}}\hat{\mathbf{x}} + \hat{\mathbf{y}}\hat{\mathbf{y}}\right) + \varepsilon_{\parallel}\hat{\mathbf{z}}\hat{\mathbf{z}}\,, \tag{2.76}$$

$$\vec{\vec{\boldsymbol{\mu}}} = \mu_{\perp}\left(\hat{\mathbf{x}}\hat{\mathbf{x}} + \hat{\mathbf{y}}\hat{\mathbf{y}}\right) + \mu_{\parallel}\hat{\mathbf{z}}\hat{\mathbf{z}}\,. \tag{2.77}$$

Substituting Eqs. (2.76) and (2.77) in Eq. (2.70) are found two possible solutions, as is expected, one for the E-mode (with the electric field in the $\hat{\mathbf{z}}$ direction) and the other for the H-mode (with the magnetic field in the $\hat{\mathbf{z}}$ direction),

$$k_x^2 = \omega^2 \varepsilon_{\parallel} \mu_{\perp} \qquad \text{E-mode,} \tag{2.78}$$

$$k_x^2 = \omega^2 \varepsilon_{\perp} \mu_{\parallel} \qquad \text{H-mode.} \tag{2.79}$$

From Eqs. (2.78) and (2.79) is possible to conclude that it is possible to obtain the effective permeability from the dispersion relation $\omega(k)$ when the effective permittivity is known for high symmetry conditions. This can result in considerable saving of computing time. Similar conclusions are obtained for high-symmetry 3Ds (see Eq. (2.74)) and for 1D PCs. Nevertheless, in exceptional cases the computation of ε can be more problematic than the determination of μ. In such situations Eqs. (2.78) and (2.79) can be used to find ε as, in fact, the latter was done for the H-mode of metallic cylinders, see sec. 2.7.3.

2.6.2 Specific systems

2.6.2.a Small spheres in a cubic lattice

Here is applied Eq. (2.67) to calculate the effective ε and μ of a cubic photonic crystal with a small sphere of radius *r* in every unit cell. So, the filling fraction *f* is assumed to be very small:

$$f = \frac{4\pi}{3}\frac{r^3}{a^3} \ll 1, \tag{2.80}$$

a being the lattice constant. The generalized conductivities for the spherical inclusion and the host material are, respectively, $\hat{\sigma}_a$ and $\hat{\sigma}_b$. Because of the cubic symmetry, $\overleftrightarrow{\boldsymbol{\Sigma}}^{(0)}$, as given by Eq. (2.43), must be proportional to the unit dyadic $\overleftrightarrow{\mathbf{I}}$. Hence, Eq. (2.67) reduces to the scalar response (Eq. (2.73)). In obtaining ε, we have calculated the dyadic $\overleftrightarrow{\mathbf{N}}^{-1}(\mathbf{k}=0;0,0)$ assuming that $r \ll a$. The details of this approximate calculation of the dyadic $\overleftrightarrow{\mathbf{N}}^{-1}(\mathbf{k}=0;0,0)$ are explained in the Appendix D. We get

$$\overleftrightarrow{\mathbf{N}}^{-1}(\mathbf{k}=0;0,0) = \frac{1}{k_0^2 + i\omega\mu_0\hat{\sigma}_b}\left(\frac{i\omega\mu_0\left(\hat{\sigma}_a - \hat{\sigma}_b\right)f}{k_0^2 + i\omega\mu_0\left[\left(\hat{\sigma}_a - \hat{\sigma}_b\right)\left(\tfrac{2}{3}f + \tfrac{1}{3}\right) + \hat{\sigma}_b\right]} - 1\right)\overleftrightarrow{\mathbf{I}} \tag{2.81}$$

After some algebraic operations and using Eqs. (2.43) and (2.67), is found

$$\varepsilon = \varepsilon_b \frac{1 + 2f\,\dfrac{\varepsilon_a - \varepsilon_b}{\varepsilon_a + 2\varepsilon_b}}{1 - f\,\dfrac{\varepsilon_a - \varepsilon_b}{\varepsilon_a + 2\varepsilon_b}} \tag{2.82}$$

where

$$\varepsilon_a = \varepsilon_0 + i\hat{\sigma}_a/\omega, \qquad \varepsilon_b = \varepsilon_0 + i\hat{\sigma}_b/\omega. \tag{2.83}$$

This results for ε coincides with the well-known Maxwell-Garnett formula for the effective dielectric constant of a composite. In this case $\mu \approx \mu_0$.

2.6.2.b Cubic lattice of metallic wires

Now is applied the theory to another cubic photonic crystal, which is constructed with thin metallic wires ("3D crosses"). Here, the dyadic $\tilde{\mathbf{N}}^{-1}(\mathbf{k}=0;\mathbf{G},\mathbf{G}')$ and, consequently, the permittivity ε (Eq. (2.67)) were calculated approximately by assuming that the radius of the wires r_0 is much smaller than the lattices constant a. The final result for the dielectric constant is (see Appendix E)

$$\frac{\varepsilon(\omega)}{\varepsilon_0} = 1 - \frac{\omega_0^2}{\omega(\omega + i\rho\omega_0^2)}, \qquad \omega_0^2 = \frac{2\pi c^2}{a^2 \ln(a/r_0)}, \qquad \rho = \frac{\varepsilon_0 a^2}{\pi r_0^2 \sigma}, \tag{2.84}$$

where σ is the usual conductivity of the metal. This is in agreement with Pendry's plasma model[23] with effective plasma frequency ω_0 and damping frequency $\rho\omega_0^2$. A similar expression for the effective permittivity is obtained for wires with square cross-section, but with ω_0^2 and ρ given by (see Appendix E)

$$\omega_0^2 = \frac{2\pi c^2}{a^2 \ln(a/l)}, \qquad \rho = \frac{\varepsilon_0 a^2}{l^2 \sigma}, \tag{2.85}$$

where l is the side length of the square cross section. For this kind of structures, $\mu \approx \mu_0$.

2.7 Numerical results

The effective parameters ε and μ can be calculated analytically only for a few high symmetry structures, as was shown in the previous section for a cubic array of spheres and wires. In general, the response at the macro level must be obtained numerically. In this section are presented computational results for the effective permittivity and permeability of several well known photonic structures. As a check, the results are compared with other homogenization theories reported in the literature.

2.7.1 Two dimensions dielectric cylinders

As a first check, is obtained the effective parameters of a 2D PC formed by circular dielectric cylinders in a square lattice. Strictly speaking, the quasi-static limit is studied, although in practice the results hold up to frequencies as high as about the middle of the first (acoustic) band, with quite good precision. Two complementary cases are presented, namely silicon-cylinders in an air host and air-cylinders in a silicon host. Figure 2.1 shows the effective permittivity and permeability as a function of the filling fraction. Such a structure presents isotropy in the plane of periodicity, resulting in a uni-axial dyadic for the effective permittivity, namely Eq. (2.76):

$$\overset{\leftrightarrow}{\boldsymbol{\varepsilon}} = \left\{ \begin{matrix} \varepsilon_{\perp} & 0 & 0 \\ 0 & \varepsilon_{\perp} & 0 \\ 0 & 0 & \varepsilon_{\|} \end{matrix} \right\}. \qquad (2.86)$$

The solid line corresponds to the solution of Eq. (2.67) for $\overset{\leftrightarrow}{\boldsymbol{\varepsilon}}$ and the dashed line to the results obtained for the same structure in Ref. 10. The calculations show good agreement, except for the $\varepsilon_{\|}$ component in the region of very high filling fractions. As expected, because of the simplicity of the system, these dielectric structures do not present resonances and there are no magnetic effects. The method gives the correct answer, with $\vec{\boldsymbol{\mu}} = \mu_0 \vec{\mathbf{I}}$ for any filling fraction. It is important to stress that the method presented in Ref. 10 assumes that there are no magnetic effects ($\mu = \mu_0$ for any ω) and is valid only for dielectric structures in the region where the dispersion relation $\omega(k)$ is linear.

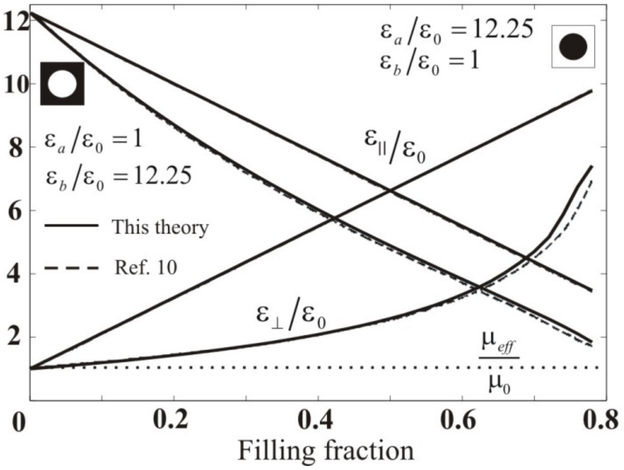

Fig. 2.1. Effective permittivity and permeability of arrays of circular Si rods in air and of cylindrical holes in a Si host as a function of the filling fraction. Solid lines correspond to the principal dielectric constants and dotted lines to the effective permeability. In this case were used 1517 G values in the computation. For these simple dielectric structures there are no magnetic effects, as expected. Dashed lines correspond to the results obtained for the same structure in Ref. 10. There is good agreement between the calculations, especially for $f < 0.6$.

2.7.2 Three dimension dielectric spheres

Figure 2.2 shows the effective permittivity and permeability for a 3D PC composed of silicon spheres in an air host for different values of the filling fraction. As in subsection A, the quasistatic limit has been considered. Due to the cubic symmetry of the system, the electromagnetic properties can be completely defined in terms of two scalars, ε and μ, see Eqs. (2.71)-(2.73). The solid line corresponds to the effective permittivity computed using Eq. (2.67) and the dashed line describes the effective permittivity calculated by Datta et al. [24] for the same system. There is good agreement, especially for small filling fractions. Again, for this simple dielectric structure with $\omega \propto k$, $\mu = \mu_0$ for any filling fraction.

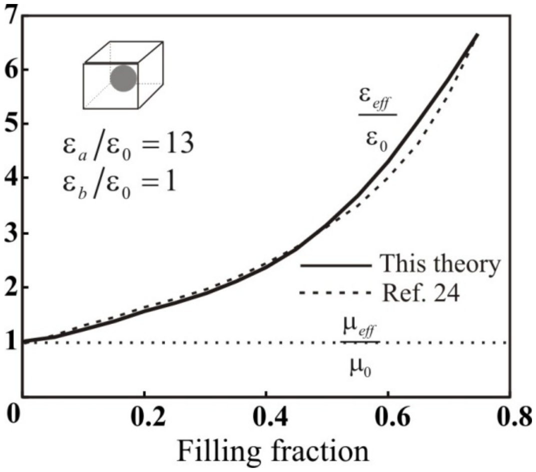

Fig. 2.2. Effective permittivity (solid line) and effective permeability (dotted line) of a 3D PC of dielectric spheres in a cubic lattice as a function of the filling fraction. In this case we used 1793 G values in the computation, resulting in very good convergence. As in Fig. 2.1, there are no magnetic effects. Dashed lines correspond to the effective permittivity obtained in Ref. 24 for the same structure. There is good agreement between the calculations except for the region around $f \approx 0.64$.

2.7.3 Two dimension metallic wires

A bi-dimensional metallo-dielectric PC of metallic wires has two different behaviors, depending on the polarization of the incident wave. For the E-mode (with the electric field parallel to the wires) the structure presents a low-frequency band gap [75]. This behavior is correctly described by the effective parameters obtained from Eq. (2.67). Figure 2.3 presents the dispersion relation $\omega(k_x)$ for the first band and the relevant elements of the effective permittivity and permeability dyadics for a square lattice of copper wires $(\omega_p = 6.0774\times10^{15}\,\mathrm{s}^{-1})$, considering three different filling fractions. Here the wave propagation is fixed to the [100] direction. Part *a* of the figure shows how the low-frequency band gap becomes wider as the filling fraction is increased. At the same time the first band is raised in frequency, while its width decreases. Part *b* shows the effective permittivity $\varepsilon_{\|}$ and the effective permeability $\mu_{\perp}$ as a function of the frequency. We should note that inside the band gap $\varepsilon_{\|}$ and $\mu_{\perp}$ have always opposite signs, namely $\varepsilon < 0$ and $\mu \geq \mu_0$. This results in an imaginary effective refractive index, as corresponds to prohibition of propagation in this frequency range. As the frequency is increased $\varepsilon_{\|}$ goes from negative to positive values, being equal to zero at the upper edge of the band gap. On the other hand, $\mu_{\perp}$ is strictly equal to μ_0 for ω = 0 as follows from Eq. (2.67). As the frequency is increased, $\mu_{\perp}$ acquires values greater than μ_0, resulting in paramagnetic behavior.

Another situation is observed for the same structure of metallic wires when the electric field of the incident wave is in the plane of periodicity. For this polarization (H-mode) there is no low-frequency band gap and the dispersion $\omega(k_x)$ is linear at low frequencies. Nevertheless, as was pointed out by Krokhin et al [26], for the H-mode this structure composed of nonmagnetic materials presents a remarkable diamagnetic behavior.

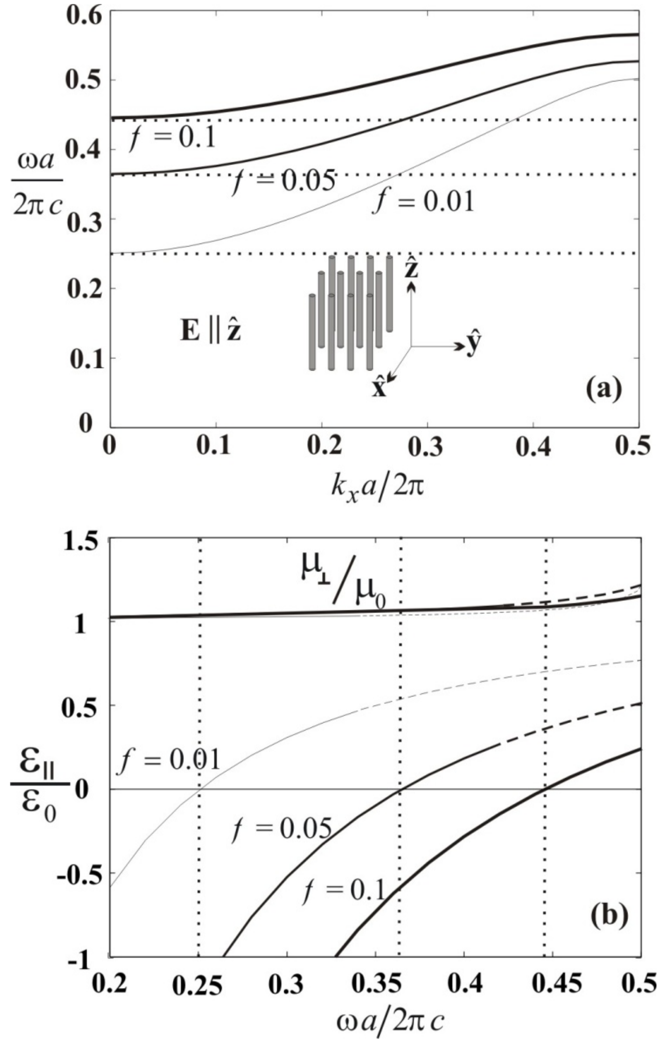

Fig. 2.3. E-mode dispersion relation $\omega(k_x)$ for the first band (part *a*) and the relevant elements of the effective permittivity and permeability dyadics (part b) for a square lattice of copper wires ($\omega_p^{Cu} = 6.077 \times 10^{15} s^{-1}$) with a lattice constant $a = 1.5 \times 10^{-4} cm$. Three different filling fractions are considered. The wave propagation is along the [1 0 0] direction and have been used 1405 G values in the computation. The system presents a low-frequency band gap in which the effective refractive index is imaginary. In addition, the system also presents a paramagnetic behavior inside the first pass-band. The dotted lines mark the lower edges of the pass bands. The dashed lines indicate regions ($k_x > \pi / 2a$) where our long-wavelength expansion cannot be trusted.

Figure 2.4 shows the effective permeability $\mu_{\parallel}$ (part *a*) and the corresponding effective permittivity $\varepsilon_{\perp}$ (part *b*) as a function of the filling fraction in the limit $k \to 0$ (and $\omega \to 0$) for three different metals, namely aluminum, copper and bismuth (with plasma frequencies, respectively, $\omega_p = 2.278 \times 10^{16}\,\mathrm{s}^{-1}$, $6.077 \times 10^{15}\,\mathrm{s}^{-1}$, and $9.844 \times 10^{12}\,\mathrm{s}^{-1}$). In part *a*, the solid lines were obtained from Eq. (2.67) and the dotted lines are the results in Ref. 26.

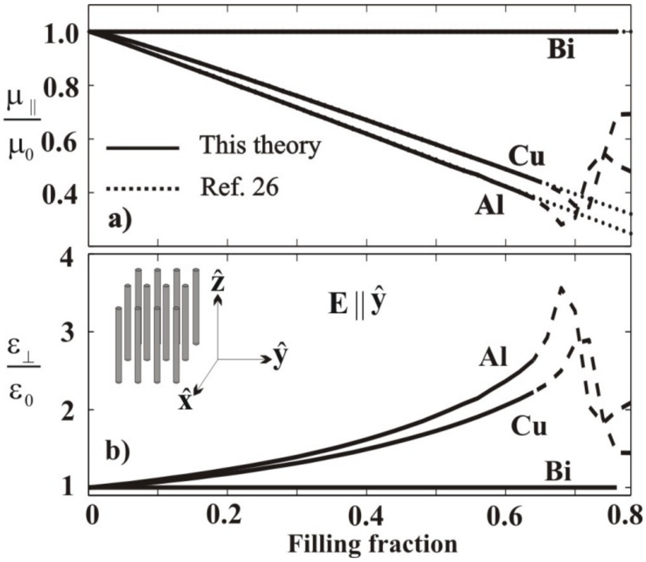

Fig. 2.4. Effective permeability $\mu_{\parallel}$ (part *a*) and effective permittivity $\varepsilon_{\perp}$ (part *b*) for the H-mode as a function of the filling fraction in the limit $k \to 0$ (and $\omega \to 0$) for a square lattice of metallic wires whit a lattice constant $a = 1.5 \times 10^{-4}\,cm$. Three different metals are considered: aluminum ($\omega_p^{Al} = 2.278 \times 10^{16}\,s^{-1}$), copper ($\omega_p^{Cu} = 6.077 \times 10^{15}\,s^{-1}$) and bismuth ($\omega_p^{Bi} = 9.844 \times 10^{12}\,s^{-1}$). In part *a*, the solid lines were obtained from Eq. (2.67) and the dotted lines are the results obtained in Ref. 26. The two methods show good agreement with the exception of high filling fractions where is not reach convergence (dotted lines) with the 1405 G values used in this computation. The diamagnetic behavior observed for copper and aluminum increases with the filling fraction. The effective permittivity $\varepsilon_{\perp}$ (part *b*) was obtained from part *a* and the dispersion relation $\omega(k_x)$.

As before, is obteined good agreement between the two methods, with the exception of high filling fractions where convergence is not reached (dashed lines) with the 1405 “plane waves” used in this computation. The agreement in this region can be improved by increasing the number of plane waves. This behavior is also observed in dielectric structures, where small filling fractions require a smaller number of “plane waves” in order to obtain convergence in the computation. Using Fig. 2.4(a) for the permeability, the effective permittivity $\varepsilon_{\perp}$, Fig. 2.4(b), was obtained with the help of Eq. (2.79). It should be note that the direct computation of the permittivity from Eq. (2.67) ran into convergence problems.

2.7.4 3D crosses of continuous and cut wires

In this section are calculated the effective permittivity and the effective permeability of a 3D metallo-dielectric photonic crystal of thin metallic wires of square cross-section (l^2) in a cubic lattice. Three cases are presented: crosses of continuous wires (Fig. 2.5a), crosses of cut wires separated by a small gap of width $d = 0.00105a$ (Fig. 2.6a), and crosses of cut wires with larger gap $d = 0.00262a$ (Fig. 2.7a). The wires are characterized by a very high conductivity given by $\sigma = 10^7 / a\mu_0 c$. Note that it is not necessary to specify the lattice constant *a*; it serves as a normalization constant. As before, because of the cubic symmetry of the system the electromagnetic properties are completely defined by two scalars, ε and μ. These effective parameters were calculated by using Eqs. (2.67), (2.25) and $\ddot{\mathbf{\Sigma}}^{(2)} = \lim_{k\to 0}\left(\ddot{\mathbf{\Sigma}}(k) - \ddot{\mathbf{\Sigma}}^{(0)}\right)/k^2$.

In the calculation of the matrix block $\ddot{\mathbf{N}}^{-1}(\mathbf{k};0,0)$, appearing in Eq. (2.25), it has been taken advantage of the square cross section by dividing the wires into a set of *n* small cubes of side l and using the approach of small inclusions (see Appendix D, Eq. (D10) for the form factor of each cube. This numerical method, known as the form-factor division approach [69], has led to an algebraic system of 3*n* equations. In these calculations, have been used 55 small cubes (i.e. $n = 55$) and the results converged when the summations over $\mathbf{G}$ in the $3n \times 3n$ coefficients of this system had $N = (61)^3$ summands (where $N = 226981$ also denotes the number of "plane waves"). The form-factor division approach is particularly useful when the filling fraction *f* of the inclusions is small because *n* should not be very large. Figs. 2.5, 2.6 and 2.7 are organized as follows: part *a* gives the geometry of the system, where is drawn two neighboring unit cells, zooming in on the interface region. In part b is shown the effective permittivity ε of the structure, with its real part ε' plotted with solid lines and the imaginary part ε'' with dotted lines. The effective permeability is rendered in part *c*, again with solid (dotted) lines for the real (imaginary) part μ' (μ''). In part *d* is plotted the corresponding effective refractive index $n = \pm\left[(\varepsilon/\varepsilon_0)(\mu/\mu_0)\right]^{1/2}$ calculated from parts *b* and *c*, with similar convention for the real (n') and imaginary (n'') parts. Finally, in part *e* is shown the dispersion relation obtained from the effective parameters ε and μ. The same type of lines are used for the real (k') and imaginary (k'') wave vector components. Note that are used dashed lines in the region $|\mathbf{k}| > \pi/2a$ where the quantitative description given by this homogenization theory is suspect. Nevertheless, the description is still expected to be useful qualitatively. In Fig. 2.8 are summarized the general behavior of this structure.

As was pointed out by Pendry et al [50], the electromagnetic behavior of this kind of structures strongly depends on the connectivity of the wires. For the case of continuous wires (Fig. 2.5) the system presents a plasma-like behavior and a low-frequency band gap occurs (part *e*). Inside of this band gap region (shaded zones) the effective parameters ε and μ have opposite signs, namely $\varepsilon < 0$ and $\mu \geq 1$, and the corresponding effective refractive index *n* is imaginary. The arrow in part *e* indicates the effective plasma frequency obtained from Eq. (2.85). The difference between Eq. (2.85) and the numerical result decreases as the wires become thinner. This is because Eq. (2.85) was derived assuming very thin wires. It is important to note that the system of connected metallic wires has been recently investigated by Silveirinha, employing the homogenization method of Ref. [76].

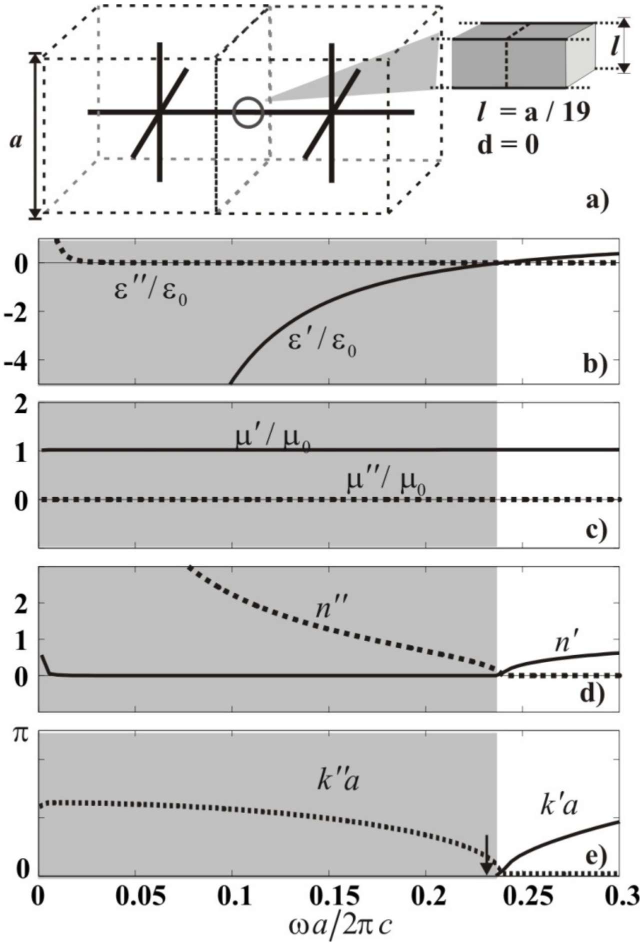

Fig. 2.5. Effective parameters of a cubic lattice of continuous metallic wires (3D crosses) of square cross-section (chosen for computational convenience). The system is depicted in part *a* where is zoomed in on the interface region between two neighboring unit cells. The effective permittivity and permeability are plotted in parts *b* and *c*, respectively. The corresponding effective refractive index is presented in part *d*. The dispersion relation $\omega(k)$, calculated from ε and μ, is plotted in part *e*, where the arrow indicates the effective plasma frequency obtained from Eq. (2.85). Shaded regions indicate the photonic band gap where n is imaginary. The system presents a plasma-like behavior.

When the thin wires are severed, the plasma-like behavior disappears and a free-photon-like behavior emerges (Fig. 2.6).

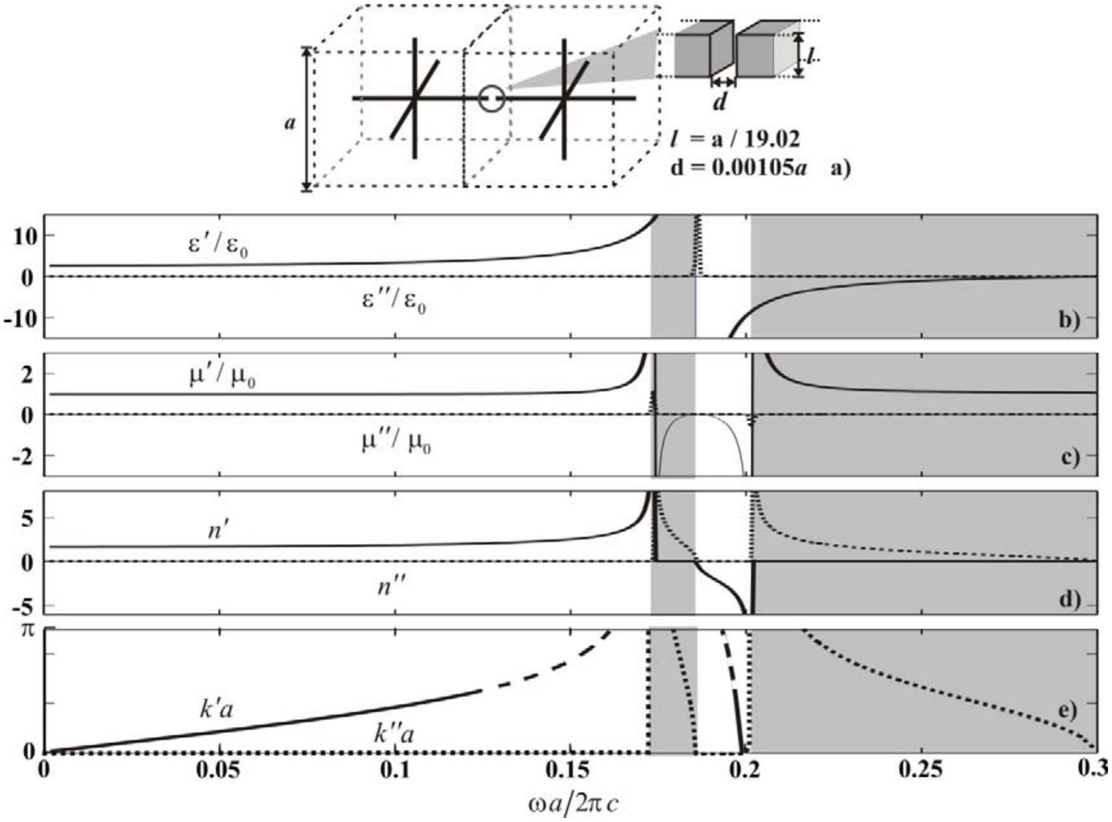

Fig. 2.6. Effective parameters for a PC formed of three-dimensional metallic crosses being separated by a small gap. The system is depicted in part *a* where is zoomed in on the interface region between two neighboring unit cells. The effective permittivity and permeability are plotted in parts *b* and *c*, respectively. The corresponding effective refractive index is presented in part *d*. The dispersion relation $\omega(k)$ calculated from ε and μ is plotted in part *e*. Shaded regions describe photonic band gaps where n is imaginary or complex. The first (acoustic) pass-band is characterized by a real and positive n whereas the second (optical) band is characterized by a real and negative n. Long-dashed lines indicate large k values for which our calculations in the limit $k \to 0$ cannot be trusted.

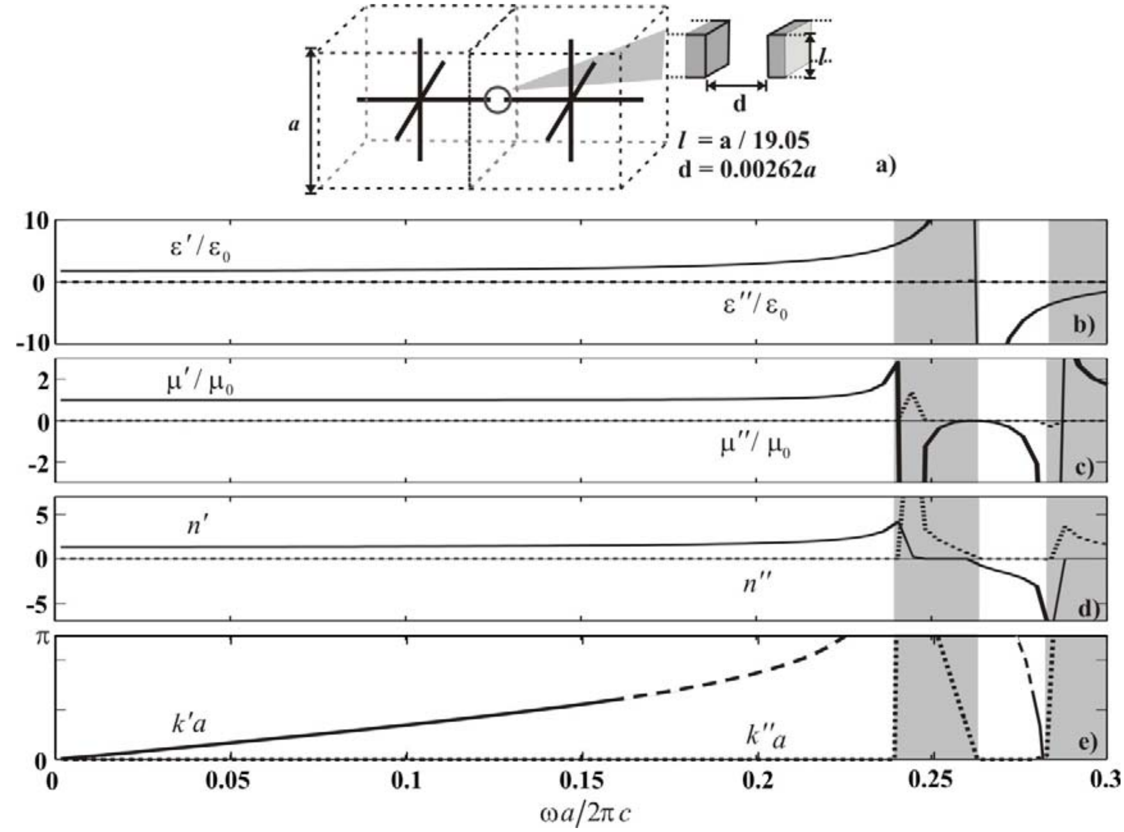

Fig. 2.7. Same as Fig. 2.6 but with a larger gap between wires in neighboring cells. The behavior of the system is similar to that in Fig. 2.6 but shifted to higher frequencies.

Now, low-frequency propagation of transverse modes is allowed as is shown in Fig. 2.6e. It is important to note that this cut in the wires also creates a resonance and an anti-resonance in ε and μ (parts *b* and *c*). This situation results in two high-frequency band gaps (shaded zones) where the effective refractive index (part *d*) is an imaginary or complex number. These band gap regions can move to higher frequencies if the separation between the wires is increased as in Fig. 2.7. Again, this theory correctly describes the system previously investigated by Pendry [50].

The regions of $\operatorname{Im}\mu(\omega) < 0$ in the Figs. 2.6 and 2.7 should not be considered breaches of causality, but are associated with the fact that the wavelength $2\pi c/\omega$ is only ~5 times greater than the lattice constant *a*. Thus, homogenization is not ideally applicable in this region, as argued in Ref. [19].

2.7.5 Doubly negative (left-handed) behavior

Now, will be analized the second (optical) pass-band in the case of cut wires (Figs. 2.6 and 2.7). In this spectral region both ε and μ are real and negative. In calculating *n* $\left(n = \pm\sqrt{\varepsilon\,\mu}\right)$ we should take the negative sign of the square root as was pointed out by Veselago [48]. In this region, the metallo-dielectric PC has left-handed behavior as a consequence of the strong capacitance produced by the small gap between the wires and the induced eddy currents [14]. It is important to stress here that have been selected thin wires in order to shift the band gap to sufficiently low frequencies (long wavelength limit). That is why were chosen gaps as small as $d = 0.00105a$ and $d = 0.00262a$. The same *metamaterial* behavior can be found in similar systems with wider gaps and thicker wires. In Fig. 2.8 we can see the effect of severing the wires. When the wires are continuous the system behaves as a plasma-like effective medium with a low-frequency band gap characterized by an imaginary refractive index (part a). A gap in the wires causes a qualitative change in the behavior at the macro-level and creates an acoustic pass-band where the index n is real and positive. This cut also creates a doubly negative region in the optical pass-band where n is real and negative (Fig. 2.6d). As the gap between the wires is increased (Fig. 2.7d), the same behavior is observed but shifted to higher frequencies.

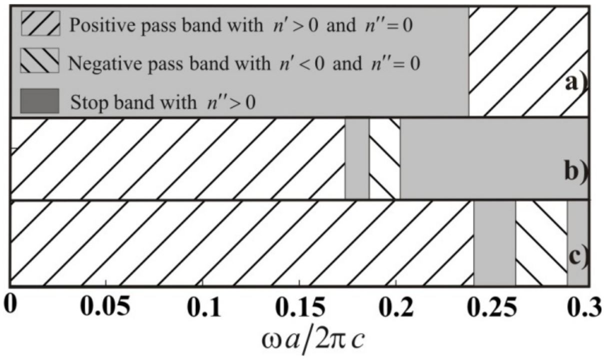

Fig. 2.8. Summary of Figs. 2.5, 2.6 and 2.7. The figure shows the effect of severing the wires in a PC of three-dimensional metallic crosses in a cubic lattice. For continuous wires (part *a*), the system presents a low-frequency band gap (plasma-like behavior). When the wires are cut (part *b*), the plasma-like behavior disappears and the propagation of low frequency waves is allowed. Cutting the wires also creates a region with a real and negative refractive index. When the gap is increased (part c), the stop bands are shifted to higher frequencies, as is also the metamaterial region ($n < 0$).

It should be remarked here that the term *metamaterial* can be also applied to the system of 2D metallic wires, studied in this section 2.6. It was shown that this PC, composed of nonmagnetic materials presents diamagnetic or paramagnetic behavior, depending on the polarization of the incident wave, being diamagnetic for the H-mode and paramagnetic for the E-mode.

Finally, it is important to stress that even though the figures shown in this section are based on formulas (2.59)-(2.62), obtained in the limit $k \to 0$, they can be reasonably used in the weakly non-local region where $|\mathbf{k}| < \pi/2a$.

2.8 Conclusion

We have developed a general homogenization theory for calculating the bulk electromagnetic response of a PC in the long-wavelength limit. By applying this mean field theory, were derived analytic expressions (requiring matrix inversions) for the effective dyadics of both the usual dielectric response and the bi-anisotropic response, with these dyadics expressed in terms of the unit cell and Bravais lattice. These permittivity ($\overleftrightarrow{\boldsymbol{\varepsilon}}$), permeability ($\overleftrightarrow{\boldsymbol{\mu}}$), and crossed magneto-electric ($\overleftrightarrow{\boldsymbol{\gamma}}, \overleftrightarrow{\boldsymbol{\delta}}$) dyadics have all been expressed in terms of a basic conductivity dyadic ($\overleftrightarrow{\boldsymbol{\Sigma}}$), for which have been included two equivalent formulas; one gives a more physical understanding of the homogenization process and the other is more convenient from the computational point of view. Unlike the non-local dielectric response, the bi-anisotropic metamaterial response allows the magnetic properties to emerge at the macro-level. It also has the advantage that the dyadics $\overleftrightarrow{\boldsymbol{\varepsilon}}$, $\overleftrightarrow{\boldsymbol{\mu}}$, $\overleftrightarrow{\boldsymbol{\gamma}}$, and $\overleftrightarrow{\boldsymbol{\delta}}$ are independent of the magnitude of the wave vector (although they can depend, in general, on its direction). It is interesting that the permeability dyadic $\overleftrightarrow{\boldsymbol{\mu}}$ of the bi-anisotropic response diagonalizes in a coordinate system with one axis parallel to the wave vector k. Therefore, the principal axes of the permittivity $\overleftrightarrow{\boldsymbol{\varepsilon}}$ and permeability $\overleftrightarrow{\boldsymbol{\mu}}$ dyadics in general do not coincide, high-symmetry configurations being the exception. This situation could lead to new results in the Crystal Optics of periodic composites. Within this homogenization theory, the crossed magneto-electric dyadics ($\overleftrightarrow{\boldsymbol{\gamma}}$, $\overleftrightarrow{\boldsymbol{\delta}}$) of the bi-anisotropic response vanish in the limit $k \to 0$ if the unit cell possesses inversion symmetry. Hence, in this important case the response is given entirely in terms of $\overleftrightarrow{\boldsymbol{\varepsilon}}$ and $\overleftrightarrow{\boldsymbol{\mu}}$. Even in this relatively simple situation, the physics of anisotropic metamaterials is still very rich (see, for example, Rosa et al [53, 63]). This theory was verified by reducing the general results to those obtained in previous works: analytically, to the Maxwell-Garnett formula for small spheres and to the Pendry effective permittivity for a 3D system of metallic wires ("3D crosses") and numerically, for dielectric 2D cylinders and 3D spheres. Moreover, were presented numerical results for metallo-dielectric photonic crystals. In contrast with the pure dielectric case where there are no magnetic effects, here have been found paramagnetic and diamagnetic behavior in 2D PC's of metallic wires, depending on the polarization – respectively parallel and perpendicular to the wires. Were studied in detail, numerically, 3D systems of mutually perpendicular wires ("3D crosses"), focusing on the transition from continuous wires to cut wires and determining the effect of the width of the gap created between the severed wires. This leads to the disappearance of the low-frequency stop band (for the continuous wires) and its replacement by an "acoustic" pass band (for the cut wires). The second ("optical") pass band is characterized by both the permittivity and the permeability being negative. This metamaterial behavior results from the capacitance created in the gaps between wires and the eddy currents induced by the magnetic field.

The theory presented in this chapter bridges the gap between the photonic crystal or micro-level description and the uniform or macro-level description. It is based on first principles, characterizing the photonic crystal by means of a position-dependent generalized conductivity. It is a classical mean-field theory in the spirit of Solid State theory. In principle, the final formulas for the bianisotropic response ($\overleftrightarrow{\boldsymbol{\varepsilon}}$, $\overleftrightarrow{\boldsymbol{\mu}}$, $\overleftrightarrow{\boldsymbol{\gamma}}$ and $\overleftrightarrow{\boldsymbol{\delta}}$) can be applied to one-, two-, and three-dimensional photonic crystals with arbitrary Bravais lattices and arbitrary composition of the unit cell. The ensuing numerical work involves matrix inversion and reciprocal lattices summation. On the downside, convergence can be slow, computer memory – insufficient, and computation times – lengthy.

The derived effective material dyadics $\overleftrightarrow{\boldsymbol{\varepsilon}}$, $\overleftrightarrow{\boldsymbol{\mu}}$, $\overleftrightarrow{\boldsymbol{\gamma}}$, $\overleftrightarrow{\boldsymbol{\delta}}$ can depend on the frequency – not, however, on the magnitude of the Bloch wave vector k. Nevertheless, this work could be readily generalized to first or second order in $|\mathbf{k}|$. In the case of 2D PCs, it should be interesting to investigate out-of-plane propagation. Finally, it should be also commented that application of this theory to optical response (say, of a periodic composite slab) would also require long vacuum wavelength ($2\pi c/\omega \gg a$), in addition to long Bloch wavelengths ($2\pi/k \gg a$).

Chapter 3

Mean-field description of two-dimensional photonic crystals: Axial propagation.

(MS by J. A. Reyes-Avendaño and P. Halevi, in preparation)

This chapter is devoted to the study the axial propagation of electromagnetic waves in a two-dimensional photonic crystal in the limit of long wave-lengths by describing the periodic structure in terms of the effective permittivity. As a consequence of the translational symmetry for this direction of propagation, special attention is paid to the nature of the wave vector (**k**). In contrast with the in-plane propagation where **k** is a Bloch wave vector, for the axial propagation **k** is an ordinary wave vector with no restrictions on its magnitude. Taking into account this important point and using the generalized conductivity $\hat{\boldsymbol{\sigma}}(\mathbf{r})$ as the only parameter describing the unit cell, a very general expression for the effective permittivity is derived, in a similar way as was done in chapter 2. This very general formula is used to study both, dielectric and metallo-dielectric photonic crystals. Moreover, in order to give a complete description for this axial direction of propagation, a study of the wave polarization is performed for the first three bands by plotting the three components of the electric and magnetic fields within the unit cell. This procedure allows to determine which of the three principal elements of the dielectric dyadic is involved in the wave propagation.

3.1 Introduction

Since their apparition, Photonic Crystals (PCs) have been intensely studied because they offer wide ranging possibilities to manipulate electromagnetic-waves. This arises from three important factors: the periodicity of the system (in one-, two-, or three-dimensions), the dielectric contrast among the materials employed in their composition, and the wavelength used in the experiment. By an appropriate selection of the materials and shape of the PC's building blocks it is possible to obtain, for example, an artificial material that inhibits the light propagation in a band of frequencies when the wave-length is of the same order as the lattice constant ($\lambda \approx a$) [3]. On the other hand, when λ is much greater than a ($\lambda \gg a$), it is possible to design structures called metamaterials that give rise to negative refraction [11-13] among other interesting phenomena.

In particular, two-dimensional photonic crystals (2D PC) have been preferred because they have advantages in mode-confinement over the one-dimensional PCs and are much easier to fabricate than three-dimensional PCs. Moreover, their inclusion in integrated planar optics is natural [77]. The major effort in studying 2D PC has been focused on the propagation of electromagnetic waves in the plane of periodicity, resulting in several applications, as wave-guides [5] and optical switches [78] when

$\lambda \approx a$, and more recently, structures with negative permittivity [49] or negative permeability [50] when $\lambda \gg a$. Nevertheless, there is an interesting possibility of the wave vector k not being restricted to the plane of periodicity, i.e., $k_z \neq 0$ [79-84]. For example, there exists an off-plane angle dependence of the photonic band gaps in a 2D PC that can be used to improve the control of spontaneous emission [85]. Also, it has been found that a lattice of air cylinders embedded in a dielectric matrix posseses an omnidirectional absolute band gap [86, 87]. The latter implies that a 2D PC could have some functionalities of a 3D PC.

All the aforementioned studies for out-of-plane propagation have centered their attention in the frequency region where $\lambda \approx a$. In contrast, very few references are dealing with the out-of-plane propagation in the long wave-length limit $\lambda \gg a$. Probably, the first attempt to study such a situation was done by Feng and Arakawa [85] introducing a simple model for the effective refractive index in order to predict the off-plane angle dependence of the band gap. A deeper analysis was done by Krokhin et. al. [25] for 2D PCs. The mean field theory developed in Ref. [25] covers in-plane and off-plane propagation, giving explicit formulas for the effective permittivity in both cases. Nevertheless, the theory is restricted to acoustic bands for dielectric structures in the limit $\omega, k \to 0$ and is not applicable in the case of metallo-dielectric structures. On the other hand, Belov and collaborators [88] focused their attention on a parallel conducting wire medium in the long-wavelength limit. They showed that a complete description of this medium by means of a dielectric tensor, must take into account the off-plane wave vector component.

In the previous chapter we studied in detail the propagation of electromagnetic waves in PCs when the Bloch wave vector goes to zero ($\mathbf{k}_B \to 0$). In this limit, the periodic structure behaves as a homogeneous medium and can be described in terms of effective parameters. These effective parameters were derived by describing the periodic structure using a generalized conductivity at every point in the unit cell which allows the description of dielectric and metallo-dielectric PCs. Then, the electromagnetic fields were averaged over many unit cells considering small Bloch wave vectors in comparison with the inverse lattice constant [89, 90]. Because the Bloch wave vector was taken as the only wave vector characterizing the EW, the study was restricted to axial propagation in the case of 1D PCs and to the in-plane propagation in the case of 2D PCs.

This chapter expands and completes the previous work [89, 90] for the case of 2D photonic crystals. Now, the same ideas developed previously are used to study the propagation of electromagnetic waves perpendicular to the plane of periodicity in a 2D PC in the limit of long Bloch wavelengths. This time, special attention is paid to the axial wave vector which does not experience the periodicity of the system and behaves as an ordinary wave vector in a homogeneous medium. This point has strong repercussions for the homogenization process, for instance, the magnetic effects are absent, thus reducing the bi-anisotropic response derived in the previous chapter to the dielectric response. Finally, the polarization for the first three bands is analyzed by plotting the electric and magnetic fields within the unit cell. This procedure reveals which element in the effective dielectric dyadic is involve in the wave propagation.

The chapter is organized as follows. The introduction was given in Sec. 3.1. In Sec. 3.2 we derive the general formulae that lead to homogenization a 2D PC for the case of axial propagation. In section 3.3 the polarization is analyzed for the first two bands and the numerical results are presented for the effective permittivity of dielectric and metallo-dielectric structures. In section 3.4 a comparison with experimental results is performed. The conclusions are given in section 3.5. Finally, the general method used to compute the band structure and an analysis of convergence are given in Appendix G and H respectively.

3.2 Homogenization process.

As starting point, it should be note that in a 2D PC it is possible to split the wave vector in two components which have a very different behavior,

$$\mathbf{k} = \mathbf{k}_B + \mathbf{k}_z . \tag{3.1}$$

The first component $\mathbf{k}_B$, is the Bloch wave vector laying in the plane of periodicity. This component can be restricted to the first Brillouin zone and in the long wavelength limit, it must be much smaller than the inverse lattice constant *a*

$$k_B a \ll 1 . \tag{3.2}$$

On the other hand, $\mathbf{k}_z$ is the component perpendicular to the plane of periodicity. Because $\mathbf{k}_z$ points in a translationally invariant direction, it is an ordinary wave vector and no restrictions are imposed over it. Hence, the long wavelength limit Eq. (3.2) is *not* applicable for this component. This is so, because the properties of our 2D photonic crystal are independent of the z-coordinate.

In the following the special case of axial propagation will be studied, then Eq. (3.1) simplifies to:

$$\mathbf{k} = \mathbf{k}_z = k_z \hat{\mathbf{z}} . \tag{3.3}$$

Now, despite the invariance in the z-direction, the electromagnetic fields associated still experience the periodicity of the system [25]. In the long wavelength limit, this interaction can be studied by obtaining the effective parameters, namely, the effective permittivity and the effective permeability although other magneto-electric parameters are possible [2, 91].

The aforementioned effective parameters can be derived by averaging the electromagnetic fields within the PC over many unit cells, as is proposed in Refs. [89] and [90]; the calculation below closely follows these references. This averaging procedure smooths out the rapid oscillations within the unit cell. In a Fourier expansion, these oscillations are described by the terms with $\mathbf{G} \neq 0$, therefore, the average electric field and magnetic induction could be defined as

$$\mathbf{E}(\mathbf{r}) \equiv \langle \mathbf{e}(\mathbf{r}) \rangle = \mathbf{e}(\mathbf{G}=0)e^{ik_z z} = \mathbf{E}_0 e^{ik_z z}, \tag{3.4}$$

$$\mathbf{B}(\mathbf{r}) \equiv \langle \mathbf{b}(\mathbf{r}) \rangle = \mathbf{b}(\mathbf{G}=0)e^{ik_z z} = \mathbf{B}_0 e^{ik_z z}, \tag{3.5}$$

where $\mathbf{e}(\mathbf{r})$ and $\mathbf{b}(\mathbf{r})$ are the electric field and magnetic induction at the micro-level, <…> indicates the average and the wave propagation has been fixed parallel to the cylinders. In order to study dielectric and metallo-dielectric structures it is convenient to describe the unit cell by only a single material scalar field with the same periodicity as the PC, namely the position-dependent generalized conductivity:

$$\hat{\sigma}(\mathbf{r}) = \sigma(\mathbf{r}) - i\omega\varepsilon_0\chi(\mathbf{r}), \tag{3.6}$$

where σ(r) and χ(r) are, correspondingly, the usual conductivity and susceptibility for isotropic materials in the unit cell. In terms of this effective conductivity, the current density **j** is given by

$$\mathbf{j}(\mathbf{r}) = \hat{\sigma}(\mathbf{r})\mathbf{e}(\mathbf{r}). \tag{3.7}$$

Note that this current density is entirely produced by the internal electric field of the PC. Because of the periodicity, the generalized conductivity can be expanded in a Fourier series,

$$\mathbf{j}_0 = \hat{\sigma}(\mathbf{G}=0)\mathbf{e}(\mathbf{G}=0) + \sideset{}{'}\sum_{\mathbf{G}} \hat{\sigma}(-\mathbf{G})\mathbf{e}(\mathbf{G})\,, \tag{3.8}$$

where the primes indicate that the term with G = 0 is excluded from the sums. To express the quantities $\mathbf{e}(\mathbf{G} \neq 0)$ in terms of $\mathbf{e}(\mathbf{G}=0)$, is possible to use the wave equation

$$\nabla \times \nabla \times \mathbf{e}(\mathbf{r}) = \left[i\mu_0 \omega \hat{\sigma}(\mathbf{r}) + k_0^2 \right] \mathbf{e}(\mathbf{r})\,, \tag{3.9}$$

which is obtained by eliminating the magnetic induction from de Ampére-Maxwell law and Faraday's law with $k_0^2 = \mu_0 \varepsilon_0 \omega^2$. After some algebra it is possible to write

$$(\mathbf{k}_z + \mathbf{G}) \times (\mathbf{k}_z + \mathbf{G}) \times \mathbf{e}(\mathbf{G}) + k_0^2 \mathbf{e}(\mathbf{G}) = -i\omega\mu_0 \sum_{\mathbf{G}'} \hat{\sigma}(\mathbf{G}-\mathbf{G}')\mathbf{e}(\mathbf{G}')\,. \tag{3.10}$$

This equation can be rewritten in dyadic notation as

$$\sideset{}{'}\sum_{\mathbf{G}'} \overleftrightarrow{\mathbf{M}}(\mathbf{k}_z;\mathbf{G},\mathbf{G}') \cdot \mathbf{e}(\mathbf{G}') = i\omega\mu_0 \hat{\sigma}(\mathbf{G})\mathbf{e}(0), \quad \mathbf{G} \neq 0\,, \tag{3.11}$$

where the dyadic $\overleftrightarrow{\mathbf{M}}(\mathbf{k}_z;\mathbf{G},\mathbf{G}')$ is defined for $\mathbf{G} \neq 0$ and $\mathbf{G}' \neq 0$ as

$$\overleftrightarrow{\mathbf{M}}(\mathbf{k}_z;\mathbf{G},\mathbf{G}') = \left[\left(\left| \mathbf{k}_z + \mathbf{G} \right|^2 - k_0^2 \right) \overleftrightarrow{\mathbf{I}} - \left(\mathbf{k}_z + \mathbf{G} \right) \left(\mathbf{k}_z + \mathbf{G} \right) \right] \delta_{\mathbf{G},\mathbf{G}'} - i\omega\mu_0 \hat{\sigma}(\mathbf{G}-\mathbf{G}') \overleftrightarrow{\mathbf{I}}\,. \tag{3.12}$$

Here, $\overleftrightarrow{\mathbf{I}}$ and $\delta_{\mathbf{G},\mathbf{G}'}$ are, respectively, the unit dyadic and the Kronecker delta. Solving Eq. (3.11) for $\mathbf{e}(\mathbf{G} \neq 0)$, it is found the expression

$$\mathbf{e}(\mathbf{G}) = i\omega\mu_0 \sum_{\mathbf{G}'}{}^{'} \overleftrightarrow{\mathbf{M}}^{-1}(\mathbf{k}_z;\mathbf{G},\mathbf{G}')\hat{\sigma}(\mathbf{G}')\cdot\mathbf{e}(0), \quad \mathbf{G} \neq 0 . \tag{3.13}$$

After substituting this expression in Eq. (3.8), we finally obtain the macroscopic current density in the form

$$\mathbf{j}_0 = \overleftrightarrow{\mathbf{\Sigma}}(\mathbf{k}_z)\cdot\mathbf{E}_0 , \tag{3.14}$$

where $\overleftrightarrow{\mathbf{\Sigma}}(\mathbf{k}_z)$ is the effective conductivity dyadic:

$$\overleftrightarrow{\mathbf{\Sigma}}(\mathbf{k}_z) = \hat{\sigma}(\mathbf{G}=0)\overleftrightarrow{\mathbf{I}} + i\omega\mu_0 \sum_{\mathbf{G},\mathbf{G}'}{}^{'} \hat{\sigma}(-\mathbf{G})\overleftrightarrow{\mathbf{M}}^{-1}(\mathbf{k}_z;\mathbf{G},\mathbf{G}')\hat{\sigma}(\mathbf{G}') . \tag{3.15}$$

In terms of the average fields and the effective conductivity, the Ampere-Maxwell equation can be written as

$$\mathbf{k}\times\mathbf{B}_0 = -\mu_0\left[\omega\varepsilon_0\overleftrightarrow{\mathbf{I}} + i\overleftrightarrow{\mathbf{\Sigma}}(\mathbf{k}_z)\right]\cdot\mathbf{E}_0 , \tag{3.16}$$

Comparing the last equation with the corresponding equation for a macroscopic homogeneous medium:

$$\mathbf{k}\times\mathbf{H} = -\omega\mathbf{D} , \tag{3.17}$$

it is possible to define the effective parameters $\overleftrightarrow{\boldsymbol{\varepsilon}}$ and $\overleftrightarrow{\boldsymbol{\mu}}$ as:

$$\overleftrightarrow{\boldsymbol{\varepsilon}}(\mathbf{k}_z,\omega)=\varepsilon_0\overleftrightarrow{\mathbf{I}}+\frac{i}{\omega}\overleftrightarrow{\boldsymbol{\Sigma}}(\mathbf{k}_z,\omega)\,, \tag{3.18}$$

$$\overleftrightarrow{\boldsymbol{\mu}}=\mu_0\overleftrightarrow{\mathbf{I}} \tag{3.19}$$

Clearly, the last description establishes that there are not magnetic effects for the axial propagation, i.e. $\mu=\mu_0$. In contrast with the case of in-plane propagation where it is possible to associate some magnetic effects with the small parameter $\mathbf{k}_B$ [89, 90], here $\mathbf{k}_B$ is strictly equal to 0 and the magnetic effects disappear. On the other hand, the effective permittivity is a function of the frequency ω and the wave vector $\mathbf{k}_z$ in agreement with the results obtained by Belov [88] for the case of metallo-dielectric structures. Although there is no direct restriction over the ordinary wave vector $\mathbf{k}_z$, the homogenization process requires that the amplitude of the electromagnetic fields within the unit cell varies slowly. The latter implies that the electromagnetic wave's frequency has to remain low and, in consequence, $\mathbf{k}_z$ cannot be arbitrarily large.

Finally, it is important to note that in the case of a 2D PC having mutually perpendicular mirror planes, the following equation is satisfied:

$$\hat{\sigma}(-\mathbf{G}_x,\mathbf{G}_y)=\hat{\sigma}(\mathbf{G}_x,\mathbf{G}_y)=\hat{\sigma}(\mathbf{G}_x,-\mathbf{G}_y)\,. \tag{3.20}$$

As a consequence of Eq. (3.20), the effective permittivity (Eq. (3.18)) is a diagonal dyadic for this kind of systems. Then, the dispersion relation for the axial propagation in the homogenized medium can be written as:

$$\left[\omega^2\varepsilon_{xx}(\omega)-k_z^2/\mu_0\right]E_x\hat{\mathbf{x}}=0$$

$$\left[\omega^2\varepsilon_{yy}(\omega)-k_z^2/\mu_0\right]E_y\hat{\mathbf{y}}=0 \tag{3.21}$$

$$\varepsilon_{zz}(\omega)E_z\hat{\mathbf{z}}=0$$

Equation (3.21) indicates that in principle, longitudinal and transversal electromagnetic waves can propagate through the system. Two polarizations are supported for transversal waves, one with its electric field parallel to the *x* axis and the other with its electric field parallel to the *y* axis. These two modes are degenerate if there is isotropy in the plane of periodicity. On the other hand, longitudinal waves can propagate only if ε_{zz} is strictly equal to zero for a finite frequency.

3.3 Numerical results

In this section the effective permittivity is computed for different dielectric and metallo-dielectric PCs in the case of axial propagation. The effective permittivity derived in the previous section is at the same time frequency- and wave vector-dependent (see Eqs. (3.18) and (3.15)), thus, it is important to obtain a priori the relation between these two quantities, namely, the dispersion relation $\omega(k)$ (see Appendix G). If the aforementioned relation is not used in solving Eq.(3.18), the resulting $\vec{\vec{\boldsymbol{\varepsilon}}}$ would lead to unphysical results. In addition, the polarization of each mode must also be defined in order to select the component of $\vec{\vec{\boldsymbol{\varepsilon}}}$ that is involved in the wave propagation. Figure 3.1 shows all the information required to compute Eq. (3.18) and the effective permittivity for the first two bands. The system consists of a square lattice of silicon cylinders surrounded by air with a filling fraction $f=0.1$. Part *i* of Fig. 3.1 shows the dispersion relation $\omega(k)$ for the axial propagation. The first band in this figure is a degenerate band with two different modes that have been labeled as *A* and *B*. Subfigures *ii* and *iii* show the three components of the electric and magnetic field respectively. Both fields have been plotted inside of 9 unit cells for the first three modes (*A*, *B* and *C*) with $k_{zn} = 0.05$.

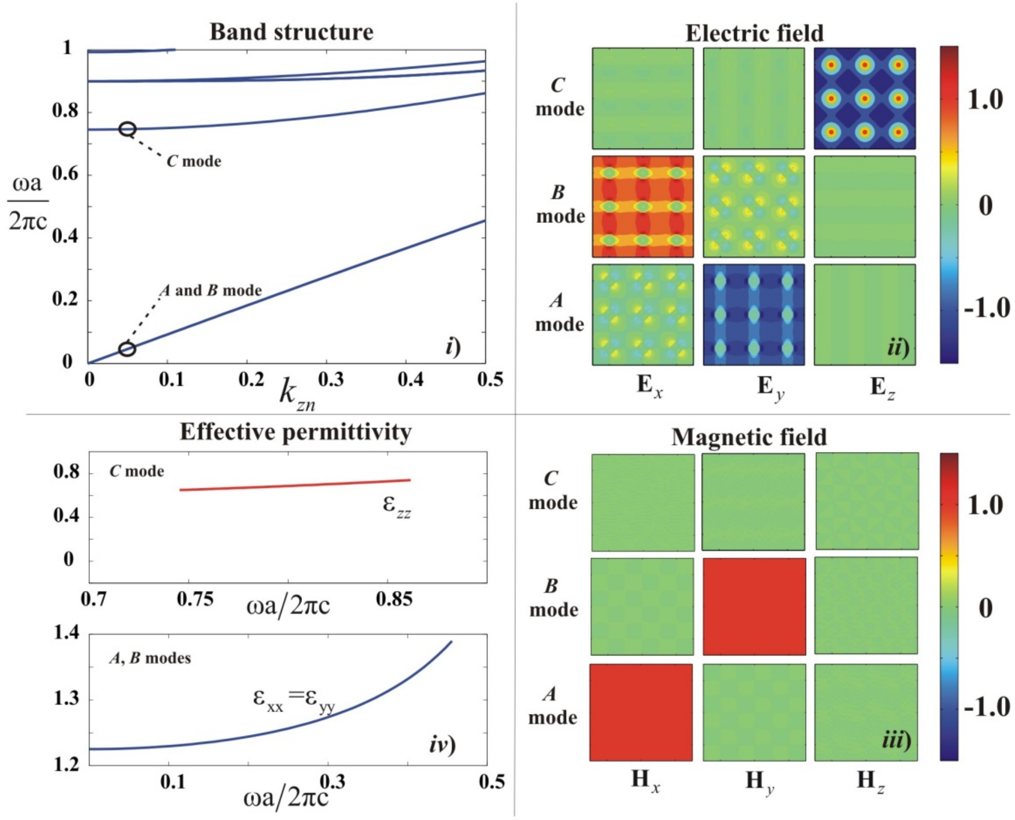

Fig. 3.1. *i*) Band structure for the axial propagation of a square lattice of silicon cylinders with a filling fraction $f = 0.1$. Right side of the figure shows the electric (*ii*) and magnetic (*iii*) fields for the three modes marked with a circle in the band structure. The degenerate modes *A* and *B* have a transversal polarization, while the *C* mode has a longitudinal polarization. Part *iv*) shows the effective permittivity computed for the first two bands. Because of the strong oscillation of $E_z(\mathbf{r})$ within the unit cell observed for the second band, the homogenization process fails in obtain the correct answer $\varepsilon_z = 0$. Nevertheless, the magnetic field $\mathbf{H}(\mathbf{r})$ vanishes for this longitudinal mode, as it should.

These two figures show that the *A* and *B* modes have a transversal polarization with their electric and magnetic fields oscillating in the plane of periodicity. In contrast, the *C* mode has a longitudinal polarization with its electric field parallel to the wave vector $\mathbf{k}_z$. The subfigures *ii* and *iii* also give information about the wave fronts that propagate inside of the PC. It is interesting to note that even for the *A* and *B* modes with $\mathbf{k}_B = 0$, $\mathbf{k}_{zn} = 0.05$ and $\omega a/2\pi c \approx 0.05$, the electric field shows oscillations within the unit cell. Therefore, for axial propagation in the long wavelength limit, the wave that propagates in the PC is not a pure plane wave (as occurs for in-plane propagation) but it exhibits a periodic dependence along the *x* and *y* directions. This behavior was predicted in Ref. [25]. Nevertheless, the structure can be still described by using a mean field theory but with a reduced precision because the oscillations within the unit cell will disappear during the homogenization process. This approximate description is expected to be useful for describing the classical optical phenomena provided that the oscillations within the unit cell remain small in comparison the average magnitude of the electric field (weak homogenization).

In contrast with the modes *A* and *B*, the electric field for the *C* mode shows strong oscillations and the homogenization process will not be a good approximation. Nevertheless, equation (3.21) implies that the effective permittivity for this mode must to be equal to zero. Finally, part *iv* of Fig. 3.1 shows the effective permittivity computed for the first three modes of part *i*. The results obtained for the *A* and *B* modes are expected to be a good approximation as long as the frequency remains small. On the other hand, the homogenization process fails to give the correct answer ($\varepsilon_{zz} = 0$) for the *C* mode. As will be shown later, if the frequency of the *C* mode is lower, the oscillations within the unit cell are smaller and the homogenization process gives the right value.

Figure 3.2 shows the effective permittivity for the first band (*A* and *B* modes) as a function of the filling fraction. This time the cylinders form a triangular lattice. The right side of the figure corresponds to silicon cylinders in air and the left side of the figure to air cylinders in a silicon matrix. Four different values of the wave vector are considered. Solid lines correspond to the effective permittivity obtained from the homogenization theory by using 887 plane waves in the computation. Dotted lines correspond to the effective permittivity calculated from de dispersion relation $\varepsilon_{\perp} = \left(k_z c/\omega\right)^2$. In general, there is good agreement between both results with the exception of some points with high filling fractions, especially, when the interstitial region between the cylinders has a high dielectric constant in comparison with the cylinders (left side of figure). The agreement in this region can be improved by increasing the number of plane waves used in the computation. The results shown in Fig. 3.2 demonstrate that our mean field theory can be used to study the axial propagation of electromagnetic waves in a 2D dielectric PC as long as the frequency is low enough. In practice, this means that $\omega \leq 0.4$ should be observed.

Figure 3.3 shows the dispersion relation and the corresponding effective permittivity for a square lattice of metallic wires. In the computation 1009 plane waves have been used. Left side of the figure shows the results for aluminum wires and the right side shows the results for copper wires. In both cases a very small filling fraction has been chosen in order to get a low frequency in the second band. The dispersion relations in Fig. 3.3 can be obtained by employing the methods proposed in Refs. [83, 92] or by solving the wave equation for the electric field and then, eliminating the flat bands which converge very slowly. This method is discussed in the Appendix G.

In a similar way as occurs in a dielectric structure, in a metallo-dielectric PC the first band (dashed line) has a transversal polarization and the second band (solid line) has a longitudinal polarization. In both figures, the thin line is the light line. Because the wires are very thin, the electric field oscillating in the plane of periodicity practically does not interact with the wires. Therefore, the dispersion relation for a transversal mode is very close to the light-line and the effective permittivity is almost equal to one as is shown at the bottom of figure 3.3. In contrast with the dielectric case, the second band in a metallo-dielectric PC of very thin wires has a considerably lower frequency. This ensures that the oscillations of the electric field within the unit cell remain small in comparison with the average value of the field. Hence, the homogenization process give a very good approximation to the effective permittivity value $(\varepsilon_{zz} = 0)$ as is shown in the middle of Fig. 3.3.

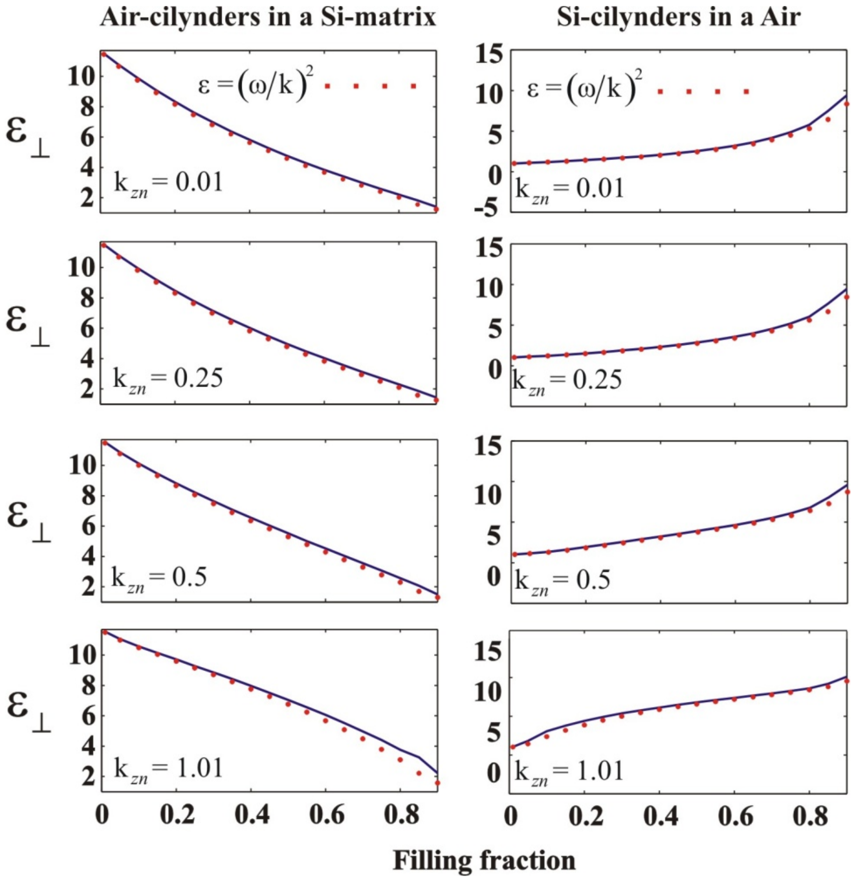

Fig. 3.2. Effective permittivity as a function of the filling fraction. Four different values of the wave vector are considered. The left side corresponds to a triangular lattice of air-cylinder in a silicon ($\varepsilon = 11.7$). The right side corresponds to the complementary structure of silicon cylinders surrounded by air. Solid lines are the results obtained from the mean field theory and the dotted lines are the results obtained from the dispersion relation.

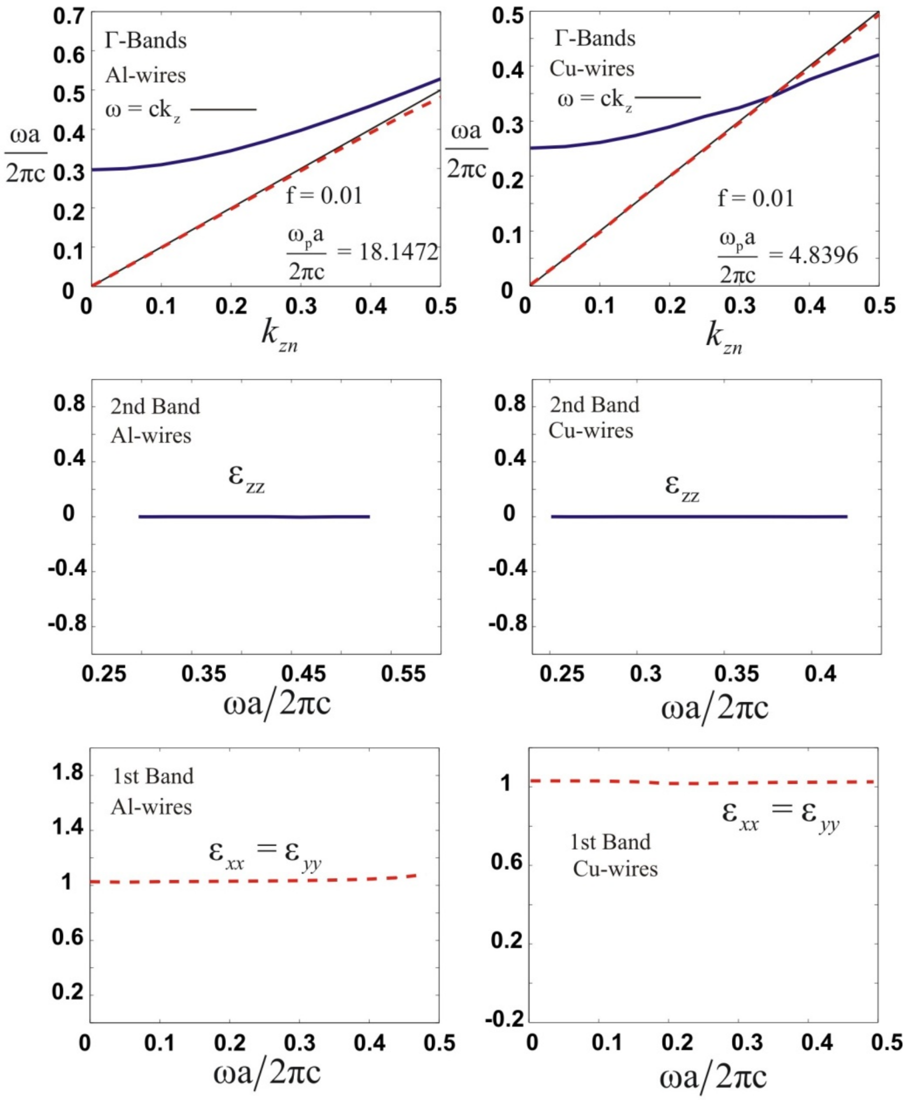

Fig. 3.3. Effective permittivity for the first two Γ bands of a square lattice of aluminum (left) and cupper (right) wires. The top of the figure shows the corresponding dispersion relations. In the middle are shown the effective permittivities for the second (optical) band. The bottom of the figure shows the effective permittivity for the first (acoustic) band. In both cases the lattice constant is $a = 1.5 \times 10^{-4} cm$.

3.4 Comparison with experimental results.

In this section are compared the numerical results obtained through this theory and the experimental results published by Shongping and Mittleman [93]. The sample used in Ref. [93] was fabricated using deep reactive ion etching to form an array of circular air holes, penetrating all the way through a 305 μm-thick high-resistivity (>10 kΩ-cm) silicon wafer. This material exhibits extremely low absorption and a frequency-independent refractive index of n_{Si}=3.418 throughout the THz range. The holes, with diameters of 360 μm, are arranged on a hexagonal lattice with spacing *a* = 400 μm. Figure 3.4 shows the comparison between the results presented in Ref. [93] and the results obtained using the homogenization process proposed in this work. The scatter graph corresponds to the effective refractive index for axial propagation obtained from the terahertz time-domain spectroscopy measurements. The horizontal dashed line indicates the predicted homogeneous limit of n_{hom}=1.6448, which is smaller than the measured low-frequency value of nmeas=1.73±0.07. The dotted curve shows the dispersion predicted by a band structure calculation for out-of-plane propagation, based on a plane wave method [25]. The solid curve is the corresponding FDTD simulation. Finally, the thick-solid line corresponds to the effective refractive index computed using this theory.

It is interesting to note that despite that this theory considers an infinite medium; the results are very close to those obtained in a very thin silicon wafer through the experiment. With the exception of low frequencies −where the experiment seems to fail− and the region around 0.45 THz, the homogenization process can be considered as a very good approximation. Of course, the results obtained by the FDTD simulation that takes into account the dimensions of the wafer are closer to the experiment. Finally, the homogenization theory presented here overcomes the results obtained by using the theory in Ref. [25]. This is expected, because in Ref. [25] small values of the wave vector k_z are required and Eq.(3.18) does not have such a restriction.

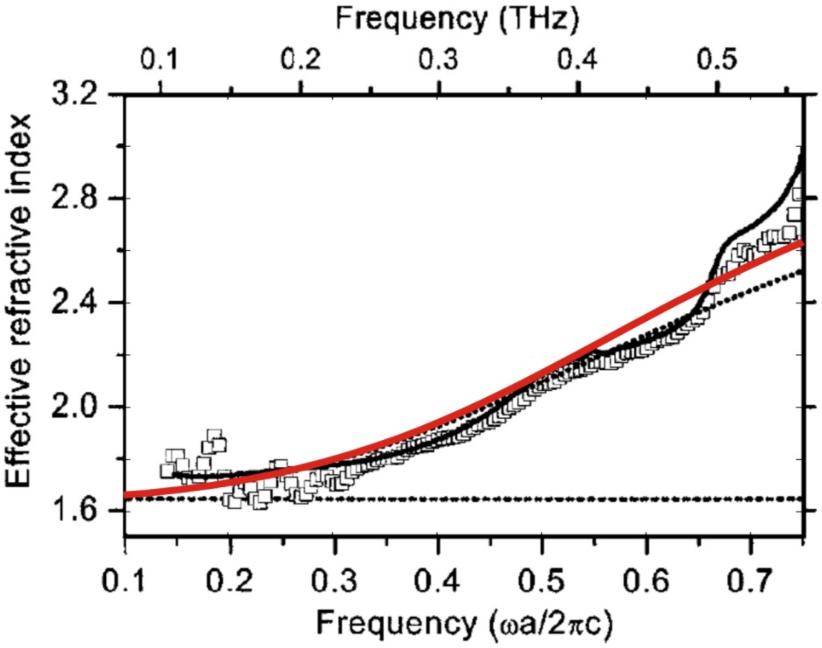

Fig.3.4. Comparison between the results presented in Ref. [93] and the results obtained using the homogenization process proposed in this work.

3.5 Conclusions

A general expression for the effective permittivity has been derived. It that can be used to study the axial propagation of electromagnetic waves in two-dimensional photonic crystals in the long-wavelength limit. The expression is frequency and wave vector dependent in agreement with other theories in the literature. Because of its generality, it can be used to analyze dielectric and metallo-dielectric structures with any shape of the inclusions. In contrast with the case of in-plane propagation studied previously, the derivation showed that there are no magnetic effects for this direction of propagation even for metallo-dielectric structures. By plotting the electric and magnetic fields within the unit cell, it was found that in the long wavelength limit, the first band in the dispersion relation has a transversal polarization while the second band has a longitudinal polarization.

In the case of dielectric structures, there was analyzed a square lattice of silicon cylinders and a triangular lattice of holes in a silicon host as well as their inverse structure. The effective permittivity computed for the first band showed good agreement with the results obtained from the dispersion relation. On the other hand, the homogenization processes fails for the second band as a consequence of the strong oscillations of the electric field within the unit cell. Nevertheless, the polarization's study carried out for the second band shows that the effective permittivity must be equal to zero as corresponds to a longitudinal polarization.

In the case of metallo-dielectric structures there has been analyzed a square lattice of thin metallic wires made of aluminum or cooper. The filling fraction has been selected to be very small in order to obtain a low frequency in the second band. This selection reduced the oscillations of the electric field within the unit cell and the homogenization process gave the correct result, $\varepsilon_{zz} = 0$. As was mentioned before, the first band has a transversal polarization with the electric field oscillating in the plane of periodicity. As a consequence of the small filling fraction, the electric field does not interact with the metallic wires and the effective permittivity is very close to that in vacuum.

Finally, the results of this theory were compared with an experiment reported in the literature. Even thought the experiment was carried out in a thin silicon wafer –not corresponding to a photonic crystal−, the effective permittivity obtained from this theory fits the experimental results very well.

Chapter 4

Electrical tuning of photonic crystals infilled with liquid crystals

(Article with the same title by Juan Adrian Reyes, J. A. Reyes-Avendaño and, P. Halevi, Opt. Comm., **281**, 2535-2547 (2008).

In this chapter a complete study is performed of electrical tuning in liquid crystal-infilled two-dimensional (2D) photonic crystals (PCs). The nematic liquid crystal (NLC) is characterized by a full range of bulk and surface elastic parameters. An essentially DC tuning field is applied in the axial direction. By minimizing the total (elastic plus electromagnetic) free energy, the configuration of the NLC directors, as a function of radial distance, is obtained. Three possible configurations are considered: escaped radial, planar radial, and axial. It is found that, in general, the escaped radial configuration is the preferred one. However, for sufficiently large applied fields, a phase transition occurs to the axial configuration. For example, in the case of the NLC *5CB*, this transition is realized at about 14 V/μm provided that the cylinder radius is greater than about 50 nm. The configuration of the NLC directors determines the dielectric tensor as function of radial distance and this, in turn, leads to the eigenvalue equation for the PC. Are presented two such equations: one exact and the other approximate. The exact eigenvalue equation is based on the full anisotropy of the dielectric tensor and does not result in the usual separation of normal modes in a 2D PC. The approximate eigenvalue equation is derived from the average (over the cylinder cross-section) dielectric tensor and leads to modes that are polarized in the directions either parallel (E-mode) or perpendicular (H-mode) to the cylinders. The calculations of the photonic band structure, by both methods, show that the approximate calculation works very well for the *5CB* NLC cylinders in a silicon oxide (silica) host. This allows to introduce the terminology quasi-E and quasi-H polarizations. It is show how the partial photonic band gap in the [100] direction for these polarizations can be tuned and even completely closed. This behavior could be applied to the design of versatile, tunable polarization filters.

4.1 Introduction

This chapter deals with two kinds of crystals, neither of which is a crystal in the usual sense. One of these is *photonic* crystal (PC) - by now a household term among condensed-matter scientists. The basic optical properties of these man-made, periodic structures, as well as numerous applications, are covered by several books [77, 94, 95, 96]. The other type of nonconventional crystal is a *liquid* crystal, characterized by some particular microscopic regularity; liquid crystals occupy an intermediate position between ordinary crystals and amorphous materials [97, 98, 99, 100, 101]. For many decades, liquid crystals are a much favored optoelectronic substance on account of easy tunability of their properties with pressure, temperature, electric fields, and magnetic fields. This suggests a marriage of convenience with PCs, whose most prominent feature is the photonic band gap (PBG). Indeed, in 1999 Bush and John proposed that, by infilling a PC with a liquid crystal, an applied electric field would tune the PBG [102, 103]. Enthusiastic response led to rapid growth, reported in a recent review [104] and a specialized conference [105]. We proceed to describe some of the advances in liquid crystal-infilled, two-dimensional (2D) and three-dimensional (3D) PCs and a few applications of related structures. Most of this work was done on *nematic* liquid crystals (NLCs) which, on account of their rodlike molecules, have the simplest macroscopic properties.

The first tuning experiment was performed by Leonard [32], who infiltrated the NLC *E7* into the air pores of a 2D macroporous silicon PC. Strong, polarization-sensitive tuning of the band edges was attained as the sample was heated from the nematic phase, beyond the phase transition, to the isotropic phase. The results were interpreted in terms of the escaped radial (ER) configuration of NLC directors. While this work concerned continuous tuning, in ref. [106] the shifts in band structure and transmission were contrasted in the nematic and isotropic phases, assuming that the NLC *5CB* occupies the space between a 2D lattice of metallic *plasma* bars. The axial (AX) NLC configuration was arbitrarily assumed. Takeda and Yoshino [38, 107] came to the theoretical conclusion that a NLC-infilled 2D PC does not support independent E- and H-modes - as is the rule for isotropic ingredient materials. As a result, an incident wave polarized perpendicular to the cylinders gives rise to transmission with parallel polarization, as well as perpendicular one. It is assumed that the NLC directors have a fixed direction within all the cylinders and that this direction can be altered by the application of an electric field [38, 107]. Much the same is assumed in ref. [108] for the nematic 5CB occupying the space between Si bars. Another promising line of research is tuning of the refraction, including the *superprism* effect [109, 110, 111]. We also note that it has become possible to fabricate PCs made up of parallel filaments of a liquid crystal-polymer composite in air (lattice constant only about 0.2 μm!) [112].

A promising application of these ideas is the recent advent of NLC-infilled PC *fibers*. Proposed by Larsen et al. [113, 114], the authors demonstrated thermo-optic tuning and switching that utilized shifts of the photonic bands with temperature. Electrical tuning of similar fibers was accomplished by Du et al. [115], who observed variations in the light output of the fiber with transversely applied voltage, as well as the switching function. All-optical modulation [116] and continuous electrically controlled tunability [117] were also demonstrated.

As for 3D PCs infilled with NLCs, ever since the original idea of Busch and John [102, 103], there was a strong preference for synthetic opal structures. The first such experimental work was done by Yoshino et al. [28, 118], who showed that the optical stop band in the transmission spectrum shifts drastically by the infiltration of liquid crystals. Subsequent work, also on silica opal, demonstrated tuning of the optical response by an external electric field [119, 120]. Mertens et al. [121], studied both normal and inverted colloidal crystals infilled with the *E7* NLC. They found that the Bragg reflection peak in the [122] direction can be temperature-tuned. Interestingly, in ref. [122] it was shown that, in specially prepared synthetic opals, the nematic directors can self-align in a unique, well defined direction. Also, Escuti et al. [123], reported on the fabrication and electro-optic measurements of fcc lattices in holographic polymer-dispersed NLCs.

Several NLC-infilled defect structures were also tuned. In ref. [124] it was demonstrated that a NLC defect layer within a 1D PC gives rise to a transmission peak whose spectral position could be tuned by an external voltage. Schuller et al. [125], fabricated a planar microcavity in a 2D PC of air holes, thus producing a linear waveguide. In an experiment similar to that of Leonard et al. [32], with the *E7* NLC having been injected into the holes, the transmission peak was tuned by sweeping the temperature from 20 °C up to 72 °C (beyond the nematic-isotropic phase transition at 60 °C). Takeda and Yoshino [126] studied theoretically a NLC polymer film forming a defect layer within a 2D PC. It was found that the transmission peaks depend on the direction of the NLC director - assumed to be constant, as in ref. [38, 107]. The same authors also designed a Y-shaped wave guide in a 2D PC, with the three arms of the Y having different radii [127]. The path taken by the light could then be controlled by an applied field - although not assumed explicitly.

It is noteworthy that an electrically tunable laser has been devised; it is based on infiltrating a NLC into the void cylinders of a 2D PC with a defect cavity (produced by replacing one of the cylinders by a narrower one) [128]. Application of a voltage realigns the NLC molecules, changing the effective index and laser cavity's optical length, thus blue-shifting the lasing wavelength ($\simeq 1.6\mu m$).

After this survey of advances in tuning of PCs by means of infiltration of NLCs, it is evident that deeper understanding and future applications much depend on in-depth studies of the configuration of the NLC within a PC of interest. That is, what is the precise direction of the NLC director $\hat{\mathbf{n}}(\mathbf{r})$ at every point within the infiltrated voids? How does this direction depend on an applied electric field or on the temperature? Is it possible to have a change of the *type* of configuration, that is, a phase transition even below the usual nematic phase-isotropic phase transition point? The only way to answer these questions is to minimize the free energy of the system. In a 3D PC the infilled voids have very complicated geometrical forms; for example, a general solution for the much-favored synthetic opals is a formidable problem [96, 109, 111]. On the other hand, 2D PCs - given their simple, cylindrical voids - are a manageable task.

In the next section will be established the basic formulas for the free energy of an isolated NLC cylinder subject to an external, axial DC electric field. In doing so will take fully into account the bulk and surface interactions of the NLC molecules. The free energy is minimized in sec. 4.3, considering three possible configurations: ER, the planar radial (PR), and the AX. The direction of the director $\hat{\mathbf{n}}(\mathbf{r})$ is calculated as function of the radial distance in the cylinder and of the magnitude of the applied field. For sufficiently large values of this field a phase transition occurs, as shown in sec. 4.4, from the ER to the AX configuration. In sec. 4.5 the dielectric tensor for the NLC cylinder - which is both inhomogeneous and anisotropic - is used to derive the eigenvalue equation for the magnetic field in the NLC-infilled PC. This equation separates into the usual, independent E- and H-polarization modes only for applied electric fields above the critical value - when the NLC configuration is axial. Nevertheless, it is also show that such two independent modes follow from an approximate treatment (sec. 4.6) that averages the dielectric tensor over the cross-section of a cylinder. Rather surprisingly, graphical comparison of the PBSs obtained from the approximate and exact theories yield a very good fit (sec. 4.7). From this fact it is possible to conclude that, while for sub-critical electric fields, strictly speaking, there is no separation into E- and H-modes, such a classification is a very reasonable approximation - at least for the materials considered in this work (*5CB* NLC in silicon oxide (silica) PC). Finally, the conclusions are given in sec. 4.8; substantial tuning of the photonic bands and band gaps, as well as polarization effects, can be accomplished by means of the external electric field.

4.2 Model and basic equations for nematic liquid crystal cylinder

In this section, instead of considering the Photonic Crystal (PC) as a whole, will be considered a single, circular and infinitely long, cylinder of LC that is contained within an isotropic dielectric material. In what follows are commented the assumptions and approximations involved in the calculation.

It is assume homeotropic anchoring of the nematic liquid crystal (NLC) molecules at the cylinder walls. This means that the easy direction for the molecular orientation is the direction perpendicular to the wall at every point. According to Burylov [130], “in essentially every experiment to date the anchoring is of homeotropic type". This, however, does not mean that the directors are perpendicular to the walls; the actual inclination also depends on elastic forces due to neighboring molecules, on external fields, and on the strength of anchoring. This leaves three possible structures [129], namely the PP, the PR, and the ER. In the first two structures all the directors of the

LC lie in the plane perpendicular to the cylinder. In case of the ER structure the directors form a certain angle with the normal to the wall; the angle gradually increases as the cylinder axis is approached and, on the axis itself, the directors are parallel to it.

The macroscopic description of the Van der Waals forces between the NLC molecules is given in terms of the following formula [129] for the elastic contribution to the free-energy density:

$$\begin{aligned} F_{el} = \tfrac{1}{2}\int_V dV[K_{11}(\nabla\cdot\hat{\mathbf{n}})^2 + K_{22}(\hat{\mathbf{n}}\cdot\nabla\times\hat{\mathbf{n}})^2 + \\ + K_{33}(\hat{\mathbf{n}}\times\nabla\times\hat{\mathbf{n}})^2 - K_{24}\nabla\cdot[\hat{\mathbf{n}}\nabla\cdot\hat{\mathbf{n}} + \hat{\mathbf{n}}\times\nabla\times\hat{\mathbf{n}}]] \\ + \tfrac{1}{2}\int W_0\cos^2\theta(R)dS \end{aligned} \tag{4.1}$$

Here the unit vector $\hat{\mathbf{n}}$ is the director, the elastic moduli K_{11}, K_{22}, and K_{33} describe, respectively, transverse bending (splay), torsion (twist), and longitudinal bending (bend) deformations. K_{24} is called the surface elastic constant because it is the coefficient of a divergence term which can be transformed to a surface integral by using Green's theorem. The last term provides the interaction between the NLC and the confining surface. There $\theta(R)$ is the angle between $\hat{\mathbf{n}}$ and the axial direction evaluated at the surface of the cylinder, and W_0 denotes the strength of interaction, in units of energy per area, between a nematic molecule and the surface.

It is assumed that the wave field **E** is much weaker than the applied field $\mathbf{E}_0 : |\mathbf{E}| \ll |\mathbf{E}_0|$, so that the dielectric tensor of the LC will not depend on the wave field. Thus our study of the optical response of the LC-infilled PC is linear. Additionally, it is assumed that the external field $\mathbf{E}_0$ is larger than the critical (Freedericksz) field, below of which no reorientation of the nematic LC molecules occurs. Finally, it is neglected absorption in both the LC and the dielectric host.

The free energy of the LC cylinder has, in addition to the above elastic part, also an electromagnetic part due to the applied electrostatic field. As we have already discussed, the first contribution is given by eq. (4.1). The electromagnetic free energy density, taking $\mathbf{E}_0$ along *z*-axis is, in MKS units

$$\begin{aligned} F_{el} &= -\tfrac{1}{2}\int_V [\mathbf{D}\cdot(\mathbf{E}_0+\mathbf{E})+\mathbf{B}\cdot\mathbf{H}]dV \\ &\simeq -\tfrac{1}{2}\int_V \varepsilon_{zz}(r)E_0^2 dV \end{aligned} \tag{4.2}$$

where we have used the fact that $\left|\mathbf{E}\right| \ll \left|\mathbf{E}_0\right|$.

Now we must express the element of the dielectric tensor $\varepsilon_{zz}(r)$ in terms of the ordinary and extraordinary dielectric constants of the NLC, ($\varepsilon_o = n_o^2$) and ($\varepsilon_e = n_e^2$), respectively. At a point where the director forms an angle with the *z*-axis, the dielectric tensor in the proper coordinate system of the NLC has the uniaxial form. This must be transformed into the "laboratory" coordinate system *x, y, z*, resulting in the following expression for the dielectric tensor elements:

$$\varepsilon_{ij} = \varepsilon_o\delta_{ij} + \varepsilon_a n_i n_j \tag{4.3}$$

where $\varepsilon_a = \varepsilon_e - \varepsilon_o$ is the "dielectric anisotropy" and the components of the director are

$$n_x = \sin\theta(r)\cos\phi \tag{4.4}$$

$$n_y = \sin\theta(r)\sin\phi \tag{4.5}$$

$$n_z = \cos\theta(r) \tag{4.6}$$

The angle ϕ is measured with respect to the (arbitrarily oriented) *x*-axis. For infinite circular cylinders the symmetry implies that $\theta = [\hat{\mathbf{n}} \cdot \hat{\mathbf{z}}]$ only depends on the radial distance *r*. Since $\hat{\mathbf{n}}$ is a position dependent vector, eqs. (4.3)-(4.6) show explicitly that we have inhomogenety, as well as anisotropy. Using the eqs. (4.1) and (4.2), the total free-energy becomes

$$\begin{aligned} F = F_{el} + F_{em} &= \tfrac{1}{2}\int_V dV[K_{11}(\nabla \cdot \hat{\mathbf{n}})^2 + K_{22}(\hat{\mathbf{n}} \cdot \nabla \times \hat{\mathbf{n}})^2 + \\ &+ K_{33}(\hat{\mathbf{n}} \times \nabla \times \hat{\mathbf{n}})^2 - K_{24}\nabla \cdot [\hat{\mathbf{n}}\nabla \cdot \hat{\mathbf{n}} + \hat{\mathbf{n}} \times \nabla \times \hat{\mathbf{n}}]] \\ &+ \tfrac{1}{2}\int W_0 \cos^2\theta(R)dS - \tfrac{1}{2}E_0^2\int_V \varepsilon_{zz}(r)dV \end{aligned} \tag{4.7}$$

This section is concluded with an important note: While eqs. (4.3)-(4.6) are valid for any frequency, the static limiting values $\varepsilon_o(\omega \to 0)$ and $\varepsilon_a(\omega \to 0)$ must be used for the tuning with the essentially DC applied field E_0, while the high frequency (optical) values $\varepsilon_o(\omega \to \infty)$ and $\varepsilon_a(\omega \to \infty)$ apply to the infrared EM fields in the PC. Hence, the static (optical) values are used in sections 4.2-4.4 (4.5-4.7).

4.3 Nematic Configurations

The free energy of the LC is obtained by integrating eq. (4.7) over the cylindrical volume. Then, expressing $\nabla \cdot \hat{\mathbf{n}}$ and $\nabla \times \hat{\mathbf{n}}$ in cylindrical coordinates it is obtained the free energy per unit length. The calculation is done for the ER configuration which covers the PR and the AX configurations as special cases. Taking *L* as the cylinder length and normalizing the radial distance *r* with the cylinder radius $R(r \,/\, R = x)$ it is obtained

$$F / L \equiv F_{ER} = \int_0^1 dx\, f_B(\theta, d\theta / dx) + f_s[\theta(1)] \tag{4.8}$$

where the bulk f_B and surface f_s expressions are defined as

$$\begin{aligned} f_B(\theta, d\theta / dx) = \pi K_{11} x \Bigg[\left(\frac{d\theta}{dx} \right)^2 (\cos^2\theta + \eta \sin^2\theta + \frac{\sin^2\theta}{x^2} \\ -q(\cos^2\theta + \varepsilon_o / \varepsilon_a) \Bigg] \end{aligned} \tag{4.9}$$

$$f_s(\theta) = \pi K_{11} \sigma \cos^2\theta(1) - \pi(K_{24} + K_{11}). \tag{4.10}$$

Here

$$\eta \equiv K_{33} / K_{11} \tag{4.11}$$

$$\sigma \equiv R W_0 / K_{11} + K_{24} / K_{11} - 1 \tag{4.12}$$

and *q* is the important parameter defined as

$$q \equiv \varepsilon_a E_0^2 R^2 / K_{11} \tag{4.13}$$

The *q*-parameter represents the ratio of the electric and elastic energies; for $q \ll 1$ the influence of the applied field is weak, while, for $q \gg 1$ the field essentially overcomes the Van der Waals forces between the molecules. Note that the effectiveness of the field E_0 is greatly augmented for large radii *R* of the tubes.

The dependence of the director inclination $\theta(r)$ on the radial distance, for the ER configuration (our general case), is obtained by minimization of the free energy F_{ER}.

With this purpose in mind, in eq. (4.8) we consider θ and $d\theta / dx$ in $f_B(\theta, d\theta / dx)$ as two independent variables. Then the variation of F_{ER} is

$$\delta F_{ER} = \int_0^1 dx \left[\frac{\partial f_B(\theta, d\theta / dx)}{\partial \theta} \delta\theta + \frac{\partial f_B(\theta, d\theta / dx)}{\partial (d\theta / dx)} \delta \left(\frac{d\theta}{dx} \right) \right] + \frac{df_s[\theta(1)]}{d\theta(1)} \delta\theta(1) \quad (4.14)$$

Notice that even though f_s in eq. (4.10) is not a function of x, it is nevertheless a function of $\theta(1)$. Then, as usual in variational calculus [130], we exchange the order of the variation and the derivative: $\delta\left(\frac{d\theta}{dx}\right) = \frac{d}{dx}\delta\theta$ and use the identity

$$\frac{d}{dx}\left\{ \frac{\partial f_B(\theta, d\theta / dx)}{\partial (d\theta / dx)} \delta\theta \right\} = \frac{d}{dx}\left\{ \frac{\partial f_B(\theta, d\theta / dx)}{\partial (d\theta / dx)} \right\} \delta\theta + \frac{\partial f_B(\theta, d\theta / dx)}{\partial (d\theta / dx)} \frac{d(\partial\theta)}{dx} \quad (4.15)$$

to rewrite Eq. (4.14) as

$$\begin{aligned} \delta F_{ER} = & \int_0^1 dx \left[\frac{\partial f_B(\theta, d\theta / dx)}{\partial \theta} - \frac{d}{dx}\left\{ \frac{\partial f_B(\theta, d\theta / dx)}{\partial (d\theta / dx)} \right\} \right] \delta\theta \\ & + \left[\frac{df_s}{d\theta} + \frac{\partial f_B(\theta, d\theta / dx)}{\partial (d\theta / dx)} \right]_{x=1} \delta\theta(1) \end{aligned} \quad (4.16)$$

Here we have used the fact that $\theta(0) = 0$ in the ER configuration, implying that $\delta[\theta(0)] = 0$. To find the extrema we set the condition $\delta F_{ER} = 0$ which can be fulfilled by satisfying simultaneously the conditions:

$$\frac{\partial f_B(\theta, d\theta / dx)}{\partial \theta} - \frac{d}{dx}\left\{ \frac{\partial f_B(\theta, d\theta / dx)}{\partial (d\theta / dx)} \right\} = 0 \quad (4.17)$$

$$\left[\frac{df_s}{d\theta}+\frac{\partial f_B(\theta, d\theta / dx)}{\partial(d\theta / dx)}\right]_{x=1}=0 \tag{4.18}$$

Eq. (4.17) describes the nematic's bulk and is the well known Euler-Lagrange equation which assumes the explicit form

$$\begin{aligned}\frac{d^2\theta}{dx^2}x^2\left(\cos^2\theta+\eta\sin^2\theta\right)+\left(\frac{d\theta}{dx}\right)^2\frac{x^2}{2}(n-1)\sin 2\theta \\ +x\frac{d\theta}{dx}\left(\cos^2\theta+\eta\sin^2\theta\right)-\tfrac{1}{2}\sin 2\theta-q\frac{x^2}{2}\sin 2\theta=0\end{aligned} \tag{4.19}$$

Eq. (4.18) leads to the “arbitrary anchoring” boundary condition at the surface

$$\left.\frac{d\theta}{dx}\right|_{x=1}=\left.\frac{\sigma\sin\theta\cos\theta}{\cos^2\theta+\eta\sin^2\theta}\right|_{x=1} \tag{4.20}$$

In the above procedure we have just performed a free-end-point variation [130] for which θ is subjected to a finite force $df_s / d\theta$ at the cylinder border. To check that Eq. (4.20) is indeed consistent with the hard-anchoring boundary condition $\theta(1)=\pi / 2$, valid for a very large surface force, let us divide Eq. (4.20) by σ and take the limit when $W_0 \to \infty$. Then according to eq. (4.12) $\sigma \to \infty$ and we obtain that

$$\sin\theta(1)\cos\theta(1)=0\,. \tag{4.21}$$

This equation has the solutions $\theta(1)=0$ and $\theta(1)=\pi / 2$. The former condition is associated with the AX configuration that will be discuss below, and the second one is what we were looking for.

Notice that Eq. (4.19) has two simple exact solutions, namely, $\theta(x) = \pi/2$ and $\theta = 0$. The first possibility corresponds to the PP or PR configurations, the second one to the AX structure. A third solution is the ER configuration which depends on the radius and fields through the parameter *q*, Eq. (4.13), and should be obtained by solving Eq. (4.19) subject to the condition Eq. (4.20). To discern which of these configurations the nematic actually adopts, it is necessary to calculate their corresponding total energies from eqs. (4.8)–(4.10) to choose the one with smallest value. It will be discussed below.

Numerical solutions of Eq. (4.19) subjected to the conditions given by Eq. (4.20) and $\theta(0) = 0$ were calculated by using the shooting method [131] for different values of *q* and are shown in Figs. 1-4. We performed the calculations for the NLC *5CB* at $T_{IN} - T = 10°\mathrm{C}$ where $T_{IN} = 35°\mathrm{C}$ is the clearing temperature at which *5CB* suffers the transition from nematic to isotropic phase. The other parameters [132] are $\eta = 1.316$, $K_{11} = 1.2 \times 10^{-11} N$, $W_0 / K_{11} = 40 \mu m^{-1}$, $K_{24} / K_{11} = 1$, $\varepsilon_o = 7$ and $\varepsilon_a = 1.5$. In Figs.4.1-4.4 the angle θ, between the nematic director and the cylinder axis is plotted versus the radial distance. In all these figures the various curves are characterized by the field parameter *q*, defined in Eq. (4.13). The uppermost curve corresponds to $q = 0$ and describes the ER configuration in the absence of an applied field. The value of *q* increases from top to bottom, the last curve -a straight line coinciding with the *q*-axis - corresponding to the critical value of *q*, at which the phase transition ER →AR occurs. The specific values of *q* for each curve are given in the figure captions.

These figures clearly show that, for any value of the field parameter *q*, the directors are constrained to the axial direction on the cylinder axis and to some angle $0 < \theta < \pi/2$ at the wall. Notice how the value of θ at the cylinder wall $x = 1$ diminishes with increasing field, which implies that for general anchoring the field has stronger effect on the configuration than it has in the strong anchoring limit. Moreover, for a given finite value of $\sigma > 1$, we can find numerically a value of q for which $\theta(x) = 0$ at every point; that is, a phase transition occurs from the ER to the AX configuration. This is indicated by the largest value of q in figures 4.1–4.4, that corresponds to $\theta(x) = 0$. In the next section will be explored the phase transition in detail.

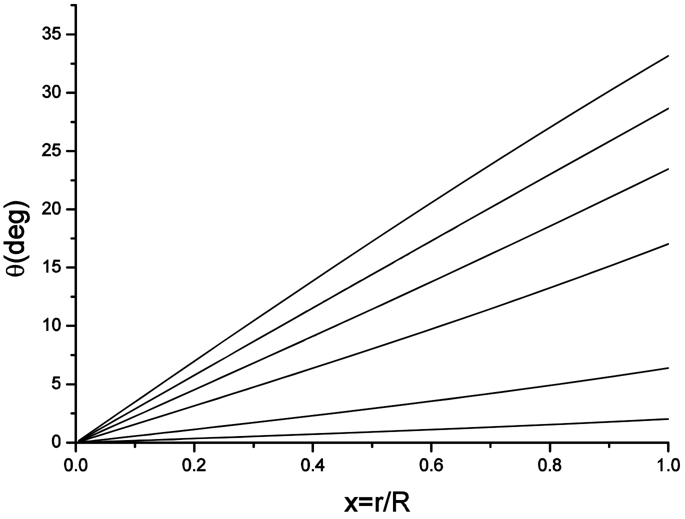

Fig. 4.1. Inclination of the NLC director θ versus the dimensionless radial distance $x = r / R$ for the nematic 5CB with $\eta = 1.316$ and $\sigma = 1.25$ ($R = 31.25\text{nm}$). The field parameter takes the values (from above to below) q = 0, 0.25, 0.5, 0.75, 1, 1.045, 1.049. For the last value of q, $\theta(x) = 0$.

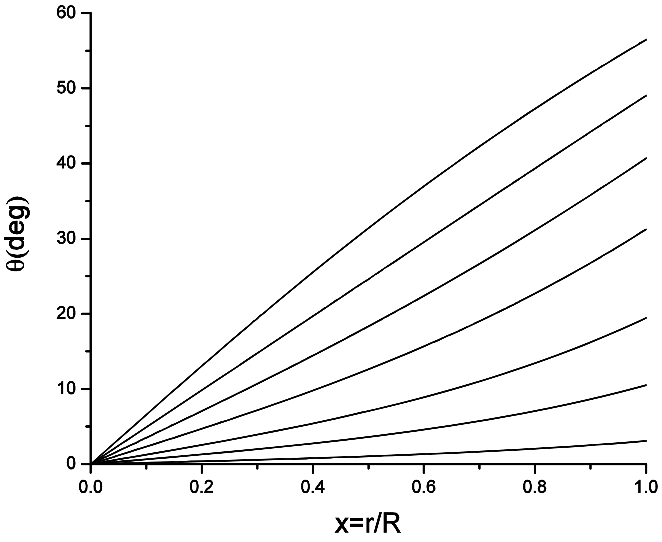

Fig. 4.2. As in Fig. 4.1 for $\sigma = 2$ ($R = 50\text{nm}$) and q = 0, 1, 2, 3, 4, 4.5, 4.7, 4.75.

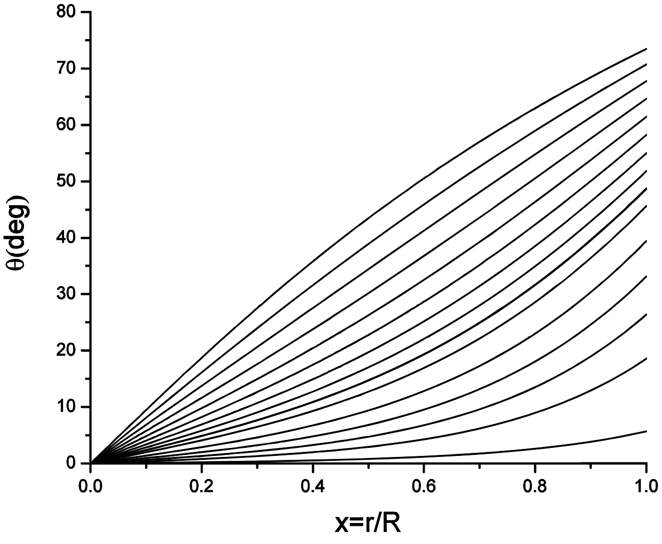

Fig. 4.3. As in Fig. 4.1 for $\sigma = 4$ ($R = 0.1\mu m$) and q = 0, 1, 2, 3, 4, 5, 6, 7, 8, 9, 11, 13, 15, 17, 19, 19.2.

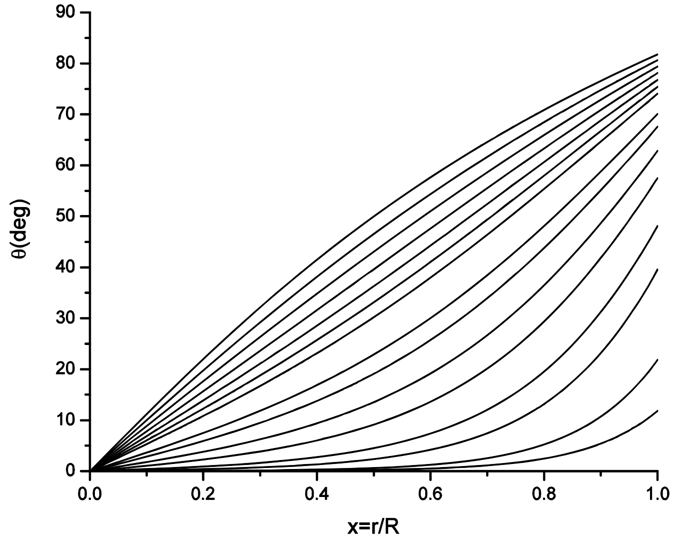

Fig. 4.4. As in Fig. 4.1 for $\sigma = 8$ ($R = 0.2\mu m$) and q = 0, 1, 2, 3, 4, 5, 6, 9, 11, 15, 20, 30, 40, 60, 70, 71.39.

4.4 Phase transition from escaped radial to the axial configuration

It is possible to obtain the free energy density for the PR configuration from Eq. (4.8) by setting $\theta = \pi/2$; this leads to

$$F_{PR} = \pi K_{11}\left[\ln(R/\rho) + 1 - K_{24}/K_{11} - q\,\varepsilon_0/2\varepsilon_a\right] \tag{4.22}$$

where ρ is the radius of the dislination core which should be of the order of the molecular size. The energy for the AX configuration is obtained by setting $\theta = 0$ and is given by

$$F_{AX} = \pi K_{11}\left[-(\varepsilon_a + \varepsilon_0)\,q/2\varepsilon_a + R\,W_0/K_{11}\right] \tag{4.23}$$

The PR configuration becomes energetically more favorable than the ER if $F_{PR} < F_{ER}$. Thus the boundary between both configurations in the parameter space is described by the equation

$$\begin{aligned}&\ln(R/\rho)+1-K_{24}/K_{11}-E_0^2R^2/2K_{11}\varepsilon_o\\&\quad-F_{ER}(\eta,RW_0/K_{11}+K_{24}/K_{11}-1,\varepsilon_aE_0^2R^2/K_{11})/\pi K_{11}=0\end{aligned} \tag{4.24}$$

Similarly, the AX configuration becomes energetically more favorable than the ER if $F_{AX} < F_{ER}$ that is, the boundary between these configurations is defined by

$$\begin{aligned}&-(\varepsilon_a+\varepsilon_o)E_0^2R^2/2K_{11}+RW_0/K_{11}\\&\quad-F_{ER}(\eta,RW_0/K_{11}+K_{24}/K_{11}-1,\varepsilon_aE_0^2R^2/K_{11})/\pi K_{11}=0\end{aligned} \tag{4.25}$$

Using the numerical solutions for $\theta(x)$, shown for several of values of σ in Figs. 4.1–4.4, and those of $d\theta(x)/dx$, we calculate numerically $F_{ER}(\eta,\sigma,q)$ as given by equation (4.8) and insert it in the last two equations. Are found no realistic solutions for Eq. (4.24). This is essentially due to the fact that the parameter ρ has to be taken of the order of the molecular size $\rho \simeq 2nm$ so that $\ln\rho$ is very large unless $R \leq 10nm$. In contrast, it is found a solution for Eq. (4.25) that is plotted in Fig. 4.5 for an AC electric field of 1 Khz. In the context of the photonic crystal, this can be considered a DC field.

Note that, for this particular NLC, $K_{24} = K_{11}$ and thus $\sigma = (W_0 / K_{11})R$. The variation of the parameter σ in Figs. 4.1–4.4 then corresponds simply to variation of the cylinder radius *R*.

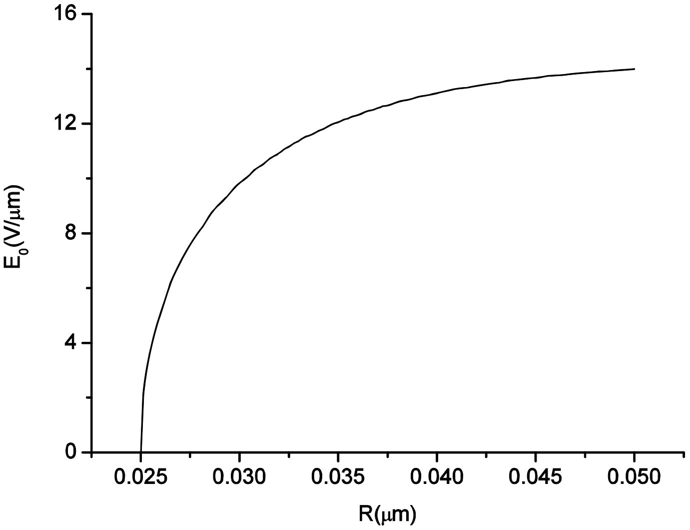

Fig. 4.5 E_0 as function of R. Eq. 4.32 provides the asymptotic value for E_0.

From Fig. 4.5 it is possible to see that for large values of R, the necessary field E_0 to cause the phase transition seems to tend to a constant value. It can be shown analytically that the solution of Eq. (4.19) has this behavior, by calculating its asymptotic form for large values of q.

As is well known, the effect of the external field on the nematic is usually opposed to that of elastic forces, particularly at frontiers of the nematic where the molecules anchor to the walls. This competition is stronger for intense fields since in the regions which lie “far” from the border (bulk), the nematic director is practically aligned with the field, whereas within a layer of nematic in contact with the solid walls, the orientation of $\hat{\mathbf{n}}$ displays strong spatial gradients, so as to satisfy the boundary conditions. These two regions with different behaviors can be described simultaneously by using the boundary layer technique [133] for which the solution in the bulk is denoted by $\theta_b(x)$ and the solution within the layer is represented by $\theta_1(x)$.

The solutions for both regions are coupled or matched asymptotically to give rise to a continuous solution $\theta_{adj}(x)$, valid for the entire domain and is given by

$$\theta_{adj}(x) = \theta_b(x) + \theta_1(x) - \theta_{match}(x) \tag{4.26}$$

Here $\theta_{match}(x)$ must be determined so that the solution in the boundary layer $\theta_1(x)$ and the solution in the bulk $\theta_b(x)$ are joined asymptotically. In other words, $\theta_{match}(x)$ is defined as the solution within the region where $\theta_1(x)$ and $\theta_b(x)$ overlap each other, that amounts mathematically to write [133]

$$\theta_{match}(x) = \lim_{h\to\infty} \theta_1(x) = \lim_{x\to\gamma} \theta_b(x) \tag{4.27}$$

where γ represents the region in which θ_b cannot satisfy at least one of the boundary conditions (in our case at the border of the cylinder) and *h* is related with the thickness of the boundary layer.

To apply this formalism, it must be note first, that, for large *q*, Eq. (4.19) reduces to $qx^2 \sin 2\theta = 0$ which means that the AX solution $\theta_b(x) = 0$ (bulk), which does not satisfy the boundary condition given by Eq. (4.20)!, is reached apparently for the whole domain $0 \le x \le 1$. To get around this problem, $\theta_b(x)$ should be no longer valid for a narrow region near $x = 1$. Thus, there must exist a region (not a point) near the boundary $x = 1$ (that we call the boundary layer) where the solution varies on a rapid spatial scale so as to both satisfy the boundary condition given by Eq. (4.20) and tend to the bulk solution θ_b outside of this thin layer. To find this boundary layer solution $\theta_1(x)$ we need to express Eq. (4.19) in terms of a rapid scale variable $\ln x' \equiv \sqrt{q}\ln x$ or $x' \equiv x^{\sqrt{q}}$, which is selected in such a way that the highest order derivative of θ is to be proportional to the last term, (field term) of this equation. This derivative term will allow θ to vary adequately near the boundary. In this way, even for large values of *q* we keep the highest derivative by using this fast variable, which allows to write $x\, d\theta\big/ dx = \sqrt{q}x' d\theta\big/ dx'$, leading to

$$q\sqrt{\cos^2\theta + \eta \sin^2\theta}x' \frac{d}{dx'}\left[x' \frac{d\theta}{dx'}\sqrt{\cos^2\theta + \eta\sin^2\theta}\right] \\ -\frac{1}{2}\sin 2\theta - \frac{q{x'}^{2/\sqrt{q}}}{2}\sin 2\theta = 0 \tag{4.28}$$

Taking the limit of large *q* this equation turns out to be Eq. (4.19) for a vanishing *q* value. Similarly, using the fact that $d\theta\big/ dx\big|_{x=1} = \sqrt{q}\, d\theta\big/ dx'\big|_{x'=1}$ Eq. (4.20) remains the same after replacing σ by $\sigma' = \sigma\big/\sqrt{q}$. Thus, the boundary layer solution θ_1 for large *q* can be obtained by replacing *x* and σ by $x^{\sqrt{q}}$ and $\sigma' = \sigma\big/\sqrt{q}$, respectively, in the solution $\theta = \theta(x)$ in the absence of external fields ($q = 0$). This solution of Eq. (4.19), without the last term has been found by Crawford et al. [132] in the inverse form $x = x(\theta)$, as follows:

$$x = \sqrt{\frac{\sigma+1}{\sigma-1}\frac{\Delta-1}{\Delta+1}} Exp\left[\sqrt{\eta-1}\arctan\left(\frac{\sqrt{\eta-1}(\Delta-\sigma)}{\Delta\sigma+\eta-1}\right)\right] \quad \text{for} \quad q = 0 \tag{4.29}$$

This is the solution of Eq. (4.19) when there is no applied field ($q = 0$). Here $\Delta = \sqrt{1+\eta\tan^2\theta}$.

As it was showed above, for $q \to \infty$ the bulk solution is $\theta_b = 0$ and it can be proved consistently that $\lim_{\sqrt{q}\to\infty} \theta_1 = \theta(x^{\sqrt{q}}, \sigma/\sqrt{q}, \eta) \to 0$ so that θ_{match} vanishes and as a consequence θ_{adj} from Eq. (4.26) reduces to θ_1 which yields

$$\theta_{adj} = \theta(x^{\sqrt{q}}, \sigma/\sqrt{q}, \eta) \tag{4.30}$$

At this point, it is convenient to recall that the ER solution $\theta \neq 0$, given by Eq. (4.29), valid in the absence of a field, is only possible for $\sigma > 1$. Otherwise, the anchoring at the cylinder wall is no longer possible [129] and the system acquires the AX solution ($\theta = 0$). In fact, if we take the limit $\sigma \to 1$ in Eq. (4.29), *x* will remain finite only if $\Delta \to 1$, implying $\theta \to 0$. According to Eq. (4.30), rescaling of σ to the variable $\sigma' = \sigma / \sqrt{q}$ implies that the threshold value for the realization the ER-AX phase transition is translated by the influence of the field from $\sigma = 1$ to $\sigma/\sqrt{q} = 1$. Hence, using the Eqs. (4.12) and (4.13), we find the expression for the threshold or critical field $E_0 = E_c$:

$$E_c = \frac{W_0/K_{11} + K_{24}/RK_{11} - 1/r}{\sqrt{\varepsilon_a/K_{11}}} \tag{4.31}$$

that for large *R* goes to the constant value

$$E_c = \frac{W_0}{\sqrt{\varepsilon_a K_{11}}} \tag{4.32}$$

Using numerical values for the *5CB* nematic we get $E_c = 13.45\,V/\mu m$. Actually, because in the particular case of the NLC *5CB*, $K_{24} = K_{11}$, Eq. (4.13) is independent of *R*. Because, according to Eq. (4.13) $\sqrt{q} \propto R$, our asymptotic calculation should not work well for small values of *R* as is apparent from Fig. 4.5.

Also, Eq. (4.19) admits the AX solution for all *q*:

$$\theta_q(x) = 0 \tag{4.33}$$

However, as we have noted in the discussion of Eq. (4.25), the AX configuration is not favorable energetically for subcritical fields, while for a field larger than the value given by Eq. (4.31), it is the only solution.

Once $\theta(x)$ is calculated numerically, the Eq. (4.3) completely determine the dielectric tensor at every point of the LC cylinders and for all values of the field. Now one can proceed to the calculation of the PB structure, with allowance for the inhomogeneity and anisotropy of the LC cylinders, as done by Hornreich et al. [134] for cholesteric blue phases.

4.5 Photonic crystal composed of nematic liquid crystal cylinders

Sections 4.2–4.4 were devoted to the dielectric response of a single NLC cylinder subject to an axial DC electric field $E_0\hat{\mathbf{z}}$, neglecting the contribution of the AC wave field in our linear approximation. The conditions at the cylinder surface were specified in terms of the parameters W_θ and K_{24}, encapsulated in the important quantity σ, Eq. (4.12). We expect σ to be practically independent of the thickness of the cylinder wall, and this thickness has not been taken into account explicitly.

Summarizing our result up this point, the NLC cylinder is characterized by the dielectric tensor ε_{ij}, Eq. (4.3),

$$\overleftrightarrow{\boldsymbol{\varepsilon}} = \begin{pmatrix} \varepsilon_o + \varepsilon_a \sin^2\theta \cos^2\varphi & \varepsilon_a \sin^2\theta \sin\varphi \cos\varphi & \varepsilon_a \sin\theta \cos\theta \cos\varphi \\ \varepsilon_a \sin^2\theta \sin\varphi \cos\varphi & \varepsilon_o + \varepsilon_a \sin^2\theta \sin^2\varphi & \varepsilon_a \sin\theta \cos\theta \sin\varphi \\ \varepsilon_a \sin\theta \cos\theta \cos\varphi & \varepsilon_a \sin\theta \cos\theta \sin\varphi & \varepsilon_o + \varepsilon_a \cos^2\theta \end{pmatrix} \tag{4.34}$$

in the laboratory frame of reference. Here $\theta(r) = angle\,(\hat{\mathbf{n}}, \hat{\mathbf{z}})$ is the angle formed by the director $\hat{\mathbf{n}}$ with respect to the cylinder axis and φ is the angle between the projection of $\hat{\mathbf{n}}$ onto the *xy* plane and an arbitrarily oriented *x*-axis. The angle $\theta(r)$ depends on the radial distance *r*, is however independent of *z* for our infinitely long cylinders. This angle $\theta(r)$ is found from the solution of the differential Eq. (4.19) subject to the boundary condition Eq. (4.20). Examples of the solution, for four values of the parameter σ (corresponding to progressively increasing cylinder radii *R*) are shown in Figs. 4.1-4.4. For applied fields E_0 that are greater than the critical field E_c, as given by Eq. (4.25) or (4.31) and Fig. 4.5, all the directors assume the axial direction $(\hat{\mathbf{n}} = \hat{\mathbf{z}})$, that is, θ(r) = 0 for all *r*. Then Eq. (4.34) reduce to

$$\overleftrightarrow{\boldsymbol{\varepsilon}}_{AX} = \begin{pmatrix} \varepsilon_o & 0 & 0 \\ 0 & \varepsilon_o & 0 \\ 0 & 0 & \varepsilon_e \end{pmatrix} \tag{4.35}$$

as it should, recalling that the *anisotropy* is defined as the difference between the extraordinary and ordinary dielectric constants, $\varepsilon_a = \varepsilon_e - \varepsilon_o$.

Now we turn to a PC of NLC cylinders. Here is assumed that the applied electric field $E_0\hat{\mathbf{z}}$ has the same value at every point **r** within the PC. Given this and the molecular origin of the director orientation, we can safely assume that the configuration θ(r) in any given cylinder is not affected by neighboring cylinders. That is, it have been taken Eq. (4.34) to represent the dielectric tensor within all the cylinders of the PC $(r \le R)$. The space between the cylinders is filled by a uniform and isotropic dielectric having the dielectric constant ε_b. In what follows will be needed the inverse dielectric tensor or dyadic $\overleftrightarrow{\boldsymbol{\eta}}(\mathbf{r})$ that satisfies the definition

$$\overleftrightarrow{\boldsymbol{\eta}}(\mathbf{r}) \cdot \overleftrightarrow{\boldsymbol{\varepsilon}}(\mathbf{r}) = \overleftrightarrow{\mathbf{I}} \quad \text{for all } \mathbf{r}, \tag{4.36}$$

$\overleftrightarrow{\mathbf{I}} = \hat{\mathbf{x}}\hat{\mathbf{x}} + \hat{\mathbf{y}}\hat{\mathbf{y}} + \hat{\mathbf{z}}\hat{\mathbf{z}}$ being the unit dyadic. By inverting the matrices (4.34) and (4.35) it is found that

$$\overleftrightarrow{\boldsymbol{\eta}}(\mathbf{r}) = \frac{\overleftrightarrow{\mathbf{I}}}{\varepsilon_0} - \frac{\varepsilon_a}{\varepsilon_o \varepsilon_e} \begin{pmatrix} \sin^2\theta\cos^2\varphi & \sin^2\theta\sin\varphi\cos\varphi & \sin\theta\cos\theta\cos\varphi \\ \sin^2\theta\sin\varphi\cos\varphi & \sin^2\theta\sin^2\varphi & \sin\theta\cos\theta\sin\varphi \\ \sin\theta\cos\theta\cos\varphi & \sin\theta\cos\theta\sin\varphi & \cos^2\theta \end{pmatrix}$$

$$\equiv \eta_a(r,\varphi), \quad \text{r within any cylinder} \tag{4.37}$$

$$\overleftrightarrow{\boldsymbol{\eta}}(\mathbf{r}) = \frac{1}{\varepsilon_b}\overleftrightarrow{\mathbf{I}}, \quad \text{r outside of cylinders}$$

Clearly, the problem at hand is anisotropic, as well as inhomogeneous.

Every element of $\overleftrightarrow{\boldsymbol{\eta}}(\mathbf{r})$ is periodic in the *xy* plane, permitting its expansion in a 2D Fourier series:

$$\overleftrightarrow{\boldsymbol{\eta}}(\mathbf{r}) = \sum_{\mathbf{G}} \overleftrightarrow{\boldsymbol{\eta}}(\mathbf{G}) e^{i\mathbf{G}\cdot\mathbf{r}} \tag{4.38}$$

where $\mathbf{G} = G_x\hat{\mathbf{x}} + G_y\hat{\mathbf{y}}$ are the 2D reciprocal lattice vectors. The Fourier coefficients $\overleftrightarrow{\boldsymbol{\eta}}(\mathbf{G})$ are obtained as

$$\overleftrightarrow{\boldsymbol{\eta}}(\mathbf{G}) = \frac{1}{A_c} \int_{A_c} d\mathbf{r}\ \overleftrightarrow{\boldsymbol{\eta}}(\mathbf{r})\, e^{-i\mathbf{G}\cdot\mathbf{r}} \tag{4.39}$$

A_c being the area of the unit cell. For $\mathbf{G} = 0$, this is just the average of $\overleftrightarrow{\boldsymbol{\eta}}(\mathbf{r})$ over the unit cell. When integrating over de angle φ, for $\mathbf{G} = 0$ the off-diagonal elements of $\overleftrightarrow{\boldsymbol{\eta}}(\mathbf{r})$ give vanishing contribution, while the diagonal elements lead to integrals over the radius of the form $\int_0^1 dx \sin^2 \theta(x)$. Because $\int_{A_c} d\mathbf{r} \exp(-i\,\mathbf{G}\cdot\mathbf{r}) \equiv 0$ for any $\mathbf{G} \neq 0$, in this case Eq. (4.39) takes the form

$$\overleftrightarrow{\boldsymbol{\eta}}(\mathbf{G}) = \frac{1}{A_c} \int_0^R r dr \int_0^{2\pi} d\varphi \left[\overleftrightarrow{\boldsymbol{\eta}}_a(r,\varphi) - \frac{1}{\varepsilon_b} \overleftrightarrow{\mathbf{I}} \right] e^{-ir(G_x \cos\varphi + G_y \sin\varphi)} \tag{4.40}$$

This dyadic is *not* diagonal, and its elements must be calculated numerically. Considering Eq. (4.37), $\overleftrightarrow{\boldsymbol{\eta}}(\mathbf{G})$ is symmetric, namely $\eta_{\alpha\beta}(\mathbf{G}) = \eta_{\beta\alpha}(\mathbf{G})$.

Now we turn to Maxwell's Equations for the PC. For harmonic waves of circular frequency ω, Faraday's Law is

$$\nabla \times \mathrm{E} = ik_0 \mathbf{B}(\mathbf{r}) \tag{4.41}$$

For our periodic medium both $\mathbf{E}(\mathbf{r})$ and $\mathbf{B}(\mathbf{r})$ must be Bloch waves,

$$\mathbf{E}(\mathbf{r}) = \sum_{\mathbf{G}} \mathbf{E}_{\mathbf{k}}(\mathbf{G}) e^{i(\mathbf{k}+\mathbf{G})\cdot\mathbf{r}} \tag{4.42}$$

$$\mathbf{B}(\mathbf{r}) = \sum_{\mathbf{G}} \mathbf{B}_{\mathbf{k}}(\mathbf{G}) e^{i(\mathbf{k}+\mathbf{G})\cdot\mathbf{r}} \tag{4.43}$$

Here **k** is the Bloch wave vector and $\mathbf{E}_\mathbf{k}(\mathbf{G})$ and $\mathbf{B}_\mathbf{k}(\mathbf{G})$ are the Fourier coefficients, respectively, of the amplitudes of **E**(**r**) and **B**(**r**). Substituting the Eqs. (4.42) and (4.43) in Eq. (4.41), it is possible to conclude that

$$(\mathbf{k}+\mathbf{G})\times\mathbf{E}_\mathbf{k}(\mathbf{G}) = k_0\mathbf{B}_\mathbf{k}(\mathbf{G}) \tag{4.44}$$

Therefore, for every partial plane wave in Eqs. (4.42) and (4.43), the magnetic induction amplitudes $\mathbf{B}_\mathbf{k}(\mathbf{G})$ are perpendicular to the electric field amplitudes $\mathbf{E}_\mathbf{k}(\mathbf{G})$ and to the wave vector $(\mathbf{k}+\mathbf{G})$. Hence, $\mathbf{B}_\mathbf{k}(\mathbf{G})$ is represented as having two independent components that are perpendicular to (**k** + **G**). It is convenient to choose one of these components to be parallel to the cylinders, the other component then lying in the plane of periodicity. Then

$$\mathbf{B}_\mathbf{k}(\mathbf{G}) = \sum_{\lambda=1}^{2} \mathrm{B}_{\mathbf{k}\lambda}(\mathbf{G})\,\hat{\zeta}_{\mathbf{k}\lambda}(\mathbf{G}) \tag{4.45}$$

$$\hat{\zeta}_{\mathbf{k}2}(\mathbf{G}) = \hat{\mathbf{z}}\,, \quad \hat{\zeta}_{\mathbf{k}1}(\mathbf{G}) = \hat{\mathbf{z}}\times\frac{\mathbf{k}+\mathbf{G}}{|\mathbf{k}+\mathbf{G}|} \tag{4.46}$$

the unit vectors $(\mathbf{k}+\mathbf{G})/|\mathbf{k}+\mathbf{G}|$, $\hat{\zeta}_{\mathbf{k},1}(\mathbf{G})$ and $\hat{\zeta}_{\mathbf{k},2}(\mathbf{G})$ forming a right-handed triad of unit vectors, see Fig. 4.6. Note that, unlike $\mathbf{B}_\mathbf{k}(\mathbf{G})$, the electric field $\mathbf{E}_\mathbf{k}(\mathbf{G})$ has in general a longitudinal component parallel to (**k** + **G**).

Because here are considered non-magnetic materials and that there are no currents, the Ampére-Maxwell Law reads

$$\nabla\times\mathbf{B} = -ik_0\ddot{\boldsymbol{\varepsilon}}(\mathbf{r})\cdot\mathbf{E}(\mathbf{r}) \tag{4.47}$$

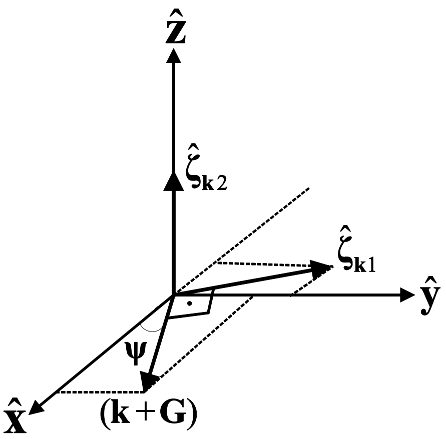

Fig. 4.6. Polarization vectors for magnetic field, Eq. (4.46), referred to coordinate axes of photonic crystal.

Multiplying this equation by $\vec{\boldsymbol{\eta}}(\mathbf{r})$, as given by Eq. (4.37), and using Eq. (4.36), it is possible to eliminate $\mathbf{E}(\mathbf{r})$ from eqs. (4.41) and (4.47). This yields the wave equation for $\mathbf{B}(\mathbf{r})$,

$$\nabla \times \left[\vec{\boldsymbol{\eta}}(\mathbf{r}) \cdot (\nabla \times \mathbf{B}(\mathbf{r})) \right] = k_0^2 \mathbf{B}(\mathbf{r}) \tag{4.48}$$

where $k_0 = \omega / c$ is the vacuum wavevector. Now, will be transform this equation to inverse space by substituting Eq. (4.38) for $\vec{\boldsymbol{\eta}}(\mathbf{r})$ and Eqs. (4.43) and (4.45) for $\mathbf{B}(\mathbf{r})$. Standard algebra leads to

$$\begin{aligned} \sum_{G'} \sum_{\lambda'=1}^{2} \left[\hat{\zeta}_{\mathbf{k}\lambda}(\mathbf{G}) \times (\mathbf{k}+\mathbf{G}) \right] \cdot \vec{\boldsymbol{\eta}}(\mathbf{G}-\mathbf{G}') \cdot \left[(\mathbf{k}+\mathbf{G}')\hat{\zeta}_{\mathbf{k}\lambda'}(\mathbf{G}') \right] \mathbf{B}_{\mathrm{k}\lambda'}(\mathbf{G}') \\ + k_0^2 \mathbf{B}_{\mathrm{k}\lambda}(\mathbf{G}) = 0, \quad \lambda = 1,2. \end{aligned} \tag{4.49}$$

In order to simplify this equation, we note that, using Eq. (4.46),

$$(\mathbf{k}+\mathbf{G}) \times \hat{\zeta}_{\mathbf{k}1}(\mathbf{G}) = \left| \mathbf{k}+\mathbf{G} \right| \hat{\zeta}_{\mathbf{k}2}(\mathbf{G}) \tag{4.50}$$

$$(\mathbf{k}+\mathbf{G})\times\hat{\zeta}_{\mathbf{k}2}(\mathbf{G}) = -\left|\mathbf{k}+\mathbf{G}\right|\hat{\zeta}_{\mathbf{k}1}(\mathbf{G}) \tag{4.51}$$

In addition, it must be expressed the dyadic $\overleftrightarrow{\boldsymbol{\eta}}$ as

$$\overleftrightarrow{\boldsymbol{\eta}}(\mathbf{G}) = \sum_{\alpha,\beta=1}^{3} \eta_{\alpha\beta}(\mathbf{G})\hat{\mathbf{e}}_{\alpha}\hat{\mathbf{e}}_{\beta} \tag{4.52}$$

in a coordinate system convenient for the PC. Naturally, we select $\hat{\mathbf{e}}_3 = \hat{\mathbf{z}}\ (=\hat{\zeta}_{\mathbf{k}2})$, see Fig. 4.6. Then Eq. (49) may be conveniently rewritten as

$$\sum_{\mathbf{G}'}\sum_{\lambda'=1}^{2}\sum_{\alpha,\beta=1}^{3} \eta_{\alpha\beta}(\mathbf{G}-\mathbf{G}')\left|\mathbf{k}+\mathbf{G}\right|\left|\mathbf{k}+\mathbf{G}'\right| \begin{bmatrix} \hat{\zeta}_{\mathbf{k}2}(\mathbf{G})\cdot\hat{\mathbf{e}}_{\alpha}\hat{\mathbf{e}}_{\beta}\cdot\hat{\zeta}_{\mathbf{k}2'}(\mathbf{G}') & -\hat{\zeta}_{\mathbf{k}2}(\mathbf{G})\cdot\hat{\mathbf{e}}_{\alpha}\hat{\mathbf{e}}_{\beta}\cdot\hat{\zeta}_{\mathbf{k}1'}(\mathbf{G}') \\ -\hat{\zeta}_{\mathbf{k}1}(\mathbf{G})\cdot\hat{\mathbf{e}}_{\alpha}\hat{\mathbf{e}}_{\beta}\cdot\hat{\zeta}_{\mathbf{k}2'}(\mathbf{G}') & \hat{\zeta}_{\mathbf{k}1}(\mathbf{G})\cdot\hat{\mathbf{e}}_{\alpha}\hat{\mathbf{e}}_{\beta}\cdot\hat{\zeta}_{\mathbf{k}1}{}'(\mathbf{G}') \end{bmatrix} \begin{bmatrix} \mathrm{B}_{\mathbf{k}1}(\mathbf{G}') \\ \mathrm{B}_{\mathbf{k}2}(\mathbf{G}') \end{bmatrix} = k_0^2 \begin{bmatrix} \mathrm{B}_{\mathbf{k}1}(\mathbf{G}) \\ \mathrm{B}_{\mathbf{k}2}(\mathbf{G}) \end{bmatrix} \tag{4.53}$$

The summation over α and β greatly simplifies because $\hat{\zeta}_{\mathbf{k}2}(\mathbf{G}) = \hat{\zeta}_{\mathbf{k}2'}(\mathbf{G}') = \hat{\mathbf{z}}$. The few surviving terms lead the final result

$$\sum_{G'}\left|\mathbf{k}+\mathbf{G}\right|\left|\mathbf{k}+\mathbf{G}'\right| \begin{bmatrix} M_{11}(\mathbf{k}+\mathbf{G},\mathbf{k}+\mathbf{G}') & M_{12}(\mathbf{k}+\mathbf{G},\mathbf{k}+\mathbf{G}') \\ M_{21}(\mathbf{k}+\mathbf{G},\mathbf{k}+\mathbf{G}') & M_{22}(\mathbf{k}+\mathbf{G},\mathbf{k}+\mathbf{G}') \end{bmatrix} \begin{bmatrix} \mathrm{B}_{\mathbf{k}1}(\mathbf{G}') \\ \mathrm{B}_{\mathbf{k}2}(\mathbf{G}') \end{bmatrix} = k_0^2 \begin{pmatrix} \mathrm{B}_{\mathbf{k}1}(\mathbf{G}) \\ \mathrm{B}_{\mathbf{k}2}(\mathbf{G}) \end{pmatrix} \tag{4.54}$$

$$
\begin{aligned}
M_{11}(\mathbf{k}+\mathbf{G},\mathbf{k}+\mathbf{G}') &= \eta_{zz}(\mathbf{G}-\mathbf{G}') \\
M_{12}(\mathbf{k}+\mathbf{G},\mathbf{k}+\mathbf{G}') &= \eta_{zx}(\mathbf{G}-\mathbf{G}')\sin\psi' - \eta_{yz}(\mathbf{G}-\mathbf{G}')\cos\psi' \\
M_{21}(\mathbf{k}+\mathbf{G},\mathbf{k}+\mathbf{G}') &= \eta_{zx}(\mathbf{G}-\mathbf{G}')\sin\psi - \eta_{yz}(\mathbf{G}-\mathbf{G}')\cos\psi \\
M_{22}(\mathbf{k}+\mathbf{G},\mathbf{k}+\mathbf{G}') &= \eta_{xx}(\mathbf{G}-\mathbf{G}')\sin\psi\sin\psi' - \eta_{yy}(\mathbf{G}-\mathbf{G}')\cos\psi\cos\psi' \\
&\quad - \eta_{xy}(\mathbf{G}-\mathbf{G}')\sin(\psi+\psi').
\end{aligned}
\tag{4.55}
$$

Here $\psi(\psi')$ is the angle between $\mathbf{k}+\mathbf{G}(\mathbf{k}+\mathbf{G}')$ and the *x*-axis.

The equation (4.54) represents a doubly infinite number of equations; *infinite,* because all values of **G** must be considered (in principle) and *doubly*, because for every value of **G** there are two components of the magnetic induction – $B_{\mathbf{k}1}(\mathbf{G})$ and $B_{\mathbf{k}2}(\mathbf{G})$. However, these two components are coupled, as already noted in Ref. [38, 107], meaning that they do *not* correspond to independent polarization modes related to the direction of the cylinders. In this context we recall that 2D PCs made from *isotropic* materials with propagation in the plane of periodicity $(\mathbf{k}\perp\hat{\mathbf{z}})$, support an *E-mode* with **E**(**r**) parallel to the cylinders and an *H-mode* with **H**(**r**) or **B**(**r**) along the cylinders. This separation into two polarizations is dictated by the existence of a mirror symmetry plane perpendicular to the homogeneous cylinders, such that $\varepsilon(-z) = \varepsilon(z)$. On the other hand, no such plane exists for the NLC cylinders. This is so because the positive and negative *z*-directions are not equivalent; note that there are no NLC molecules, in our description, with *downward* – pointing directors (always $\hat{\mathbf{n}}\cdot\hat{\mathbf{z}} > 0$). This asymmetry originates in an implicit impurity at $z = +\infty$ that attracts the molecules *upward.* Eq. (4.54) thus describes a situation not unlike that of a 3D PC, where the components of the magnetic field are also coupled.

Now consider what happens for *super-critical fields* $E_0 > E_c$. In this axial configuration the dielectric dyadic is given by eq. (4.35). Then the inverse dyadic (as also follows directly from Eq. (4.37) upon substituting $\theta = 0$) is

$$\overset{\leftrightarrow}{\boldsymbol{\eta}}_{AX} = \begin{pmatrix} 1/\varepsilon_o & 0 & 0 \\ 0 & 1/\varepsilon_o & 0 \\ 0 & 0 & 1/\varepsilon_e \end{pmatrix} \tag{4.56}$$

independent of position, as long as **r** is within a NLC cylinder. The Fourier transform is gotten from Eq. (4.40):

$$\overset{\leftrightarrow}{\boldsymbol{\eta}}_{AX}(\mathbf{G}) = \begin{pmatrix} \varepsilon_o^{-1} - \varepsilon_b^{-1} & 0 & 0 \\ 0 & \varepsilon_o^{-1} - \varepsilon_b^{-1} & 0 \\ 0 & 0 & \varepsilon_e^{-1} - \varepsilon_b^{-1} \end{pmatrix} \frac{1}{A_c} \int_{A_c} dA e^{-i\mathbf{G}\cdot\mathbf{r}} \quad , \quad \mathbf{G} \neq 0 \tag{4.57}$$

The integral over the cylinder cross-sectional area gives rise to a Bessel function, namely the well-known form factor $F\left(|\mathbf{G}|R\right) = J_1\left(|\mathbf{G}|R\right)$ for circular cylinders. The matrix has the usual uni-axial structure, with

$$\begin{aligned} &\eta_{xx}^{AX}(\mathbf{G}) = \eta_{yy}^{AX}(\mathbf{G}) = \left(\frac{1}{\varepsilon_o} - \frac{1}{\varepsilon_b}\right) \frac{2fJ_1(GR)}{GR} \equiv \eta_H\left(GR\right) \\ &\eta_{zz}^{AX}(\mathbf{G}) = \left(\frac{1}{\varepsilon_e} - \frac{1}{\varepsilon_b}\right) \frac{2fJ_1(GR)}{GR} \equiv \eta_E\left(GR\right) \\ &\eta_{\alpha\beta}^{AX}(\mathbf{G}) = 0 \qquad \text{for} \quad \alpha \neq \beta, \qquad \mathbf{G} \neq 0. \end{aligned} \tag{4.58}$$

For **G** = 0, the average of $\overset{\leftrightarrow}{\boldsymbol{\eta}}(\mathbf{r})$ over the unit cell gives, simply

$$\begin{aligned} &\eta_H(0) = \frac{1}{\varepsilon_o} f + \frac{1}{\varepsilon_b}(1-f), \\ &\eta_E(0) = \frac{1}{\varepsilon_e} f + \frac{1}{\varepsilon_b}(1-f), \qquad f = \frac{\pi R^2}{A_c}, \end{aligned} \tag{4.59}$$

where *f* is the cylinder filling fraction. Eq. (4.55) then become

$$\begin{aligned}
&M_{11}^{AX}(\mathbf{k}+\mathbf{G},\mathbf{k}+\mathbf{G}') = \eta_E\left(\left|\mathbf{G}-\mathbf{G}'\right|R\right) \\
&M_{12}^{AX}(\mathbf{k}+\mathbf{G},\mathbf{k}+\mathbf{G}') = M_{21}^{AX}(\mathbf{k}+\mathbf{G},\mathbf{k}+\mathbf{G}') = 0 \qquad (4.60) \\
&M_{22}^{AX}(\mathbf{k}+\mathbf{G},\mathbf{k}+\mathbf{G}') = \eta_H\left(\left|\mathbf{G}-\mathbf{G}'\right|R\right)\cos(\mathbf{k}+\mathbf{G},\mathbf{k}+\mathbf{G}')
\end{aligned}$$

The matrix in Eq. (4.54) then becomes diagonal, so that this equation reduces to

$$\sum_{G'} \eta_E\left(\left|\mathbf{G}-\mathbf{G}'\right|R\right)\left|\mathbf{k}+\mathbf{G}\right|\left|\mathbf{k}+\mathbf{G}'\right|\mathrm{B}_{\mathbf{k}1}(\mathbf{G}') = k_0^2\mathrm{B}_{\mathbf{k}1}(\mathbf{G}) \qquad (4.61)$$

$$\sum_{G'} \eta_H\left(\left|\mathbf{G}-\mathbf{G}'\right|R\right)\left(\mathbf{k}+\mathbf{G}\right)\cdot\left(\mathbf{k}+\mathbf{G}'\right)\mathrm{B}_{\mathbf{k}2}(\mathbf{G}') = k_0^2\mathrm{B}_{\mathbf{k}2}(\mathbf{G}) \qquad (4.62)$$

Eq. (4.61) involves only the field component $\mathrm{B}_{\mathbf{k}1}(\mathbf{G})$, but not the component $\mathrm{B}_{\mathbf{k}2}(\mathbf{G})$, while it is the other way round for Eq. (4.62). This means that, in the axial configuration, we have two independent polarizations. By Eqs. (4.45) and (4.46) $\mathrm{B}_{\mathbf{k}1}(\mathbf{G})$ is the component that is perpendicular to the cylinders. Then it follows from Eq. (4.44) that the accompanying electric field $\mathbf{E}_{\mathbf{k}1}(\mathbf{G})$ must be parallel to the cylinders. Hence, Eq. (4.61) is an eigenvalue equation for *E-modes*. By similar reasoning, Eq. (4.62) governs the *H-modes*, their magnetic field being parallel to the cylinders. However, when comparing with the corresponding eigenvalue equations for isotropic cylinders, a word or caution is in order: unlike the case of isotropic cylinders, in Eqs. (4.61) and (4.62) the Fourier coefficients $\eta_E(GR)$ and $\eta_H(GR)$ are different. From Eq. (4.59) we see that the only difference arises from having to use the extraordinary dielectric constant ε_e of the NLC for the E-modes, while the ordinary dielectric constant ε_o applies to the *H-modes*.

Summarizing, for supercritical fields $E_0 > E_c(R)$, the general eigenvalue equation (4.54) – corresponding to complex polarization of the fields – decomposes into the two eigenvalue equations (4.61) and (4.62) that determine, respectively, the properties of modes polarized with their electric field parallel and perpendicular to the cylinders.

4.6 Approximate photonic band structure

This approximate approach is based on the intuitive idea of replacing the dielectric dyadic $\vec{\vec{\boldsymbol{\varepsilon}}}(r,\varphi)$, Eq. (4.34), by its average $<\vec{\vec{\boldsymbol{\varepsilon}}}>$ over the cross-sectional area of a NLC cylinder, namely

$$<\vec{\vec{\boldsymbol{\varepsilon}}}>=\frac{1}{\pi R^2}\int_0^R rdr\int_0^{2\pi} d\varphi\,\vec{\vec{\boldsymbol{\varepsilon}}}(r,\varphi) \tag{4.63}$$

From Eq. (4.34) we see that the off-diagonal elements all vanish and the diagonal elements are

$$\begin{aligned} &<\varepsilon_{xx}>=<\varepsilon_{yy}>=\varepsilon_o+\varepsilon_a\int_0^1 dx\cdot x\sin^2\theta(x)\equiv\varepsilon_H(q) \\ &<\varepsilon_{zz}>=\varepsilon_o+2\varepsilon_a\int_0^1 dx\cdot x\cos^2\theta(x)\equiv\varepsilon_E(q) \end{aligned} \tag{4.64}$$

the field parameter *q* being given by Eq. (4.13). It must be note that ε_H and ε_E are related by

$$2\varepsilon_H(q)+\varepsilon_E(q)=2\varepsilon_o+\varepsilon_e=const \tag{4.65}$$

It is interesting that an intrinsically *positive nematic* ($\varepsilon_e > \varepsilon_o$) may become *effectively negative*, in the sense that $\varepsilon_E(q) < \varepsilon_H(q)$ for a range of field strengths – and *vice versa* for an intrinsically *negative nematic* ($\varepsilon_e < \varepsilon_o$). It can even happen that $\varepsilon_E(q)$ and $\varepsilon_H(q)$ become equal for some value of q, corresponding to isotropy in the average of the NLC cylinder.

By Eq. (4.64), the inverse dielectric tensor is

$$\vec{\vec{\boldsymbol{\eta}}} \equiv < \vec{\vec{\boldsymbol{\varepsilon}}} >^{-1} = \begin{pmatrix} 1/\varepsilon_H(q) & 0 & 0 \\ 0 & 1/\varepsilon_H(q) & 0 \\ 0 & 0 & 1/\varepsilon_E(q) \end{pmatrix}, \quad r < R \tag{4.66}$$

This has the same uniaxial structure as Eq. (4.56), obtained for supercritical fields – which is *not* the case being considered at this point – however with ε_o and ε_e replaced, respectively, by ε_H (q) and ε_E (q). Thus it is possible to directly conclude that the present approximation leads to the eigenvalue equations (4.61) and (4.62), however with η_E and η_H *not* given by the Eq. (4.58), but rather by

$$\eta_E(GR) = \begin{cases} \dfrac{1}{\varepsilon_E(q)} f + \dfrac{1}{\varepsilon_b}(1-f), & \mathbf{G} = 0 \\ \left[\dfrac{1}{\varepsilon_E(q)} - \dfrac{1}{\varepsilon_b} \right] F(GR), & \mathbf{G} \neq 0 \end{cases} \tag{4.67}$$

$$\eta_H(GR) = \begin{cases} \dfrac{1}{\varepsilon_H(q)} f + \dfrac{1}{\varepsilon_b}(1-f), & \mathbf{G} = 0 \\ \left[\dfrac{1}{\varepsilon_H(q)} - \dfrac{1}{\varepsilon_b} \right] F(GR), & \mathbf{G} \neq 0 \end{cases} \tag{4.68}$$

As will be seen then, the approximate calculation leads to independent *E*- and *H-modes* even for subcritical fields [$E_0 < E_c(q)$].

4.7 Graphical results

In Ref. [78] have been computed the components $\mathbf{B}_{\perp}(\mathbf{r})$ and $\mathbf{B}_{\|}(\mathbf{r})$ of the magnetic field eigenvectors, corresponding to the directions perpendicular and parallel to the cylinders, respectively. It was found that $\mathbf{B}_{\perp}(\mathbf{r})$ is the dominant component (with $B_{\|}(\mathbf{r}) \ll B_{\perp}(\mathbf{r})$) in the *first* and *third* photonic bands. These two bands then can be said to have *nearly-E* or *quasi-E* polarization, even though, of course, we are concerned now with subcritical fields. Just the opposite occurs for the\ *second* band, which turns out to be characterized by $B_{\|}(\mathbf{r}) \gg B_{\perp}(\mathbf{r})$; to this situation we refer as *nearly-H* or *quasi-H* polarization. This suggests that the usual separation into *E*- and *H-modes* might be approximately valid for NLC-infilled two-dimensional PCs - at least for the low-lying photonic bands. The approximate theory presented in the previous sections led, precisely, to independent *E*- and *H-modes*. It is then instructive to compare band structures calculated from Eqs. (4.61) and (4.62) with the substitution of Eqs. (4.67) and (4.68) with exact band structures from Eq. (4.54). This is done in Fig. 4.7 for the *5CB* NLC cylinders in a silicon oxide (silica) host (square lattice), using our results for the director inclination $\theta(x)$.

About the first 6 bands are shown in Fig. 4.7 for $q = 20$. It is seen that, in general, the approximate bands for either the *E*- or the *H-polarization* nearly coincide with one of the exact bands. The fit is excellent for lower lying bands and it is very good even for the higher ones. This then justifies the concept of *nearly-E* and *nearly-H* polarizations and the use of much simpler approximate calculation in section 4.6. Here is important to note that, the higher the value of *q*, the more the NLC directors align with the cylinders and the better this concept of quasi-polarization is expected to work. In fact, for $q \geq q_c$ the modes are strictly separated into the *E*- and *H*-polarizations.

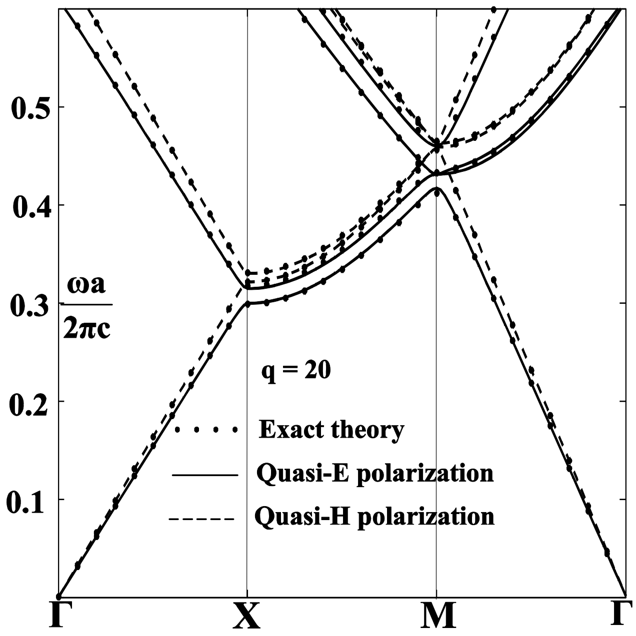

Fig. 4.7. Comparison of exact (dots) and approximate (lines and dashed lines) photonic band structures for *5CB* nematic liquid crystal cylinders forming a square lattice in a silica host, for the field parameter $q = 20$. The exact solutions follow from Eq. (4.54), while the approximate solutions are obtained from Eqs. (4.61) and (4.67) for *E-polarized* light (lines) and from Eqs. (4.62) and (4.68) for *H-polarized* light (dashed lines). Here $\sigma = 8$ ($R = 0.2\mu m$), $\varepsilon(\mathrm{SiO_2}) = 2.1$, and the cylinder filling fraction is $f = 0.7$. The high-frequency (optical) dielectric constants of the *5CB* NLC are $\varepsilon_o = 2.403$ and $\varepsilon_e = 3.008$. The figure demonstrates that the exact modes are, actually, either *nearly E-polarized* or *nearly H-polarized*.

The Fig. 4.8a, shows the band structure for the case $q \geq q_c$. As a consequence of the low dielectric contrast there is no complete band gap, but there exist partial band gaps for both polarizations in the [100] direction. These partial band gaps are tuned by the external DC electric field as shown by the Figs. 4.8b and 4.8c for the *E*- and *H-modes*, respectively. We should note that for $q = 0$, both gaps share a frequency region around ~ 0.32. When the q parameter is increased, the *E-band* gap shifts downwards and the *H-band* gap shifts upwards in frequency.

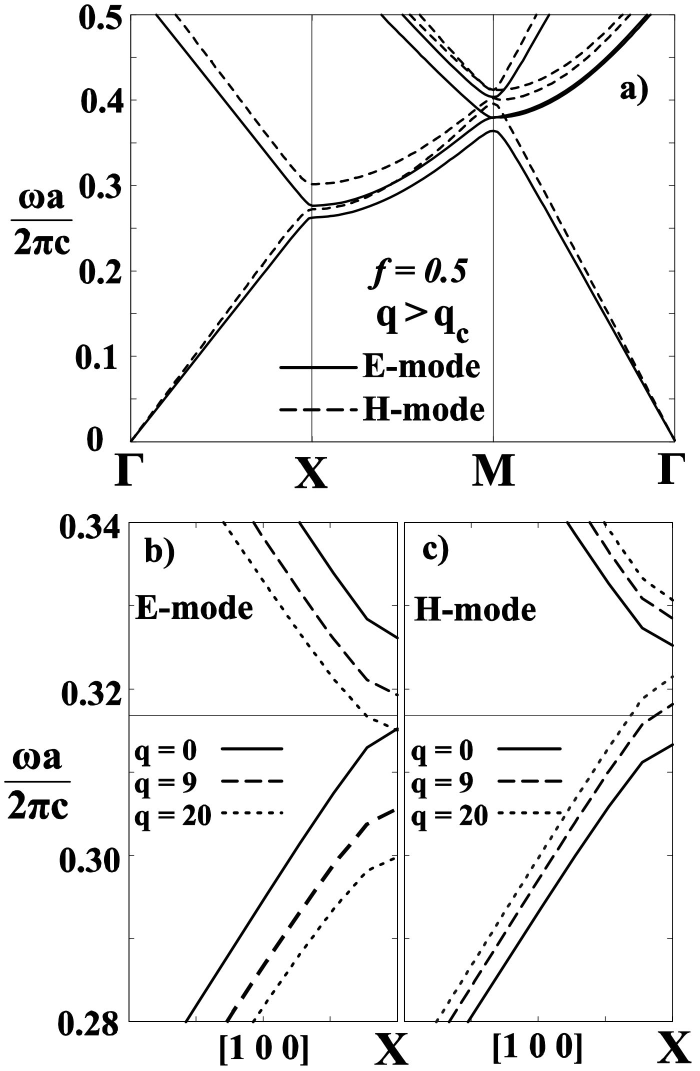

Fig. 4.8 Electrical tuning of the photonic bands for the photonic crystal considered in the previous figure. In (a) is shown the band structure for a supercritical electric field having induced a phase transition. Here the modes are strictly *E* and *H*. (b) and (c) show the tuning of the partial band gap in the [100] direction for *quasi-E* and *quasi-H* polarizations, respectively. Note that both band gaps share a frequency region and both can be shifted by the external DC electrical field.

Now, if unpolarized light with a normalized frequency of 0.317 is incident at the PC in the direction [100] and there is no applied field, all the light will be reflected. When q is increased a little ($q = 9$), the *E-polarized* component of the light will still be reflected, while now the *H-polarized* component will be transmitted. Finally, all the light will be transmitted for any value of q greater than 20. This demonstrates a significant application of NLC-infilled PCs, namely polarizers whose optical response can be tuned or switched by means of an applied field.

4.8 Conclusions

In the first part of this chapter the configuration of NLC molecules within an infinite circular cylinder was determined. Namely, was calculated the angle θ(r), formed by NLC director as function of radial distance and applied axial electric field, for a cylinder of given radius and specified elastic and surface parameters of the nematic (chosen to be *5CB*). It was come to the conclusion that, for a given radius, the configuration is *escaped radial* up to rather high fields. However, for a critical value of this DC field, a phase transition occurs to the axial configuration, with all the directors aligned with the cylinder axis. It was determined the value of this critical field as function of the cylinder radius. For radii that are not very small (R ≥ 50 nm), the critical field is $E_c \simeq 14\ V/m$.

The NLC directors $\hat{\mathbf{n}}(\theta)$ lead to the dielectric tensor ε_{ij} (r) of the NLC cylinder. In turn, this paved the way toward the eigenvalue equation that yields the photonic band structure. This was obtained for hollow cylinders in silica infilled a Ge-based PC's infilled with the nematic *5CB*. It is important to note that, in principle, there are *no* independent E- and H-modes, as is the rule for ordinary two-dimensional PCs with propagation in the plane of periodicity. That is, the electric and magnetic fields possess components both parallel and perpendicular to the cylinders. This is occasioned by the special anisotropy of the nematic molecules that in the model *escape upwards* from the radial direction; hence there is no mirror plane parallel to the plane of periodicity – a requisite for E- and H- polarized waves. Nevertheless, it turns out – at least for the examples that were studied – that each band is characterized by either $E_{\|} \gg E_{\perp}$ and $H_{\|} \ll H_{\perp}$ or by $E_{\perp} \gg E_{\|}$ and $H_{\perp} \ll H_{\|}$. In other words, it is useful to classify the bands as quasi-E or quasi-H polarized. To what extent this classification is good for other NLCs or host materials (with smaller dielectric contrast than for Si or Ge) or for different values of the cylinder radius – is an open question. It was found that the quasi-E and quasi-H bands can be tuned by a DC electric field and that a quasi-E band gap can be completely closed for a high enough field value. In spectral range, incident light polarized with its electric field in the z-direction can be switched on and off by means of the external field. The PC can also serve as a polarization filter controlled by E_0, permitting the transmission through the PC of only H-component of *unpolarized* incident light.

Finally it is important to comment that we also developed an approximate approach, based on the averaging of the dielectric tensor of the NLC over the cross-sectional area of the cylinder. This gives rise to great simplification, because $<\vec{\boldsymbol{\varepsilon}}>$ turns out to be diagonal. As a result, the electromagnetic modes of the PC become, in this approximation, strictly E- or H-polarized. It was found that the photonic bands corresponding to these polarizations very nearly coincide with one of the bands calculate exactly. Clearly, averaging over the cylinder cross-section in equivalent to neglecting the non-dominant field components – $E_{\perp}$ for the quasi-E polarization and $H_{\perp}$ for the quasi-H polarization. Clearly the approximate calculation works so well because the exact fields *are* nearly E- or H-polarized! If applied when appropriate, the approximate calculation can give valid results by means of a simpler and time-saving calculation.

As a final observation, it has been considered only three configurations of the NLC enclosed within a cylinder: the escaped radial, the planar radial, and the axial. It was, however, not studied the planar polar configuration which is supposed to form due to imperfections on the cylinder walls. Hence, this work implicitly assumes that defects occur only at one end of long, open tubes of the PC that contain the NLC. It is this situation that should lead to all the NLC molecules *escape* in only one *vertical*, but not lateral, direction.

This work is expected to facilitate a more quantitative approach to the study of NLC-infilled PCs.

Chapter 5

Electrical tuning of refraction in a two-dimensional photonic crystal infilled with a liquid crystal

(Article with the same title by J. A. Reyes-Avendaño and P. Halevi, Rev. Mex. Fís. **54**(6), 407-410(2008)).

In this chapter a novel electro-optic system is propose with potential applications for ray steering, optical multiplexers, logic gates or switches. The idea is based on the electrical tuning of refraction in a two-dimensional photonic crystal (PC) infilled by a liquid-crystal, with a direct-current electric field applied parallel to the cylinders. Using a two-step homogenization process, is shown that, for sufficiently low frequencies, this structure can be represented by two field-dependent effective refractive indices. It is demonstrate that the direction of the ordinary and extraordinary refracted rays can be sensitively tuned by varying the magnitude of the applied field.

5.1 Introduction

In this work is proposed a simple electro-optic device which, for example, could be an element in integrated photonic platforms that incorporate photonic crystals (PCs). Specifically, is considered the electrical tuning of a photonic crystal (PC) infilled with a nematic liquid crystal (NLC). With an electric field applied parallel to the cylinders of a two-dimensional (2D) PC, for sufficiently low frequencies the composite material can be replaced by a uniform, uniaxial optical medium. Taking advantage of such simple description, it is demonstrated that the directions of the refracted ordinary and extraordinary rays can be steered by varying the magnitude of the applied field, with up to ~ 7% change in the angle of refraction.

It seems that the most promising manner of tuning of PCs is based on their infilling by a NLC – tunable by means of pressure, temperature, or an applied magnetic or electric field. As for applications, electric control of the optical response is the most promising. Indeed, the first paper on this subject [102] has motivated many studies of NLC-infilled PCs [32, 78, 118, 119, 121, 135-138]. Now, while several theoretical papers dealed with very large electric fields (above the Freedericksz transition) that have to be rotated with respect to the PC (in order to alter the orientations of the NLC molecules) this scheme proved to be unattractive for experimentation. On the other hand, experimental work with a fixed direction of the field – tuning its magnitude – prospered [135-137]. Most theoretical (experimental) papers are concerned with tuning of the PBG (reflectance or transmittance). Up to now, there are only five studies [34-38] dedicated to the tuning of refraction and merely one of these [38] is based on NLCs, assuming (cumbersome) rotation of the field or the PC. In this work is presented an explicit simulation of sensitive ray steering, with the magnitude of the field as tuning agent.

In the aforementioned references the wavelength λ is on the order of the PC lattice constant *a* (PBG region). The frequency region much below the PBG has received much less attention. When $\lambda \gg a$, the structure behaves like a traditional optical element and can be characterized by an effective refractive index n_{eff}. Such *homogenization* of composites has been accomplished for PCs with isotropic ingredients [10, 65, 89, 139].

5.2 Homogenization process and tuning

In this work, it is homogenized a 2D PC of cylinders infilled with the NLC *5CB* in a silicon oxide (silica) matrix. Here it is important to stress the advantages of silica as host medium, rather than silicon, for example. The free carriers in a semiconductor screen out the applied electric field; this problem can be overcome by a specially designed capacitor, increasing however the complexity of the structure (see the last ref. 3). In addition, because here PBGs aren't of concern, having a low dielectric contrast (between the NLC and the silica glass) actually leads to more sensitive ray steering. The homogenization results in an effective uniaxial medium characterized by two refractive indices: the ordinary n_o and the extraordinary n_e. When an electric field $\mathbf{E_0}$ is applied parallel to cylinder axis $\hat{\mathbf{z}}$, both indices change their values continuously as function of E_0. As a result, an unpolarized incident beam with $\lambda \gg a$ splits into two refracted beams inside the PC: the ordinary or E mode (with $\mathbf{E} \parallel \hat{\mathbf{z}}$) and the extraordinary or H mode (with its magnetic field $\mathbf{H} \parallel \hat{\mathbf{z}}$). As will be made evident below, both angles can be tuned by the applied field E_0 by about 2.3° for the E-mode and 1.2° for the H-mode.

In a recent study [78, 138] it was shown that, when the external electric field is absent, the NLC molecules inside the cylinder adopt the *escaped radial configuration*. In this configuration, the angle θ formed between the NLC molecule axis $\hat{\mathbf{n}}$ (the *director*) and the cylinder axis $\hat{\mathbf{z}}$ increases with the radial distance r. For molecules at the cylinder's center θ = 0° and, for relatively wide cylinders, θ can reach almost 90° for molecules at the cylinder's wall [inset (a) Fig 5.1]. The external DC electric field $\mathbf{E_0}$ changes the NLC molecules' directions**,** decreasing θ as a function of E. When E_0 reaches a critical value E_c, a phase transition is induced in the NLC. All the NLC molecules in the cylinder are then aligned in the $\hat{\mathbf{z}}$ direction and any E_0 greater than E_c will leave unaltered this *axial configuration* [inset (b) Fig. 5.1]. In ref. [78, 138] the cylinder, subject to the applied field $E_0\hat{\mathbf{z}}$, was characterized by a non-diagonal dielectric tensor $\tilde{\varepsilon}(r)$ whose elements depend on the angle $\theta_E(r) = (\hat{\mathbf{n}}, \hat{\mathbf{z}})$, as well as on the ordinary and extraordinary dielectric constants $\varepsilon_o = n_o^2$ and $\varepsilon_e = n_e^2$. Now, when $\tilde{\varepsilon}(r)$ is averaged over the cross-sectional area of the cylinder, it becomes diagonal, with the uni-axial structure

$$\langle \tilde{\varepsilon}_{xx} \rangle = \langle \tilde{\varepsilon}_{yy} \rangle = \varepsilon_o + \varepsilon_a \int_0^1 dx \cdot x \sin^2 \theta(x) \equiv \varepsilon_H(q) \tag{5.1}$$

$$\langle \tilde{\varepsilon}_{zz} \rangle = \varepsilon_o + 2\varepsilon_a \int_0^1 dx \cdot x \cos^2 \theta(x) \equiv \varepsilon_E(q), \quad q = \varepsilon_A R^2 E_0^2 / K_{11} \tag{5.2}$$

Here, q is a convenient dimensionless field parameter, $\varepsilon_A = \varepsilon_E - \varepsilon_O$ $(\varepsilon_a = \varepsilon_e - \varepsilon_o)$ is the static (optical) *anisotropy*, R is the cylinder radius, K_{11} is an elastic constant of the NLC, and $x = r/R$. Clearly, the optical response of the NLC cylinder is governed by the effective ordinary (extraordinary) dielectric constants $\varepsilon_H(\varepsilon_E)$ if $\mathbf{H}(\mathbf{E}) \parallel \hat{\mathbf{z}}$ – which justifies the subscript H(E). Fig. 5.1 shows the variation of $\varepsilon_{H,E}$ with q. As this parameter increases, ε_E increases from 2.24 to 2.54, while ε_H decreases from 2.29 to

2.15, approximately. It is important that, for $q > q_c = 271.4$, ε_E and ε_H do not change further.

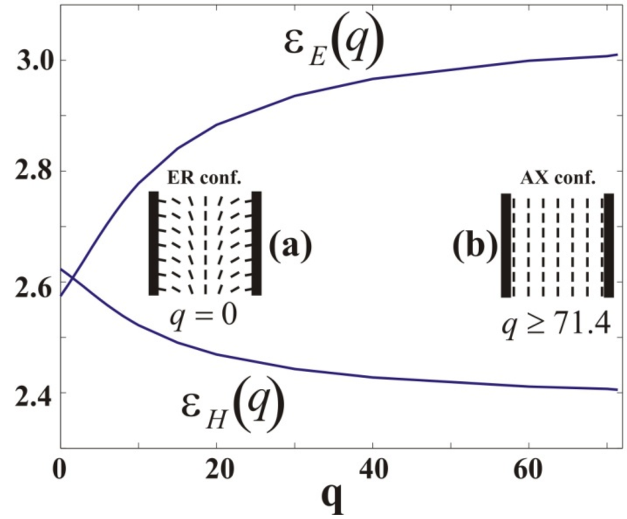

Fig. 5.1 Average dielectric constants ε_E (ε_H) of a nematic liquid crystal cylinder for electric field E (magnetic field H) parallel to the cylinder, as function of the electric field parameter q. For $q < 271.4$ ($E_0 < 14$ V/μm), the NLC molecules adopt the Escaped.

Using these ideas it is possible to represent the PC of NLC cylinders (Fig. 5.2a) as in Fig. 5.2b, and the optical response can be calculated as usual for PCs made of homogeneous and isotropic dielectric materials. In the refs. [78, 138] it has been demonstrated that this simple averaging over the cross-sectional area of a cylinder reproduces very well the exact photonic band structure for *5CB* NLC cylinders in both a silicon and a silica host. This completes the first step of homogenization.

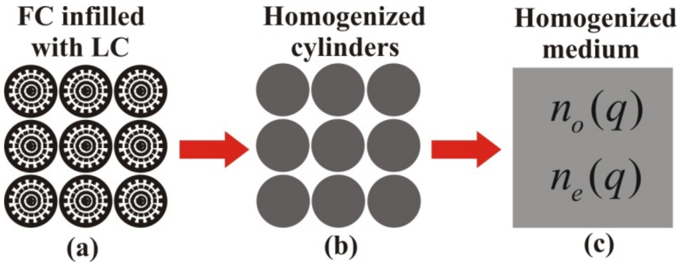

Fig. 5.2 PC homogenization process. In (a), the PC is represented by a dielectric tensor for the region inside the NLC cylinders and a dielectric constant for the host region (ε_{silica} = 1.96 in the infrared region [141]). In (b), the structure is simplified, replacing the NLC cylinders by a uniform medium with ε depending on E0 for each polarization. In (c), the PC of two (now uniform) components is replaced by a single uniform medium, characterized by a pair of field-dependent effective indices, corresponding to ordinary and extraordinary modes.

Next, as mentioned, for $\lambda \gg a$ it is possible to proceed to the second step – complete homogenization of the PC – as indicated in Fig. 5.2c. For the two-dimensional PC (Fig. 5.2b), the final value of ε_{eff} can be calculated using the methods of refs. [10, 65, 89]. Both calculations give the same result. For E-polarization, the result of homogenization is simple and yields the effective extraordinary index $n_e(q)$:

$$\left\langle \varepsilon_E(q) \right\rangle = \varepsilon_E(q)\left(\pi R^2/a^2\right) + \varepsilon_{SiO_2}\left(1-\pi R^2/a^2\right) \equiv n_e^2(q) \tag{5.3}$$

Here *a* is the period of the square lattice and the expressions in the parentheses are the NLC and silica filling fractions. The formulas for H-polarization, namely $\left\langle \varepsilon_H(q) \right\rangle \equiv n_o^2(q)$, can be found in the refs. [10, 65, 89] and provide the effective ordinary index $n_o(q)$. The fractional changes of these indices,

$$\frac{\Delta n_{o,e}(q)}{n_{o,e}(0)} = \frac{n_{o,e}(q) - n_{o,e}(0)}{n_{o,e}(0)} \tag{5.4}$$

are plotted in Fig. 5.3. It is observed that the applied electric field can tune the effective index by up to ~ 6%. Here it is important to note that the larger changes occur for modest values of the applied electric field ($E_0 \leq 5\,V/\mu m$), and it is not necessary to reach the phase transition (at $E_0 = 14\,V/\mu m$) to get a significant tuning.

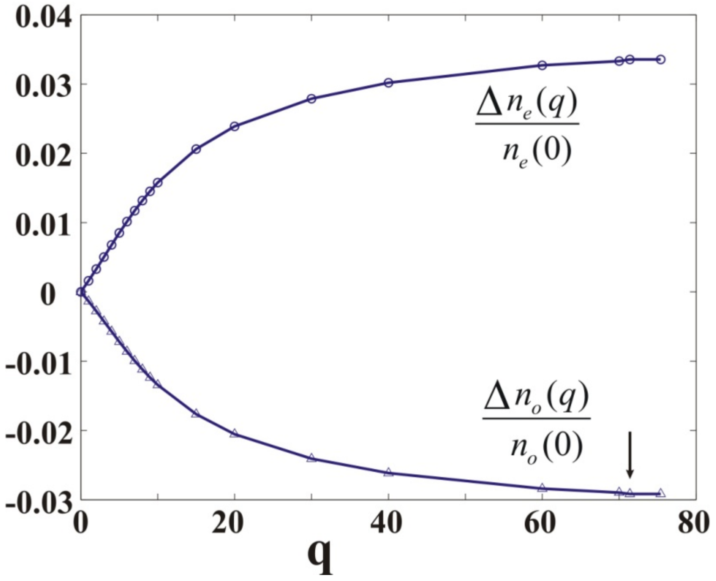

Fig. 5.3 Relative changes of the effective refractive indices of a two-dimensional PC of NLC cylinders in a silica matrix, as the applied electric field changes from zero beyond its critical value; see top coordinate E_0 (in V/μm) for our chosen parameters.. The PC lattice constant is a = 0.85 μm and R = 0.4 μm. As q increases, the ordinary (extraordinary) refractive index decreases (increases) up to a limiting value for E_0 = 14 V/μm, indicated by the arrow. For any q beyond this value, both indices remain unchanged. Both curves are well fitted up to q = 100 (the most significant interval for tuning) by series of the form $\Delta n(q)/n(0) = \sum_{n=0}^{5} a_n q^n$. The coefficients for the ordinary (extraordinary) mode are a_0 = 0.00015 (0.00031), a_1 = -0.001301 (0.002813), a_2 = 2.83 x 10^{-5} (-6.544 x 10^{-5}), a_3 = -3.03 x 10^{-7} (7.819 x 10^{-7}), a_4 = 1.338 x 10^{-9} (-4.333 x 10^{-9}), a_5 = -1.116 x 10^{-12} (8.231 x 10^{-12}).

Finally, in Fig. 5.4 are shown the variations of the refraction angles, for both the ordinary and extraordinary rays, considering an angle of incidence $\theta_i = 60°$. An unpolarized beam incident at the PC, with its saggital plane perpendicular to the cylinders, will split into the ordinary and the extraordinary beams. As the applied field increases, θ_o increases and θ_e decreases, reaching saturation at the phase transition.

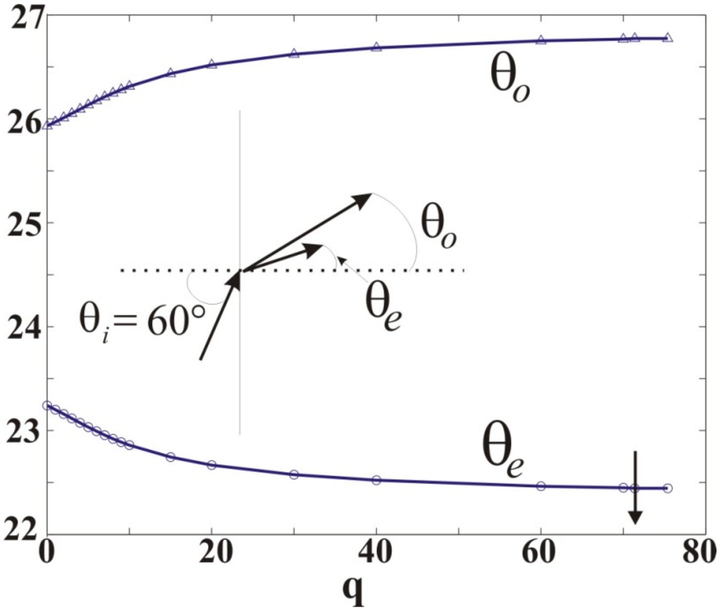

Fig. 5.4 Angles of refraction for ordinary and extraordinary rays in the homogenized medium. As q increases, the angle between the refracted beams increases until a phase transition occurs in the LC, as indicated by the arrow.

5.3 Conclusions

It has been calculated the refractive angles for light incident at a 2D PC, employing a two-step homogenization process. The first one leads to the effective dielectric constants $\varepsilon_E(q)$ and $\varepsilon_H(q)$ that characterize the NLC cylinders for a given external field E_0. The second step completes the homogenization, representing the entire NLC-infilled PC by an effective index for each polarization. Because of the uniaxial nature of the homogenized medium, the incident electromagnetic wave splits into two beams. The refractive angles of these (ordinary and extraordinary) rays can be continuously varied up to ~ 6% in comparison to the fieldless case (for $\theta_i = 60^o$). The second step of homogenization requires that $\lambda \gg a$, that is, the linear region of the PC's band structure, where $\omega \simeq kc/n_{o,e}(q)$. This implies, typically, the infrared regime. If the PC is placed in a capacitor of width ~ 15 μm, efficient tuning could be achieved with voltages up to about 70 V. The method described could be used for ray steering, for example employing a PC prism as proposed in ref. [140]. Another potential application is based on a PC lens, as suggested in ref. [139], now with the possibility of tuning the lens's focus. Further applications to be considered are optical multiplexers (where the electromagnetic wave path can be selected by external agents), optical logic gates or optical switches.

Chapter 6

Conclusions

In this thesis there has been carried out a study of aspects of two-dimensional photonic crystals related to the long-wavelength limit and to the tuning of the optical properties by using a nematic liquid crystal as an element of the system. This work is based on three main parts, namely, the homogenization process, the interaction between a DC electric field and a photonic crystal of void cylinders infilled with a liquid crystal, and finally, the tuning of the effective parameters by an external agent.

As a consequence of the anisotropy of a two-dimensional photonic crystal, the homogenization process was divided into two limiting cases: the in-plane propagation and the axial propagation. For the in-plane propagation, the homogenization process was achieved by employing the mean field theory proposed by P. Halevi and F. Pérez-Rodríguez [1,2] which can be used to compute the effective parameters of dielectric and metallo-dielectric photonic crystals with periodicity in one-, two-, or three-dimensions. This very general process can lead to the usual dielectric response ($\mathbf{D} = \overleftrightarrow{\boldsymbol{\varepsilon}}(\mathbf{k}) \cdot \mathbf{E}$, $\mathbf{B} = \mu_0 \mathbf{H}$) or to the more general bi-anisotropic response ($\mathbf{D} = \overleftrightarrow{\boldsymbol{\varepsilon}} \cdot \mathbf{E} + \overleftrightarrow{\boldsymbol{\gamma}} \cdot \mathbf{H}$, $\mathbf{B} = \overleftrightarrow{\boldsymbol{\delta}} \cdot \mathbf{E} + \overleftrightarrow{\boldsymbol{\mu}} \cdot \mathbf{H}$) with the permittivity ($\overleftrightarrow{\boldsymbol{\varepsilon}}$), permeability ($\overleftrightarrow{\boldsymbol{\mu}}$), and crossed magneto-electric ($\overleftrightarrow{\boldsymbol{\gamma}}, \overleftrightarrow{\boldsymbol{\delta}}$) dyadics expressed in terms of the unit cell and Bravais lattice. Unlike the non-local dielectric response, the bi-anisotropic response allows the magnetic properties to emerge at the macro-level. In the case of axial propagation it was necessary to extend the theory proposed in Refs. [89, 90] and derive new equations that take into account the special behavior of the wave vector component parallel to the cylinders. Because this component is parallel to a translationally invariant direction, it is an ordinary wave vector and no restrictions are imposed over it –in contrast with the in-plane component which must satisfy the Bloch theorem and remain small enough in the long-wavelength limit. The derivation showed that there are no magnetic effects for this direction of propagation, leaving unuseful the bi-anisotropic response derived in Ref. [89, 90].

The numerical results obtained for the in-plane propagation showed that in the case of dielectric photonic crystals there are no magnetic effects ($\mu = \mu_0$), and the value obtained for the effective permittivity is in agreement with other theories in the literature. Nevertheless, the results presented here go beyond the conventional local theories and can be applied even for Bloch wave vectors as large as $\pi/4a$. A more interesting result was found in metallo-dielectric photonic crystals where a paramagnetic or diamagnetic behavior is obtained as a function of the polarization. If the electric field is parallel to the cylinders, the effective permeability shows a paramagnetic behavior that increases as the frequency does. If the electric field is perpendicular to the cylinders, a strong diamagnetic behavior is observed and increases as the filling fraction does. It is important to stress that within the typical low-frequency band gap observed for the E-modes in a wire medium, the effective permittivity and the effective permeability have opposite signs resulting in an imaginary effective refractive index as corresponds to the inhibition of the electromagnetic wave propagation.

In the case of axial propagation, in order to get a better interpretation of the numerical results obtained for the effective permittivity dyadic, an analysis was performed about the polarization in the first two dispersion bands. By plotting the electric and magnetic fields within the unit cell, it was found that in the long wavelength limit, the first band in the dispersion relation has a transversal polarization while the second band has a longitudinal polarization. In addition, the figures show that the oscillations of the electromagnetic fields within the unit cell strongly depend on the frequency. Only for sufficiently low frequencies does the homogenization theory give satisfactory results for the second band. This can be achieved in a photonic crystal of thin metallic wires. The effective permittivity computed for the first band (with transversal polarization) of dielectric structures showed good agreement with the results obtained from the dispersion relation. On the other hand, the homogenization processes fails in the second band as a consequence of the strong oscillations of the electric field within the unit cell. In the case of metallo-dielectric structures we analyzed a square lattice of thin metallic wires made of aluminum and cooper. The filling fraction was selected to be very small in order to obtain a low frequency in the second band. This selection reduced the oscillations of the electric field within the unit cell and the homogenization process gave the correct result, $\varepsilon_{zz} = 0$. As was mentioned before, the first band has a transversal polarization with the electric field oscillating in the plane of periodicity. As a consequence of the small filling fraction, the electric field does not interact with the metallic wires and the effective permittivity is very close to that of vacuum.

The second important component in this thesis is the study of a two dimensional photonic crystal of cylindrical holes in a silicon matrix and infilled with the nematic liquid crystal 5CB. The analysis shows that in the absence of an external electric field, the NLC molecules within the cylinders adopt the configuration known as *escaped radial.* If an external DC electric field is applied parallel to the cylinders, the nematic molecules gradually change their orientation as the electric field increases in magnitude. Eventually, for a critical value of this DC field, a phase transition occurs to the axial configuration, with all the molecules aligned with the cylinder axis. This critical value was determined as function of the cylinder radius and for radii that are not very small (R ≥ 50 nm), the critical field is $E_c \simeq 14\ V/m$. The knowledge of the direction of the nematic molecules within the cylinder as a function of the radial distance and the applied DC electric field leads to the dielectric tensor ε_{ij} (r) of the NLC cylinder. In turn, this paved the way toward the eigenvalue equation that yields the photonic band structure. Because of the strong anisotropy within the cylinder the eigenvalue equation cannot be split into two equations –one for the E-modes and other for the H-modes– as is usual in ordinary two dimensional photonic crystals. Nevertheless, by analyzing the electric field within the unit cell it was found that each band can be defined as a quasi-E or a quasi-H polarized band. The concept of quasi-polarization was used to develop a simpler method to compute the band structure, resulting in great simplification. The approximation is based on the averaging of the dielectric tensor characterizing the cylinders over the cross-sectional area. As a result, the electromagnetic modes of the PC, in this approximation, are strictly E- or H-polarized. It was found that the photonic bands corresponding to these polarizations very nearly coincide with one of the bands calculated exactly. The results obtained for different values of the external DC electric field show that the optical properties in a photonic crystal of air cylinders in a silicon matrix and infilled with the nematic liquid crystal can be gradually tuned. For example, a quasi-E band gap can be completely closed for a high enough field value.

Finally, the homogenization process and the tuning effect obtained through the inclusion of liquid crystals in the structure of the photonic crystal were used to develop an electro-optic system with potential applications for ray steering, optical multiplexers, logic gates or switches. By employing a two-step homogenization process the refractive angle was calculated for light incident at the system. The first step leads to the effective dielectric constants $\varepsilon_E(q)$ and $\varepsilon_H(q)$ that characterize the NLC cylinders for a given external field E_0. The second step completes the homogenization, representing the entire NLC-infilled PC by an effective index for each polarization. Because of the uniaxial nature of the homogenized medium, the incident electromagnetic wave splits into two beams. The refractive angles of these (ordinary and extraordinary) rays can be continuously varied up to ~ 6% in comparison to the fieldless case (for $\theta_i = 60^o$). The second step of homogenization requires that $\lambda \gg a$, that is, the linear region of the PC's band structure, where $\omega \simeq kc/n_{o,e}(q)$. This implies, typically, the infrared regime. If the PC is placed in a capacitor of width ~ 15 μm, efficient tuning could be achieved with voltages up to about 70 V.

The method described could be used for ray steering, for example employing a PC prism as proposed in ref. [10]. Another potential application is based on a PC lens, as suggested in ref. [139], now with the possibility of tuning the lens's focus. Further applications to be considered are optical multiplexers (where the electromagnetic wave path can be selected by external agents), optical logic gates or optical switches.

The results presented in this thesis could pave the way to the design novel devices to control the flux of light. Moreover, the homogenization theory studied here is a powerful tool for the analysis of metamaterials which are a hot topic in the scientist community.

Appendixes

APPENDIX A: DERIVATION OF EQ. (2.25)

Lets to rewrite the system of equations (2.19) in the form

$$\sum_{\mathbf{G}'} \overleftrightarrow{\mathbf{D}}(\mathbf{k};\mathbf{G},\mathbf{G}') \cdot \mathbf{e}(\mathbf{G}') = 0\,, \qquad \text{A1}$$

where

$$\overleftrightarrow{\mathbf{D}}(\mathbf{k};\mathbf{G},\mathbf{G}') = \left[\left(\left|\mathbf{k}+\mathbf{G}\right|^2 - k_0^2\right)\overleftrightarrow{\mathbf{I}} - \left(\mathbf{k}+\mathbf{G}\right)\left(\mathbf{k}+\mathbf{G}\right)\right]\delta_{\mathbf{G},\mathbf{G}'} - i\omega\mu_0\hat{\sigma}(\mathbf{G}-\mathbf{G}')\overleftrightarrow{\mathbf{I}}\,. \qquad \text{A2}$$

Here, $\mathbf{G}$ and $\mathbf{G}'$ are vectors of the reciprocal lattice, including $\mathbf{G}=0$ and $\mathbf{G}'=0$. It is possible to express $\overleftrightarrow{\mathbf{\Sigma}}(\mathbf{k})$ (Eq. (2.24)) in terms of the matrix $\overleftrightarrow{\mathbf{D}}$. Indeed, as follows from Eq. A2, the Fourier coefficients of the conductivity, $\hat{\sigma}(\mathbf{G})$, are connected to $\overleftrightarrow{\mathbf{D}}$ as

$$\overleftrightarrow{\mathbf{D}}(\mathbf{k};0,0) - \left(k^2 - k_0^2\right)\overleftrightarrow{\mathbf{I}} + \mathbf{k}\mathbf{k} = -i\omega\mu_0\hat{\sigma}(0)\overleftrightarrow{\mathbf{I}}\,, \qquad \text{A3}$$

$$\overleftrightarrow{\mathbf{D}}(\mathbf{k};0,\mathbf{G}') = -i\omega\mu_0\hat{\sigma}(-\mathbf{G}')\overleftrightarrow{\mathbf{I}} \quad \text{for} \quad \mathbf{G}' \neq 0\,, \qquad \text{A4}$$

$$\overleftrightarrow{\mathbf{D}}(\mathbf{k};\mathbf{G},0) = -i\omega\mu_0\hat{\sigma}(\mathbf{G})\overleftrightarrow{\mathbf{I}} \quad \text{for} \quad \mathbf{G} \neq 0\,. \qquad \text{A5}$$

Besides, as it has been recently demonstrated in Ref. [69], there exists a relation between the inverse of a submatrix and the inverse of its original matrix. In the case at hand, $\overleftrightarrow{\mathbf{M}}$ is a submatrix of $\overleftrightarrow{\mathbf{D}}$, with the row $\mathbf{G}=0$ and the column $\mathbf{G}'=0$ having been eliminated. From the aforementioned relation [69] it follows that

$$\overleftrightarrow{\mathbf{M}}^{-1}(\mathbf{k};\mathbf{G},\mathbf{G}') = \overleftrightarrow{\mathbf{D}}^{-1}(\mathbf{k};\mathbf{G},\mathbf{G}') - \overleftrightarrow{\mathbf{D}}^{-1}(\mathbf{k};\mathbf{G},0)\cdot\left\{\overleftrightarrow{\mathbf{D}}^{-1}(\mathbf{k};0,0)\right\}^{-1}\cdot\overleftrightarrow{\mathbf{D}}^{-1}(\mathbf{k};0,\mathbf{G}')\,. \qquad \text{A6}$$

In the above equation, $\overleftrightarrow{\mathbf{D}}^{-1}(\mathbf{k};\mathbf{G},\mathbf{G}')$ is the inverse of the matrix $\overleftrightarrow{\mathbf{D}}(\mathbf{k};\mathbf{G},\mathbf{G}')$ of infinite size, and $\left\{\overleftrightarrow{\mathbf{D}}^{-1}(\mathbf{k};0,0)\right\}^{-1}$ symbolizes the inverse of the 3×3 matrix block $\overleftrightarrow{\mathbf{D}}^{-1}(\mathbf{k};0,0)$.

Now, substituting the Eqs. (A3)-(A6) into Eq. (2.24).

$$\begin{aligned}\overleftrightarrow{\mathbf{\Sigma}}(\mathbf{k}) = \frac{i}{\omega\mu_0}\Bigg\{&\overleftrightarrow{\mathbf{D}}(\mathbf{k};0,0) - \left(k^2-k_0^2\right)\overleftrightarrow{\mathbf{I}} + \mathbf{kk} - {\sum_{\mathbf{G},\mathbf{G}'}}' \overleftrightarrow{\mathbf{D}}(\mathbf{k};0,\mathbf{G})\cdot\Big[\overleftrightarrow{\mathbf{D}}^{-1}(\mathbf{k};\mathbf{G},\mathbf{G}') \\ &-\overleftrightarrow{\mathbf{D}}^{-1}(\mathbf{k};\mathbf{G},0)\cdot\left\{\overleftrightarrow{\mathbf{D}}^{-1}(\mathbf{k};0,0)\right\}^{-1}\cdot\overleftrightarrow{\mathbf{D}}^{-1}(\mathbf{k};0,\mathbf{G}')\Big]\cdot\overleftrightarrow{\mathbf{D}}(\mathbf{k};\mathbf{G}',0)\Bigg\}.\end{aligned} \qquad \text{A7}$$

Then, is replaced $\overleftrightarrow{\mathbf{D}}(\mathbf{k};0,\mathbf{G})$ by $\overleftrightarrow{\mathbf{D}}(\mathbf{k};\mathbf{G}',\mathbf{G})\delta_{\mathbf{G}'0}$ and $\overleftrightarrow{\mathbf{D}}^{-1}(\mathbf{k};\mathbf{G},0)$ by $\overleftrightarrow{\mathbf{D}}^{-1}(\mathbf{k};\mathbf{G},\mathbf{G}')\delta_{\mathbf{G}'0}$, which facilitates the summations over $\mathbf{G}$ and $\mathbf{G}'$. After some algebra is left with the simple result

$$\overleftrightarrow{\boldsymbol{\Sigma}}(\mathbf{k}) = \frac{i}{\omega\mu_0}\left[\left\{\overleftrightarrow{\mathbf{D}}^{-1}(\mathbf{k};0,0)\right\}^{-1} - \left(k^2 - k_0^2\right)\overleftrightarrow{\mathbf{I}} + \mathbf{kk}\right], \tag{A8}$$

which is Eq. (2.25).

APPENDIX B: EXPANSION OF $\overleftrightarrow{\boldsymbol{\Sigma}}(\mathbf{k})$ IN POWERS OF k

Let us rewrite the dyadic $\overleftrightarrow{\mathbf{M}}(\mathbf{k};\mathbf{G},\mathbf{G}')$ (Eq. (2.21)) as

$$\overleftrightarrow{\mathbf{M}}(\mathbf{k};\mathbf{G},\mathbf{G}') = \overleftrightarrow{\mathbf{M}}_0(\mathbf{G},\mathbf{G}') + \overleftrightarrow{\mathbf{M}}_1(\mathbf{G},\mathbf{G}') + \overleftrightarrow{\mathbf{M}}_2(\mathbf{G},\mathbf{G}'), \tag{B1}$$

where

$$\begin{aligned}
\overleftrightarrow{\mathbf{M}}_0(\mathbf{G},\mathbf{G}') &= \left[\left(\mathbf{G}^2 - k_0^2\right)\overleftrightarrow{\mathbf{I}} - \mathbf{GG}\right]\delta_{\mathbf{G},\mathbf{G}'} - i\omega\mu_0\hat{\sigma}(\mathbf{G}-\mathbf{G}')\overleftrightarrow{\mathbf{I}}, \\
\overleftrightarrow{\mathbf{M}}_1(\mathbf{G},\mathbf{G}') &= k\overleftrightarrow{\mathbf{L}}(\hat{\mathbf{k}},\mathbf{G})\delta_{\mathbf{G},\mathbf{G}'}, \\
\overleftrightarrow{\mathbf{M}}_2(\mathbf{G},\mathbf{G}') &= \left[k^2\overleftrightarrow{\mathbf{I}} - \mathbf{kk}\right]\delta_{\mathbf{G},\mathbf{G}'}.
\end{aligned} \tag{B2}$$

Here, $\overleftrightarrow{\mathbf{L}}(\hat{\mathbf{k}},\mathbf{G})$ has been defined in Eq. (2.45). Using these definitions, the inverse of the dyadic $\overleftrightarrow{\mathbf{M}}(\mathbf{k};\mathbf{G},\mathbf{G}')$ can be written in the form:

$$\begin{aligned}
\overleftrightarrow{\mathbf{M}}^{-1}(\mathbf{k},\mathbf{G},\mathbf{G}') = \Big[\overleftrightarrow{\mathbf{I}}\delta_{\mathbf{GG}'''} &+ \overleftrightarrow{\mathbf{M}}_0^{-1}(\mathbf{G},\mathbf{G}'')\cdot\overleftrightarrow{\mathbf{M}}_1(\mathbf{G}'',\mathbf{G}''') \\
&+ \overleftrightarrow{\mathbf{M}}_0^{-1}(\mathbf{G},\mathbf{G}'')\cdot\overleftrightarrow{\mathbf{M}}_2(\mathbf{G}'',\mathbf{G}''')\Big]^{-1}\cdot\overleftrightarrow{\mathbf{M}}_0^{-1}(\mathbf{G}''',\mathbf{G}').
\end{aligned} \tag{B3}$$

Here, was used the identity $\left(\mathbf{AB}\right)^{-1} = \mathbf{B}^{-1}\mathbf{A}^{-1}$ and summation over repeated $\mathbf{G}'$s is implied. The inverse dyadic in Eq. B3 can be expresed in a Taylor expansion as $(\mathbf{I}+\mathbf{A})^{-1} = \mathbf{I} - \mathbf{A} + \mathbf{AA}\cdots$. Then,

$$\begin{aligned}\overleftrightarrow{\mathbf{M}}^{-1}(\mathbf{k},\mathbf{G},\mathbf{G}') \cong{}& \overleftrightarrow{\mathbf{M}}_0^{-1}(\mathbf{G},\mathbf{G}') - \overleftrightarrow{\mathbf{M}}_0^{-1}(\mathbf{G},\mathbf{G}'')\cdot\overleftrightarrow{\mathbf{M}}_1(\mathbf{G}'',\mathbf{G}''')\cdot\overleftrightarrow{\mathbf{M}}_0^{-1}(\mathbf{G}''',\mathbf{G}')\\ &- \overleftrightarrow{\mathbf{M}}_0^{-1}(\mathbf{G},\mathbf{G}'')\cdot\overleftrightarrow{\mathbf{M}}_2(\mathbf{G}'',\mathbf{G}''')\cdot\overleftrightarrow{\mathbf{M}}_0^{-1}(\mathbf{G}''',\mathbf{G}')\\ &+ \overleftrightarrow{\mathbf{M}}_0^{-1}(\mathbf{G},\mathbf{G}'')\cdot\overleftrightarrow{\mathbf{M}}_1(\mathbf{G}'',\mathbf{G}''')\cdot\overleftrightarrow{\mathbf{M}}_0^{-1}(\mathbf{G}''',\mathbf{G}^{IV})\cdot\overleftrightarrow{\mathbf{M}}_1(\mathbf{G}^{IV},\mathbf{G}^{V})\cdot\overleftrightarrow{\mathbf{M}}_0^{-1}(\mathbf{G}^{V},\mathbf{G}').\end{aligned}\tag*{B4}$$

In the above equation has been neglected terms giving contributions of order higher than k^2. The expression just obtained for $\overleftrightarrow{\mathbf{M}}^{-1}(\mathbf{k};\mathbf{G},\mathbf{G}')$ can be verified by calculating $\overleftrightarrow{\mathbf{M}}(\mathbf{k};\mathbf{G},\mathbf{G}')\cdot\overleftrightarrow{\mathbf{M}}^{-1}(\mathbf{k};\mathbf{G},\mathbf{G}')$, which is equal to $\overleftrightarrow{\mathbf{I}}$ up to second order terms. Substituting Eq. B4 into Eq. (2.24) and using the definitions given in Eqs. (2.41) and (2.44)

$$\begin{aligned}\overleftrightarrow{\boldsymbol{\Sigma}}(\mathbf{k}) ={}& \hat{\sigma}(\mathbf{G}=0)\overleftrightarrow{\mathbf{I}} + i\omega\mu_0 {\sum_{\mathbf{G}}}' \hat{\sigma}(\mathbf{G})\overleftrightarrow{\mathbf{C}}_1(\mathbf{G})\\ &- i\omega\mu_0 k {\sum_{\mathbf{G}}}' \overleftrightarrow{\mathbf{C}}_1(\mathbf{G})\cdot\overleftrightarrow{\mathbf{B}}(\hat{\mathbf{k}},\mathbf{G})\cdot\overleftrightarrow{\mathbf{C}}_2(\mathbf{G})\\ &- i\omega\mu_0 k^2 {\sum_{\mathbf{G}}}' \overleftrightarrow{\mathbf{C}}_1(\mathbf{G})\cdot(\overleftrightarrow{\mathbf{I}}-\hat{\mathbf{k}}\hat{\mathbf{k}})\cdot\overleftrightarrow{\mathbf{C}}_2(\mathbf{G})\\ &+ i\omega\mu_0 k^2 {\sum_{\mathbf{G},\mathbf{G}'}}' \overleftrightarrow{\mathbf{C}}_1(\mathbf{G})\cdot\overleftrightarrow{\mathbf{B}}(\hat{\mathbf{k}},\mathbf{G})\cdot\overleftrightarrow{\mathbf{M}}_0^{-1}(\mathbf{G},\mathbf{G}')\cdot\overleftrightarrow{\mathbf{B}}(\hat{\mathbf{k}},\mathbf{G}')\cdot\overleftrightarrow{\mathbf{C}}_2(\mathbf{G}').\end{aligned}\tag*{B5}$$

From Eq. B5 is clear that the effective conductivity can be written as $\overleftrightarrow{\boldsymbol{\Sigma}}(\mathbf{k}) = \overleftrightarrow{\boldsymbol{\Sigma}}_0 + k\overleftrightarrow{\boldsymbol{\Sigma}}_1(\hat{\mathbf{k}}) + k^2\overleftrightarrow{\boldsymbol{\Sigma}}_2(\hat{\mathbf{k}})$, namely Eq. (2.37) with $\overleftrightarrow{\boldsymbol{\Sigma}}_0$, $\overleftrightarrow{\boldsymbol{\Sigma}}_1(\hat{\mathbf{k}})$, and $\overleftrightarrow{\boldsymbol{\Sigma}}_2(\hat{\mathbf{k}})$ defined by Eqs. (2.40), (2.44), and (2.47), respectively.

APPENDIX C: DETERMINATION OF $p = 1/2$ BY IMPOSING THE ONSAGER SYMMETRY RELATIONS

From the definition of the inverse of a matrix is obtained the following three relations:

$$\sum_{\mathbf{G}'}{}^{'} \overleftrightarrow{\mathbf{M}}_0(\mathbf{G},\mathbf{G}') \cdot \overleftrightarrow{\mathbf{M}}_0^{-1}(\mathbf{G}',\mathbf{G}'') = \overleftrightarrow{\mathbf{I}}\delta_{\mathbf{G},\mathbf{G}''}, \qquad \text{C1}$$

$$\sum_{\mathbf{G}'}{}^{'} \overleftrightarrow{\mathbf{M}}_0(-\mathbf{G},\mathbf{G}') \cdot \overleftrightarrow{\mathbf{M}}_0^{-1}(\mathbf{G}',-\mathbf{G}'') = \overleftrightarrow{\mathbf{I}}\delta_{\mathbf{G},\mathbf{G}''}, \qquad \text{C2}$$

$$\sum_{\mathbf{G}'}{}^{'} \overleftrightarrow{\mathbf{M}}_0(-\mathbf{G},-\mathbf{G}') \cdot \overleftrightarrow{\mathbf{M}}_0^{-1}(-\mathbf{G}',-\mathbf{G}'') = \overleftrightarrow{\mathbf{I}}\delta_{\mathbf{G},\mathbf{G}''}. \qquad \text{C3}$$

Besides, from Eq. (2.42) it is possible to see that $\overleftrightarrow{\mathbf{M}}_0(-\mathbf{G},-\mathbf{G}') = \overleftrightarrow{\mathbf{M}}_0(\mathbf{G}',\mathbf{G})$ and $M_{0ij}(\mathbf{G},\mathbf{G}') = M_{0ji}(\mathbf{G},\mathbf{G}')$. Using these relations and Eq. C3,

$$\sum_{\mathbf{G}'}{}^{'} M_{0jk}^{-1}(-\mathbf{G}',-\mathbf{G}'')M_{0ji}(\mathbf{G}',\mathbf{G}) = \delta_{ik}\delta_{\mathbf{G},\mathbf{G}''}. \qquad \text{C4}$$

The last equation implies that

$$M_{0jk}^{-1}(-\mathbf{G}',-\mathbf{G}'') = M_{0kj}^{-1}(\mathbf{G}'',\mathbf{G}'). \qquad \text{C5}$$

Now, using the above derived properties of symmetry for $\overleftrightarrow{\mathbf{M}}_0^{-1}(\mathbf{G}',\mathbf{G}'')$, it is possible to straightforwardly obtain

$$\overleftrightarrow{\mathbf{\Sigma}}_0 = \overleftrightarrow{\mathbf{\Sigma}}_0^T, \quad \overleftrightarrow{\mathbf{\Sigma}}_1 = -\overleftrightarrow{\mathbf{\Sigma}}_1^T, \quad \overleftrightarrow{\mathbf{\Sigma}}_2 = \overleftrightarrow{\mathbf{\Sigma}}_2^T, \qquad \text{C6}$$

and consequently

$$\overleftrightarrow{\boldsymbol{\alpha}} = \overleftrightarrow{\boldsymbol{\alpha}}^T, \quad \overleftrightarrow{\boldsymbol{\beta}} = \overleftrightarrow{\boldsymbol{\varphi}}^T \frac{(1-p)}{p}, \quad \overleftrightarrow{\boldsymbol{\psi}} = \overleftrightarrow{\boldsymbol{\psi}}^T. \qquad \text{C7}$$

The Onsager symmetry relations impose that

$$\overleftrightarrow{\boldsymbol{\delta}} = -\overleftrightarrow{\boldsymbol{\gamma}}^T, \qquad \text{C8}$$

where the dyadics $\overleftrightarrow{\boldsymbol{\delta}}$ and $\overleftrightarrow{\boldsymbol{\gamma}}$ are given by Eq. (2.63). Substituting the Eq. C7 into Eq. (2.63) and, in turn, in Eq. C8, is obtained that $p = 1/2$.

APPENDIX D: PROOF OF EQ. (2.81)

The calculation of the matrix block $\overleftrightarrow{\mathbf{N}}^{-1}(\mathbf{k}=0;0,0)$ is equivalent to solving the system of equations

$$\sum_{\mathbf{G}'} \left\{ \left[\left(G^2 - k_0^2\right) \overleftrightarrow{\mathbf{I}} - \mathbf{G}\mathbf{G} \right] \delta_{\mathbf{G},\mathbf{G}'} - i\omega\mu_0 \hat{\sigma}(\mathbf{G}-\mathbf{G}') \overleftrightarrow{\mathbf{I}} \right\} \cdot \overleftrightarrow{\mathbf{N}}^{-1}(\mathbf{k}=0;\mathbf{G}',0) = \delta_{\mathbf{G},0} \overleftrightarrow{\mathbf{I}}. \qquad \text{D1}$$

Using the transverse and longitudinal projection operators, $\overleftrightarrow{\mathbf{P}}_T$ and $\overleftrightarrow{\mathbf{P}}_L$, this equation can be rewritten as

$$\begin{aligned}&\left[\left(G^2-k_0^2\right)\overleftrightarrow{\mathbf{P}}_T\left(\mathbf{G}\right)-k_0^2\overleftrightarrow{\mathbf{P}}_L\left(\mathbf{G}\right)\right]\cdot\overleftrightarrow{\mathbf{N}}^{-1}(\mathbf{k}=0;\mathbf{G},0)\\&\qquad-i\omega\mu_0\sum_{\mathbf{G}'}\hat{\sigma}(\mathbf{G}-\mathbf{G}')\overleftrightarrow{\mathbf{N}}^{-1}(\mathbf{k}=0;\mathbf{G}',0)=\delta_{\mathbf{G},0}\overleftrightarrow{\mathbf{I}},\end{aligned}\qquad \text{D2}$$

where $\overleftrightarrow{\mathbf{I}}=\overleftrightarrow{\mathbf{P}}_T(\mathbf{G})+\overleftrightarrow{\mathbf{P}}_L(\mathbf{G})$, $\overleftrightarrow{\mathbf{P}}_T(\mathbf{G})=\overleftrightarrow{\mathbf{I}}-\hat{\mathbf{G}}\hat{\mathbf{G}}$ and $\mathbf{P}_L(\mathbf{G})=\hat{\mathbf{G}}\hat{\mathbf{G}}$. Now, the Fourier coefficients can be written as follows:

$$\hat{\sigma}(\mathbf{G}-\mathbf{G}')=\hat{\sigma}_b\delta_{\mathbf{G},\mathbf{G}'}+\Delta\hat{\sigma}F(\mathbf{G}-\mathbf{G}'),\qquad \text{D3}$$

where $\Delta\hat{\sigma}=\hat{\sigma}_a-\hat{\sigma}_b$ and $F(\mathbf{G}-\mathbf{G}')$ is the inclusion form factor. Substituting Eq. D3 into Eq. D2, then

$$\begin{aligned}&\left[\left(G^2-k_0^2-i\omega\mu_0\hat{\sigma}_b\right)\overleftrightarrow{\mathbf{P}}_T\left(\mathbf{G}\right)-\left(k_0^2+i\omega\mu_0\hat{\sigma}_b\right)\overleftrightarrow{\mathbf{P}}_L\left(\mathbf{G}\right)\right]\cdot\overleftrightarrow{\mathbf{N}}^{-1}(\mathbf{k}=0;\mathbf{G}',0)\\&\qquad-i\omega\mu_0\sum_{\mathbf{G}'}\Delta\hat{\sigma}F(\mathbf{G}-\mathbf{G}')\overleftrightarrow{\mathbf{N}}^{-1}(\mathbf{k}=0;\mathbf{G}',0)=\delta_{\mathbf{G},0}\overleftrightarrow{\mathbf{I}}.\end{aligned}$$

D4

This equation can be rewritten as

$$\overleftrightarrow{\mathbf{N}}^{-1}(\mathbf{k}=0;\mathbf{G},0)-i\omega\mu_0\Delta\hat{\sigma}\overleftrightarrow{\mathbf{O}}(\mathbf{G})\sum_{\mathbf{G}'}F(\mathbf{G}-\mathbf{G}')\overleftrightarrow{\mathbf{N}}^{-1}(\mathbf{k}=0;\mathbf{G}',0)=\overleftrightarrow{\mathbf{O}}\delta_{\mathbf{G},0},\qquad \text{(D5)}$$

where we have introduced the matrix $\overleftrightarrow{\mathbf{O}}(\mathbf{G})$:

$$\overleftrightarrow{\mathbf{O}}(\mathbf{G})=\left[\frac{\overleftrightarrow{\mathbf{P}}_T(\mathbf{G})}{G^2-k_0^2-i\omega\mu_0\hat{\sigma}_b}-\frac{\overleftrightarrow{\mathbf{P}}_L(\mathbf{G})}{k_0^2+i\omega\mu_0\hat{\sigma}_b}\right].\qquad \text{(D6)}$$

From Eq. (D5), it follows that $\overleftrightarrow{\mathbf{N}}^{-1}(\mathbf{k}=0;0,0)$ is related with the sum

$$\overleftrightarrow{\mathbf{C}}_0 = \sum_{\mathbf{G}'} F(-\mathbf{G}')\overleftrightarrow{\mathbf{N}}^{-1}(\mathbf{k}=0;\mathbf{G}',0)\,, \tag{D7}$$

according to:

$$\overleftrightarrow{\mathbf{N}}^{-1}(\mathbf{k}=0;0,0) - i\omega\mu_0\Delta\hat{\sigma}\overleftrightarrow{\mathbf{O}}(0)\sum_{\mathbf{G}'} F(-\mathbf{G}')\overleftrightarrow{\mathbf{N}}^{-1}(\mathbf{k}=0;\mathbf{G}',0) = \overleftrightarrow{\mathbf{O}}(0)\,. \tag{D8}$$

Multiplying Eq. (D5) by $F(-\mathbf{G})$ and summing both sides over $\mathbf{G}$, we also find

$$\begin{aligned}&\sum_{\mathbf{G}'} F(-\mathbf{G})\overleftrightarrow{\mathbf{N}}^{-1}(\mathbf{k}=0;\mathbf{G},0)\\ &\qquad - i\omega\mu_0\Delta\hat{\sigma}\sum_{\mathbf{G},\mathbf{G}'} F(-\mathbf{G})\overleftrightarrow{\mathbf{O}}(\mathbf{G})F(\mathbf{G}-\mathbf{G}')\overleftrightarrow{\mathbf{N}}^{-1}(\mathbf{k}=0;\mathbf{G}',0) = F(0)\overleftrightarrow{\mathbf{O}}(0)\end{aligned}\,. \tag{D9}$$

If we consider small inclusions $(f << 1)$, then $F(\mathbf{G}-\mathbf{G}')$ is a function which slowly varies with the magnitude of $\mathbf{G}-\mathbf{G}'$. Hence for $G << 1/r$, where r is the characteristic size of the inclusion, we can use the following approximation

$$F(\mathbf{G}-\mathbf{G}') \approx F(0-\mathbf{G}') \approx F(-\mathbf{G}')\,. \tag{D10}$$

This approximation is good enough to solve Eq. (D9) because the dyadic $F(-\mathbf{G})\overleftrightarrow{\mathbf{O}}(\mathbf{G})$ decreases with G (see Eq. (D6)) and practically vanishes at $Gr >> 1$. Then, employing (D7), (D9), and (D10), we get

$$\overleftrightarrow{\mathbf{C}}_0 - i\omega\mu_0\sum_{\mathbf{G}} F(-\mathbf{G})\overleftrightarrow{\mathbf{O}}(\mathbf{G})\Delta\hat{\sigma}\overleftrightarrow{\mathbf{C}}_0 = \overleftrightarrow{\mathbf{O}}(0)F(0) \tag{D11}$$

The solution of this equation can be written as

$$\overleftrightarrow{\mathbf{C}}_0 = \left[\overleftrightarrow{\mathbf{I}} - i\omega\mu_0\Delta\hat{\sigma}\sum_{\mathbf{G}} F(-\mathbf{G})\overleftrightarrow{\mathbf{O}}(\mathbf{G})\right]^{-1} \cdot \overleftrightarrow{\mathbf{O}}(0)F(0)\,, \tag{D12}$$

which requires the calculation of the sum

$$\sum_{\mathbf{G}} F(-\mathbf{G}')\overleftrightarrow{\mathbf{O}}(\mathbf{G}) = \sum_{\mathbf{G}} F(-\mathbf{G})\left[\frac{\overleftrightarrow{\mathbf{I}} - \left(\mathbf{GG}/G^2\right)}{G^2 - k_0^2 - i\omega\mu_0\hat{\sigma}_b} - \frac{\left(\mathbf{GG}/G^2\right)}{k_0^2 + i\omega\mu_0\hat{\sigma}_b}\right]. \tag{D13}$$

Since our formulas are being derived in the limit $k \to 0$, the term with $\mathbf{G} = 0$ in (D13) turns out to be equal to $-F(0)\overleftrightarrow{\mathbf{I}}/(k_0^2 + i\omega\mu_0\hat{\sigma}_b)$.

In the long wavelength limit, i.e. when $G/k_0 >> 1$ the sum (D13) can be simplified. Indeed, let us rewrite it as

$$\begin{aligned}\sum_{\mathbf{G}} F(-\mathbf{G})\overleftrightarrow{\mathbf{O}}(\mathbf{G}) = -\frac{F(0)\overleftrightarrow{\mathbf{I}}}{k_0^2 + i\omega\mu_0\hat{\sigma}_b} &+ \sum_{\mathbf{G}'\neq 0} \frac{F(-G)(\overleftrightarrow{\mathbf{I}} - \mathbf{GG}/G^2)}{G^2 - k_0^2 - i\omega\mu_0\hat{\sigma}_b} \\ &- \sum_{\mathbf{G}'\neq 0} \frac{F(-G)\,\mathbf{GG}/G^2}{k_0^2 + i\omega\mu_0\hat{\sigma}_b}\end{aligned} \tag{D14}$$

The second term on the right-hand side of Eq. (D14) is much smaller than the others as $\left|k_0^2 + i\omega\mu_0\hat{\sigma}_b\right| << G^2$. If the latter inequality is satisfied, we can write

$$\sum_{\mathbf{G}} F(-\mathbf{G})\overleftrightarrow{\mathbf{O}}(\mathbf{G}) \approx -\frac{F(0)\overleftrightarrow{\mathbf{I}}}{k_0^2 + i\omega\mu_0\hat{\sigma}_b} - \sum_{\mathbf{G}'\neq 0} \frac{F(-G)\,\mathbf{GG}/G^2}{k_0^2 + i\omega\mu_0\hat{\sigma}_b} \tag{D15}$$

Now, we should use the sum rules:

$$\sum_{\mathbf{G}\neq 0} F(-\mathbf{G}) = 1 - F(0)\,, \tag{D16}$$

and, for a cubic system,

$$\sum_{\mathbf{G}\neq 0} \frac{\mathbf{G}\mathbf{G}}{G^2} F(-G) = \overleftrightarrow{\mathbf{I}}\,\frac{1}{3}\sum_{\mathbf{G}\neq 0} F(-\mathbf{G}') = \frac{1-F(0)}{3}\overleftrightarrow{\mathbf{I}}\,. \tag{D17}$$

Substituting (D17) into Eq. (D15), we finally get

$$\sum_{\mathbf{G}} F(-\mathbf{G}')\overleftrightarrow{\mathbf{O}}(\mathbf{G}) \cong \overleftrightarrow{\mathbf{I}}\left\{\frac{\tfrac{2}{3}F(0)}{-k_0^2 - i\omega\mu_0\hat{\sigma}_b} - \frac{1}{3}\frac{1}{k_0^2 + i\omega\mu_0\hat{\sigma}_b}\right\}. \tag{D18}$$

Using Eq. (D18), the expression for $\overleftrightarrow{\mathbf{C}}_0$ acquires the form

$$\overleftrightarrow{\mathbf{C}}_0 = \left[1 - i\omega\mu_0\Delta\hat{\sigma}\left\{\frac{\tfrac{2}{3}f}{-k_0^2 - i\omega\mu_0\hat{\sigma}_b} - \frac{1}{3}\frac{1}{k_0^2 + i\omega\mu_0\hat{\sigma}_b}\right\}\right]^{-1}\left[\frac{\overleftrightarrow{\mathbf{I}}}{-k_0^2 - i\omega\mu_0\hat{\sigma}_b}\right] f\,, \tag{D19}$$

where $f = F(0)$. Simplifying,

$$\overleftrightarrow{\mathbf{C}}_0 = -\frac{f\,\overleftrightarrow{\mathbf{I}}}{k_0^2 + i\omega\mu_0\left[\left(\hat{\sigma}_a - \hat{\sigma}_b\right)\left(\tfrac{2}{3}f + \tfrac{1}{3}\right) + \hat{\sigma}_b\right]}\,. \tag{D20}$$

Finally, we substitute this result for $\overset{\leftrightarrow}{\mathbf{C}}_0$ in Eq. (D8) and obtain

$$\overset{\leftrightarrow}{\mathbf{N}}^{-1}(\mathbf{k}=0;0,0) = -\frac{1}{k_0^2 + i\omega\mu_0\hat{\sigma}_b}\left(1 - \frac{i\omega\mu_0\left(\hat{\sigma}_a - \hat{\sigma}_b\right)f}{k_0^2 + i\omega\mu_0\left[\left(\hat{\sigma}_a - \hat{\sigma}_b\right)\left(\frac{2}{3}f + \frac{1}{3}\right) + \hat{\sigma}_b\right]}\right)\overset{\leftrightarrow}{\mathbf{I}} \,. \tag{D21}$$

This is the desired result, Eq. (81).

APPENDIX E: PROOF OF EQ. (2.84)

Consider a plane wave with $\mathbf{k} = k_x\hat{\mathbf{x}}$ and $\mathbf{E} = E_z\hat{\mathbf{z}}$ traveling through a PC constructed with thin metallic wires that are parallel to the x, y, z coordinate axes ("3D crosses"). In this case, the "active wires" are those parallel to $\hat{\mathbf{z}}$ direction and the contribution of the wires parallel to $\hat{\mathbf{x}}$ and $\hat{\mathbf{y}}$ directions to the effective response can be neglected. This situation is equivalent to the calculation of the effective permittivity ε_{zz} of a 2D PC of thin metallic wires. By the way, in such a 2D PC we can observe that the contribution of thin wires, parallel to the *z* direction, to the effective permittivity $\varepsilon_{\perp}$ is indeed negligible (see Fig. 2.5 and Refs. 26 and 65). Then $\mathbf{G}(G_x, G_x, 0) = \mathbf{G}(G_{\perp}, 0)$ and

$$\hat{\sigma}(\mathbf{G}-\mathbf{G}') = \hat{\sigma}_a F(\mathbf{G}-\mathbf{G}') = \sigma F(\mathbf{G}-\mathbf{G}') \,, \tag{E1}$$

where σ is the usual conductivity, $F(\mathbf{G}-\mathbf{G}')=\frac{1}{A_{cu}}\int\limits_{a} e^{-i(\mathbf{G}-\mathbf{G}')\cdot r}d\mathbf{r}$ is the inclusion form factor and vacuum has been considered as the host medium. To obtain ε_{zz}, we derive from Eq. D1:

$$\overleftrightarrow{\mathbf{N}}_{zz}^{-1}(\mathbf{k}=0;\mathbf{G}_{\perp},0)-\frac{i\omega\mu_0\sigma}{G_{\perp}^2-k_0^2}\sum_{\mathbf{G}'_{\perp}}F(\mathbf{G}_{\perp}-\mathbf{G}'_{\perp})\overleftrightarrow{\mathbf{N}}_{zz}^{-1}(\mathbf{k}=0;\mathbf{G}'_{\perp},0)=-\frac{\delta_{\mathbf{G},0}}{k_0^2}\,. \tag{E2}$$

Since the wire are assumed to be very thin, we can use the same approach as in Eq. (D10) and rewrite Eq. (E2) as

$$\overleftrightarrow{\mathbf{N}}_{zz}^{-1}(\mathbf{k}=0;\mathbf{G}_{\perp},0)-\frac{i\omega\mu_0\sigma}{G_{\perp}^2-k_0^2}C=-\frac{\delta_{\mathbf{G},0}}{k_0^2}\,, \tag{E3}$$

where

$$C=\sum_{\mathbf{G}'_{\perp}}F(-\mathbf{G}'_{\perp})\overleftrightarrow{\mathbf{N}}_{zz}^{-1}(\mathbf{k}=0;\mathbf{G}'_{\perp},0)\,. \tag{E4}$$

Using the last equation, we obtain from Eq. (E3):

$$C-i\omega\mu_0\sigma\sum_{\mathbf{G}_{\perp}}\frac{F(-\mathbf{G}_{\perp})}{G_{\perp}^2-k_0^2}C=-\frac{F(0)}{k_0^2}\,. \tag{E5}$$

In the long wavelength limit, i.e. when $G_{\perp}\gg k_0$, Eq. (E5) is rewritten in the form

$$C=\left[1+\frac{i\omega\mu_0\sigma F(0)}{k_0^2}-i\omega\mu_0\sigma\sum_{\mathbf{G}'_{\perp}\neq 0}\frac{F(-\mathbf{G}'_{\perp})}{\mathbf{G}_{\perp}^2}\right]^{-1}\left(-\frac{F(0)}{k_0^2}\right). \tag{E6}$$

Substituting Eq. (E6) into Eq. (E3), we get

$$\overleftrightarrow{\mathbf{N}}_{zz}^{-1}(\mathbf{k}=0;0,0) = -\frac{1}{k_0^2} + \frac{i\omega\mu_0\sigma}{k_0^2}\frac{F(0)}{k_0^2\left[1+\frac{i\omega\mu_0\sigma F(0)}{k_0^2} - i\omega\mu_0\sigma\sum\limits_{\mathbf{G}'_\perp\neq 0}\frac{F(-\mathbf{G}'_\perp)}{\mathbf{G}_\perp^2}\right]}. \quad \text{(E7)}$$

After some algebraic manipulation, we obtain

$$\left\{\overleftrightarrow{\mathbf{N}}_{zz}^{-1}(0,0)\right\}^{-1} = 1 - \frac{i\omega\mu_0\sigma k_0^2 F(0)}{k_0^2 - i\omega\mu_0\sigma k_0^2 \sum\limits_{\mathbf{G}_\perp\neq 0} F(-\mathbf{G}_\perp)\big/G_\perp^2}. \quad \text{(E8)}$$

Substituting Eq. (E8) into Eq. (43) we find that

$$\varepsilon_{eff} = \varepsilon_0\left[1 - \frac{\mu_0\sigma c^2 F(0)}{i\omega + \mu_0\sigma\omega^2\sum\limits_{\mathbf{G}_\perp\neq 0}\frac{F(-\mathbf{G}_\perp)}{G_\perp^2}}\right]. \quad \text{(E9)}$$

If we consider wires of circular cross section, then

$$\sum_{\mathbf{G}_\perp\neq 0}\frac{F(-\mathbf{G}_\perp)}{G_\perp^2} = 2f\sum_{\mathbf{G}_\perp\neq 0}\frac{J_1(G_\perp r_0)}{G_\perp^3 r_0}, \quad \text{(E10)}$$

where $f = \pi r_0^2/a^2$ is the filling fraction and $J_1(G_\perp r_0)$ are the first order Bessel function. Considering that the function $J_1(G_\perp r_0)/G_\perp r_0$ is a smooth function at $G_\perp r_0 < 1$ and rapidly decreases at $G_\perp r_0 > 1$, we shall neglect the contribution of vectors with $G_\perp r_0 > 1$ in Eq. (E10). Besides, the function $J_1(G_\perp r_0)/G_\perp r_0$ will be approximated by the value of $1/2$ at $G_\perp r_0 < 1$. Then,

$$\sum_{\mathbf{G}_\perp \neq 0} \frac{F(-\mathbf{G}_\perp)}{G_\perp^2} \approx f \sum_{G_\perp \neq 0, G_\perp \leq 1/r_0} \frac{1}{G_\perp^2} \approx \frac{f}{(2\pi/a)^2} \int_0^{2\pi} d\varphi \int_1^{a/2\pi r_0} \frac{g dg}{g^2} = \\ = \frac{fa^2}{2\pi} \ln\left(\frac{a}{2\pi r_0} \right) \approx \frac{fa^2}{2\pi} \ln\left(\frac{a}{r_0} \right), \tag{E11}$$

where $g = G_\perp a/2\pi$. Notice that the latter approximation in Eq. (E11) is valid because of the assumption $(a/r_0) >> 1$ and, then, $\ln(a/r_0) >> \ln(2\pi)$. It means that the result (E11) is not significantly altered by the choice of the cut-off value $(\sim 1/r_0)$ for the sum over $\mathbf{G}_\perp$.

Finally, substituting Eq. (E11) into Eq. (E9) we get that

$$\varepsilon_{eff} = \varepsilon_0 \left(1 - \frac{\frac{2\pi}{a^2} \frac{c^2}{\ln(a/r_0)}}{\omega^2 + i \frac{\omega \varepsilon_0 c^2 2\pi}{\sigma f a^2 \ln(a/r_0)}} \right) \tag{E12}$$

which is the Eq. (84). In a similar way, the corresponding expression for wires with square cross-section is obtained as

$$\varepsilon_{eff} = \varepsilon_0 \left(1 - \frac{\frac{2\pi}{a^2} \frac{c^2}{\ln(a/l)}}{\omega^2 + i \frac{\omega \varepsilon_0 c^2 2\pi}{\sigma f a^2 \ln(a/l)}} \right), \tag{E13}$$

where l is the side size of the square and $f = l^2/a^2$.

APPENDIX F: ANALYSIS OF IN-PLANE CONVERGENCE

Here, is given a brief analysis of convergence of some figures presented in chapter 2. As a first system, consider a PC of Si-cylinders in a square lattice as in Fig. 2.1. Figure F1 presents the corresponding principal dielectric constants as a function of the number of **G** values used in the computation for three different filling fractions. Our method reaches convergence using around 600, 1000 and 1400 **G** values for $f_a = 0.1$, $f_a = 0.4$ and $f_a = 0.7$ respectively. For high filling fractions, more plane waves are needed in the Fourier series in order to describe the periodic structure.

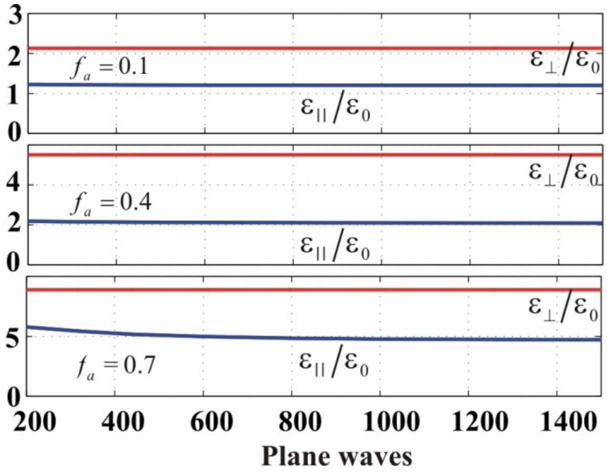

Fig. F.1. Principal dielectric constants of a PC made of Si-cylinders in a square lattice as a function of the number of **G** values used in the computation. Three values of the filling fraction are considered. The system corresponds to that in Fig. 2.1. Very good convergence is attained with about 1000 **G** values.

Comparing our theory with the method proposed in Ref. 10 where $\mu = \mu_0$ is assumed and convergence is achieved employing 1028 **G** values, our computations require more plane waves, but in contrast, our method is not restricted to the dielectric case and also gives the effective permeability of the system. Similar behavior is observed in Fig. F2 where we have plotted the effective permittivity as a function of the number of **G** values used in the computation for a system of dielectric spheres in a cubic lattice (as in Fig. 2.2) for $f_a = 0.1$, $f_a = 0.4$ and $f_a = 0.7$. In this case our method reaches convergence using around 700, 1000 and 1200 G values respectively. Finally, in Fig. F.3 we have plotted the effective permeability of a square lattice of copper wires as a function of the filling fraction for the H-mode, as in Fig. 2.4. This time, we have included the results obtained by using 613, 797, 1009 and 1405 **G** values.

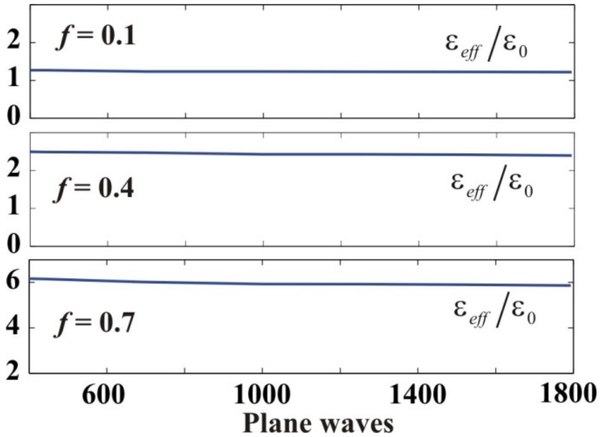

Fig. F.2. Effective permittivity as a function of the number of **G** values used in the computation for a system of dielectric spheres in a cubic lattice, as in Fig. 2.2. Three values of the filling fraction are presented. In all cases, our theory reaches convergence. With 1000 plane waves the convergence error is $\approx 1\%$.

The figure shows that for small filling fractions ($f < 0.6$) our theory gives the same result as in Ref. 26 even using only 613 **G** values. As before, in order to get convergence for high filling fractions, the number of plane waves must be increased with the filling fraction, resulting in higher computation time. For $f > 0.65$ the behavior becomes strongly divergent – even when 1405 plane waves are employed.

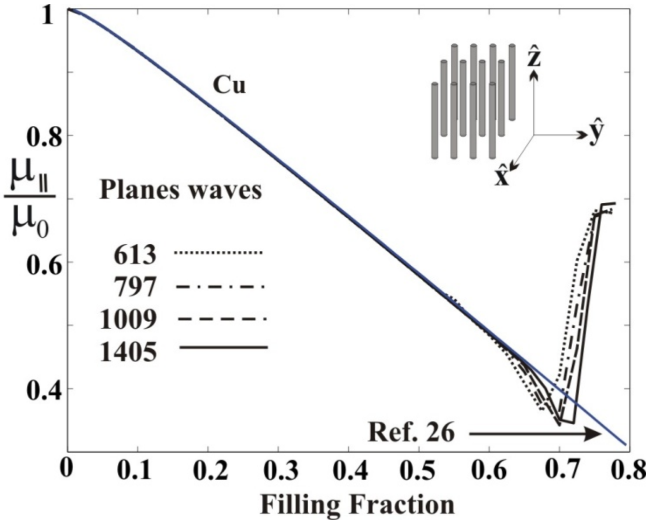

Fig. F.3. Effective permeability of a square lattice of copper wires as a function of the filling fraction for the H-mode, as in Fig. 2.4. We have plotted the results obtained from Eq. 2.67 by using 613, 797, 1009 and 1405 **G** values. Our theory gives practically the same result as Ref. 26 for $f < 0.6$, but for higher filling fractions it is necessary to increase the number of **G** values in order to reach convergence.

Appendix G. Band structure computation for the axial propagation

In order to obtain $\omega(k)$ for dielectric and metallo-dielectric structures, the PC can been described using a periodic dielectric function with the form:

$$\varepsilon(\mathbf{r}) = \tilde{\varepsilon}(\mathbf{r})\left[1-\omega_p(\mathbf{r})^2 / c^2\right] \qquad \text{G1}$$

where a dielectric component is characterized by $\omega_p = 0$ and $\tilde{\varepsilon}$ being their dielectric permittivity. On the other hand, a metallic component is characterized by $\tilde{\varepsilon} = 1$ and ω_p being their corresponding plasma frequency. Here, the absorption has been neglected. Using Eq. G1 it is possible to obtain the following standard eigenvalue problem [142]:

$$\sum_{\mathbf{G}'}\eta(\mathbf{G}-\mathbf{G}')\begin{bmatrix} \left(k_{By}+G'_y\right)^2+k_z^2+\dfrac{\Omega(\mathbf{G}-\mathbf{G}')}{\eta(\mathbf{G}-\mathbf{G}')} & -\left(k_{Bx}+G'_x\right)\left(k_{By}+G'_y\right) & -\left(k_{Bx}+G'_x\right)k_z \\ -\left(k_{Bx}+G'_x\right)\left(k_{By}+G'_y\right) & \left(k_{Bx}+G'_x\right)^2+k_z^2+\dfrac{\Omega(\mathbf{G}-\mathbf{G}')}{\eta(\mathbf{G}-\mathbf{G}')} & -\left(k_{By}+G'_y\right)k_z \\ -\left(k_{Bx}+G'_x\right)k_z & -\left(k_{By}+G'_y\right)k_z & \left(k_{Bx}+G'_x\right)^2+\left(k_{By}+G'_y\right)^2+\dfrac{\Omega(\mathbf{G}-\mathbf{G}')}{\eta(\mathbf{G}-\mathbf{G}')} \end{bmatrix}\begin{bmatrix} E_x(\mathbf{G}') \\ E_y(\mathbf{G}') \\ E_z(\mathbf{G}') \end{bmatrix}=\left(\frac{\omega}{c}\right)^2\begin{bmatrix} E_x(\mathbf{G}) \\ E_y(\mathbf{G}) \\ E_z(\mathbf{G}) \end{bmatrix} \tag{G2}$$

where $\eta(\mathbf{G}-\mathbf{G}')$ and $\Omega(\mathbf{G}-\mathbf{G}')$ are given by

$$\eta(\mathbf{G})=\frac{1}{A_{cu}}\int_{cu}\frac{1}{\tilde{\varepsilon}(\mathbf{r})}e^{-i\mathbf{G}\cdot\mathbf{r}}d\mathbf{r};\quad \Omega(\mathbf{G})=\frac{1}{A_{cu}}\int_{cu}\omega_p(\mathbf{r})e^{-i\mathbf{G}\cdot\mathbf{r}}d\mathbf{r}. \tag{G3}$$

It is important to note here, that for $k_z=0$, Eq. G2 can be split in two equations: one for the E-modes with its electric field oscillating perpendicular to the plane of periodicity and one for the H-modes with its electric field oscillating parallel to the plane of periodicity [142].

An especial situation is observed when the Eq. G2 is solved for a system of metallic wires. As was pointed out by Kuzmiak et al [143], the photonic band structure obtained from Eq. G2 shows a large number of flat bands (dispersionless) in addition to the conventional dispersion bands. These flat bands occur when the electric field of the electromagnetic wave is oscillating perpendicular to the wires and are found in the frequency range $\omega_p / \sqrt{2} < \omega < \omega_p$. Then, for in plane propagation, this phenomenon only occurs for the H polarization. The origin of these flat bands can be understood as the H polarized excitations associated with each metallic wire in isolation and characterized by discrete frequency. When a photonic crystal in formed by bringing together an infinite number of metallic wires, the individual excitations overlap and form narrow bands. Unfortunately, these flat bands converge very slowly with the increase of the number of G vectors used to solve equation G2 and the method proposed by Kuzmiak [143] cannot be employed for the case of axial propagation. Although the FDTD method can be used to compute the dispersion of this kind of systems [83], is still possible to obtain it trough Eq. G2 by eliminating at hand the flat bands which converge very slowly. Figures G.1 and G.2 shows the results obtained from Eq. G2 for a square lattice of aluminum- and copper-wires respectively. The solid lines correspond to the first two bands obtained by using 1009 plane waves in the computation.

The figures show how the flat bands do not reach convergence even using 1009 plane waves in the computation. In contrast, for wave vectors smaller than 0.2, the first two band converge with only 441 plane waves. Then, making a careful selection of the first band it is possible to obtain the dispersion relation. Here is important to say that in some cases result impossible to do the selection because of the huge number of flat bands.

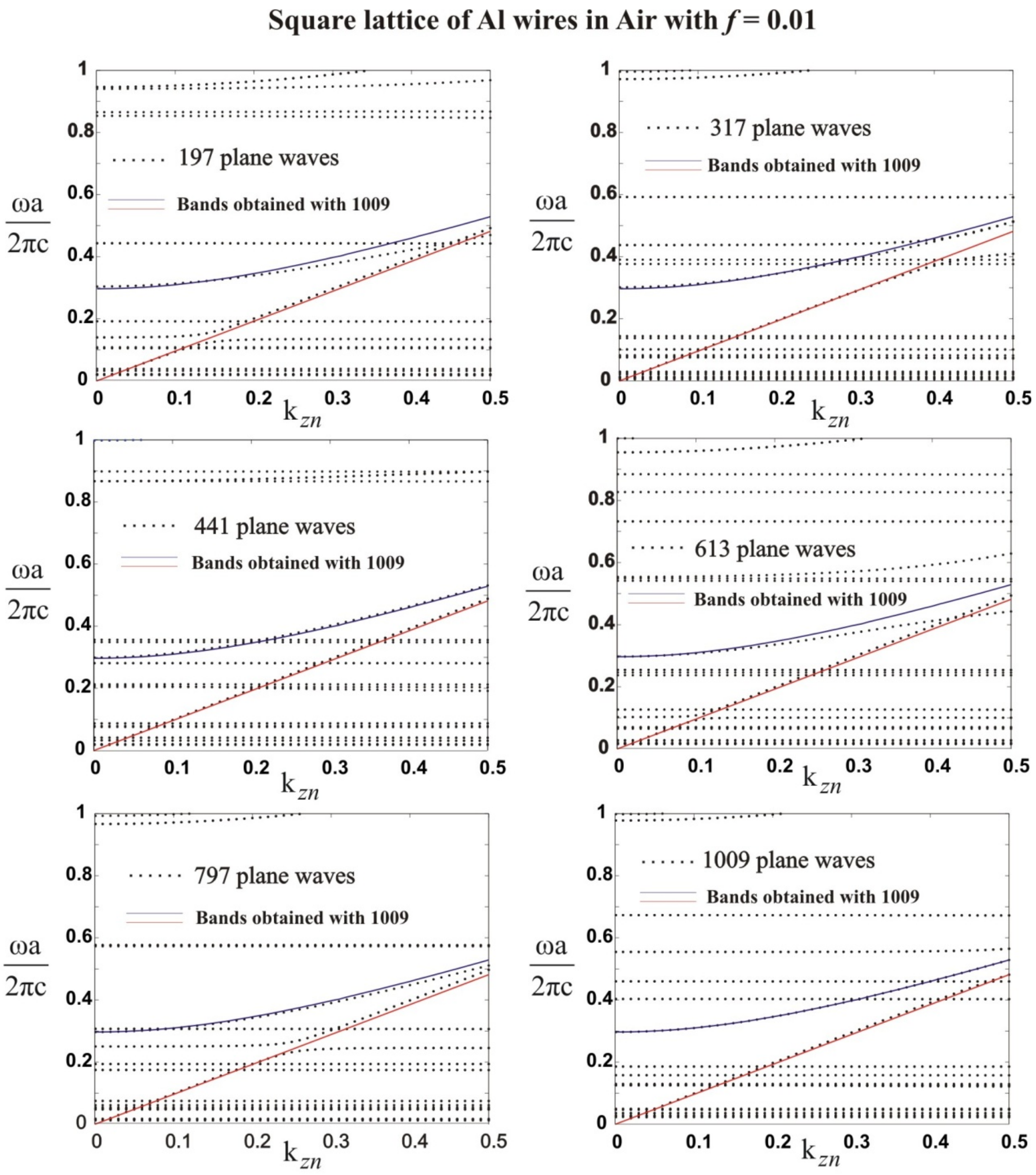

Square lattice of Al wires in Air with $f = 0.01$

Fig. G. 1. Band structure for the axial propagation of a square lattice of aluminum wires with a filling fraction f = 0.01. The figure shows the results obtained with different numbers of plane waves used to computed Eq. G2. The solid lines correspond to the first two band obtained with 1009 plane waves. Even the flat band does not reach convergence, for $k_z < 0.2$ the first two bands converge with only 441 plane waves.

Square lattice of Cu wires in Air with *f* = 0.01

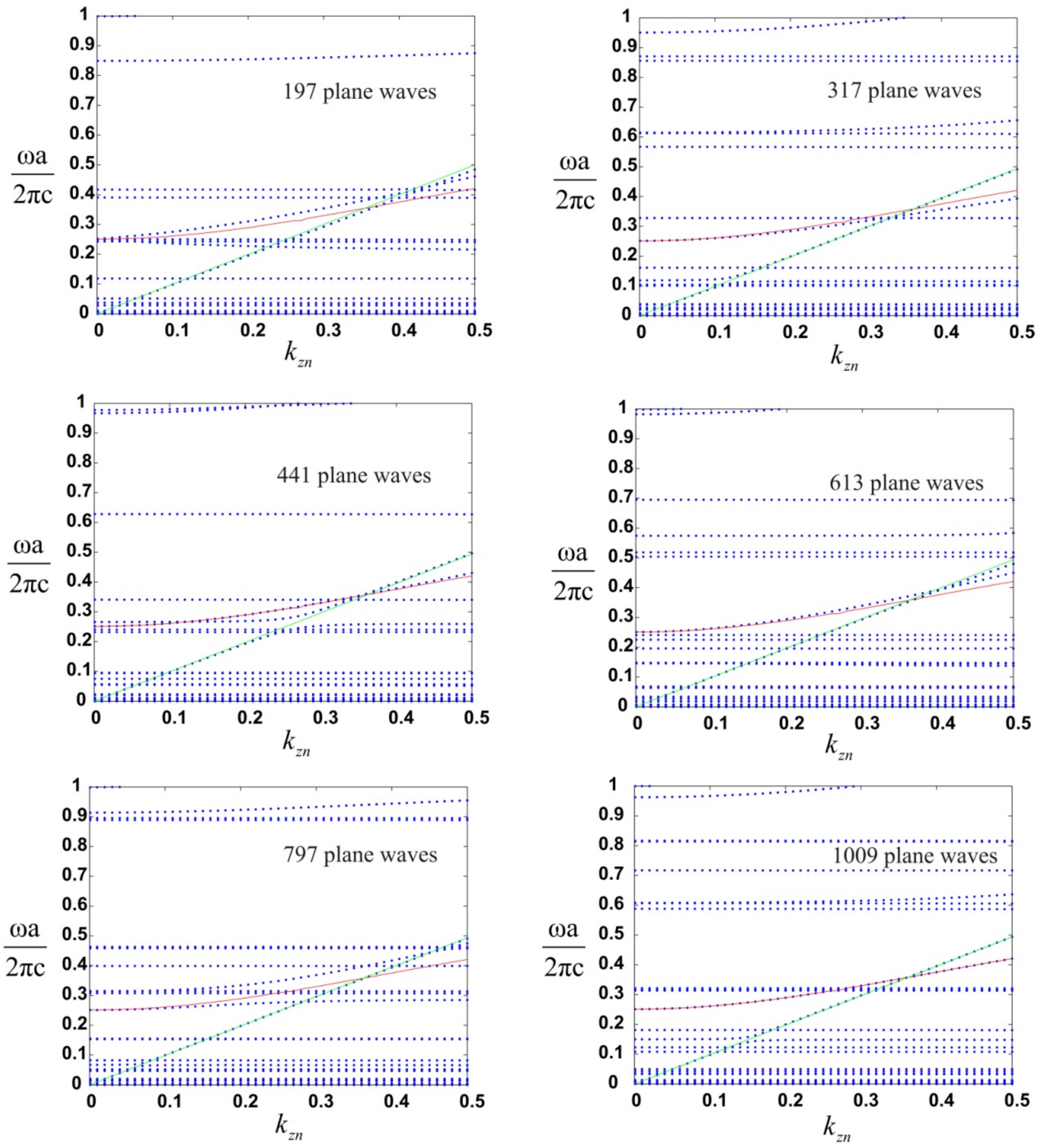

Fig. G.2. Band structure for the axial propagation of a square lattice of copper wires with a filling fraction *f* = 0.01. The figure shows the results obtained with different numbers of plane waves used to computed Eq. G2. The solid lines correspond to the first two band obtained with 1009 plane waves. Even the flat band does not reach convergence, for $k_z < 0.2$ the first two bands converge with only 441 plane waves.

Appendix H. Analysis of convergence for the Γ bands

In this section is analyzed the numerical convergence obtained in the dispersion relation and effective parameter computations. The dispersion relation was obtained using the equation G2 presented previously. Fig. H.1 shows the first three Γ bands for a triangular lattice of circular cylinders drilled in a dielectric matrix ($\varepsilon = 13$). Dotted lines indicate the points where the convergence will be analyzed.

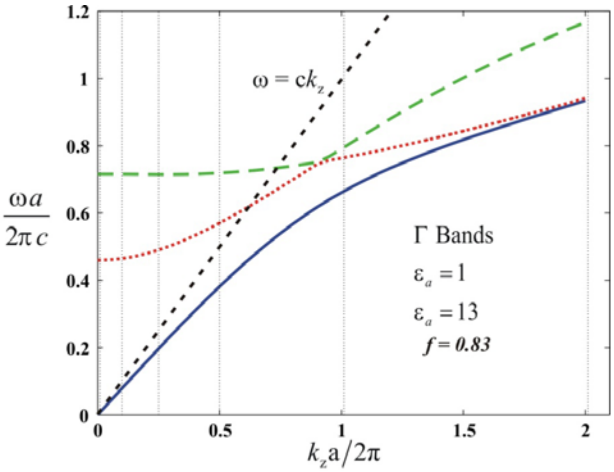

Fig. H.1.- Out-of-plane band structure of the triangular lattice of air columns for the first three Γ bands. The light line $\varpi = k_z \varpi$ is plotted whit a dashed line. The vertical dotted lines at $k_z = 0.01,\ 0.1, 0.25, 0.5,\ 1.01$ and 2.01 indicate the points where the convergence is analyzed.

Figure H.2 shows the dispersion relation as a function of the number of plane waves used in the computation. Each subfigure shows the convergence obtained for the first three bands at one point indicated by the dotted lines in Fig. H.1. At a first look, the results seem to indicate that lower bands and small wave vectors require less plane waves in order to obtain convergence that higher bands and bigger wave vectors.

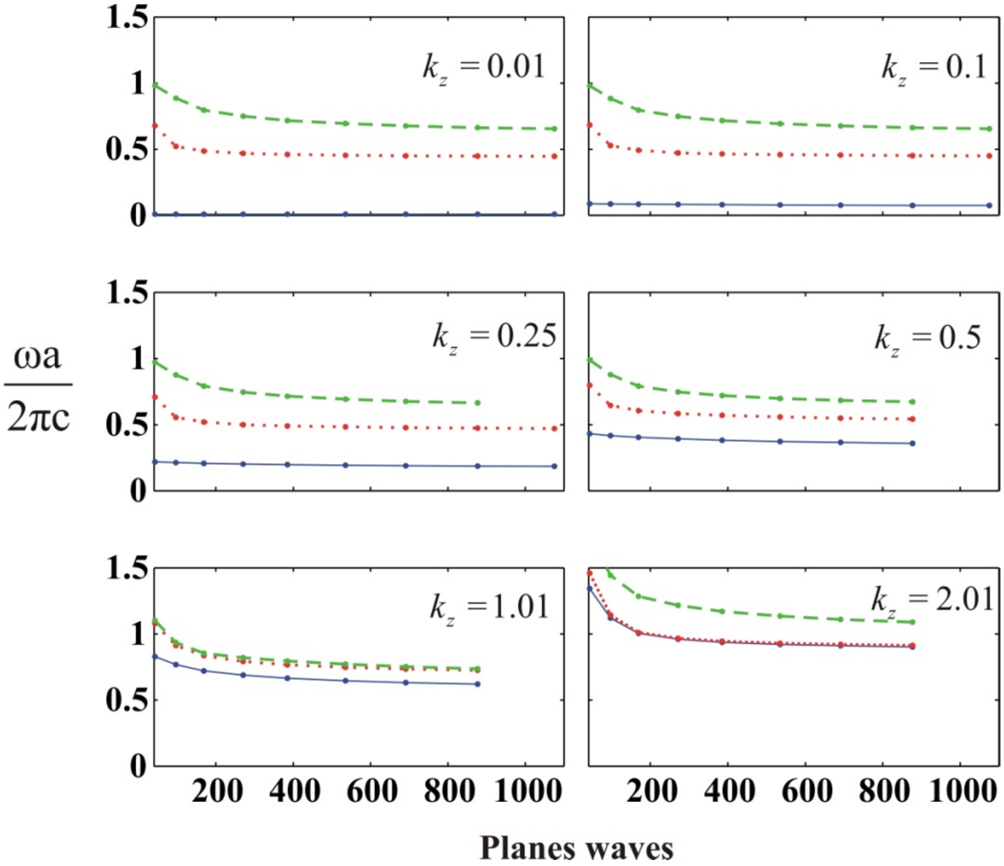

Fig. H.2.- Dispersion relation as a function of the number of plane waves used in the computation. Six k_z values are analyzed as is indicated by the vertical dotted lines in Fig. H.1. Solid, dotted and dashed lines correspond to the first, second and third Γ-band respectively.

A better analysis of Fig. H.2 is presented in table H.1, where is calculated the relative change of the dispersion relation between the values obtained using 877 and 691 plane waves respectively. This value was obtained as

$$\text{Relative change } = \left(\left| \omega_{877} - \omega_{691} \right| / \left| \omega_{877} \right| \right) \times 100 . \qquad \text{G4}$$

The results show in general that employing only 877 plane waves in the computation, it is possible to obtain a precision better than 2%.

Kz	1st Band	2nd Band	3th Band
0,01	1,52%	0,63%	1,99%
0,10	1,54%	0,67%	1,98%
0,25	1,60%	0,89%	1,90%
0,50	1,80%	1,42%	1,71%
1,01	1,88%	1,31%	2,19%
2,01	0,88%	0,76%	1,90%

Table H.1.- Relative change between the dispersion relation value obtained by using 877 and 691 plane waves. The results correspond to Eq. G4.

The effective permittivity as a function of the plane waves used in the computation is presented in Figs. H.3, H.4 and H.5 for the xx, yy and zz component respectively. Again, each subfigure corresponds to one specific wave vector. As is expected, same results are obtained for the xx and yy components because the system is homogeneous in the plane of periodicity. These two components show good convergence for the first and second band, mostly for small wave vectors. Nevertheless, the third band shows a divergent behavior with the exception of $k_z = 2.01$. Tables H.2 presents the relative change in the effective permittivity for the xx and yy components calculated in a similar way as Eq. G4. Same conclusions are obtained for the convergence of the ε_{zz} component (Fig. H.4). The first and second bands show good convergence. In contrast, the third band does not reach convergence with the maximum number of plane waves used in the computation. Finally, Fig. H.5 shows the computation time employed in obtaining the effective permittivity tensor for one band and one specific wave vector value. The computation time increases exponentially as the number of plane waves is increased.

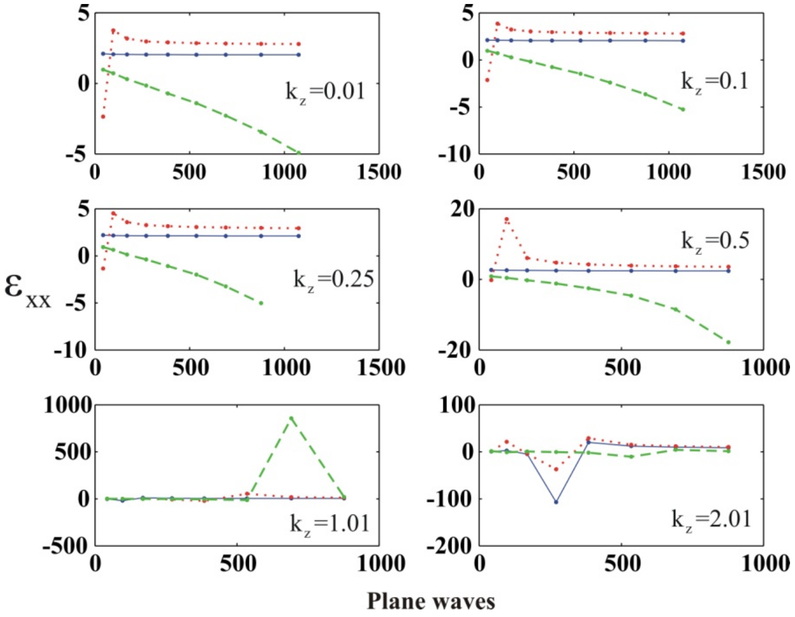

Fig. H.3 XX-Component of the effective permittivity as a function of the number of plane waves used in the computation. Six k_z values are analyzed as is indicated by the vertical dotted lines in Fig. H.1. Solid, dotted and dashed lines correspond to the firs, second and third Γ-bands respectively.

Kz	1st Band	2nd Band	3th Band
0,01	0,10%	0,82%	33,55%
0,10	0,11%	0,90%	33,71%
0,25	0,21%	1,40%	35,31%
0,50	0,78%	4,01%	52,24%
1,01	5,74%	45,39%	4340,99%
2,01	13,33%	15,09%	238,27%

Table H.2.- Relative change between the $\varepsilon_{xx} = \varepsilon_{yy}$ component value obtained by using 877 and 691 plane waves. The results are obtained in a similar way as in Eq. G4.

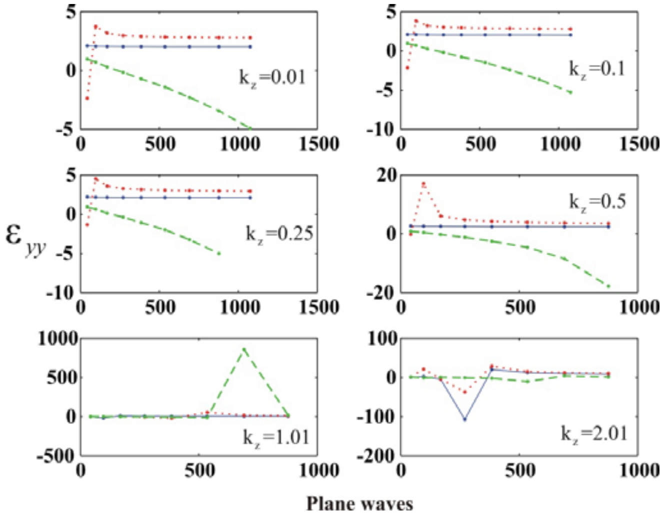

Fig. H.4. YY-Component of the effective permittivity as a function of the number of plane waves used in the computation. Six k_z values are analyzed as is indicated by the vertical dotted lines in Fig. H.1. Solid, dotted and dashed lines correspond to the firs, second and third Γ-bands respectively.

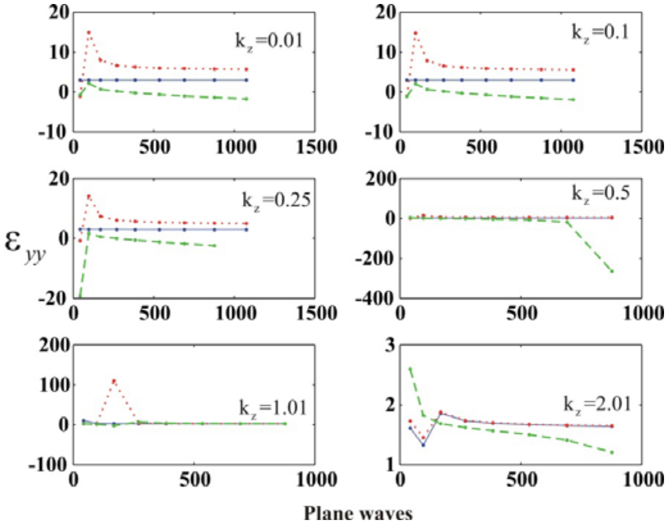

Fig. H.5. ZZ-Component of the effective permittivity as a function of the number of plane waves used in the computation. Six k_z values are analyzed as is indicated by the vertical dotted lines in Fig. H.1. Solid, dotted and dashed lines correspond to the first, second and third Γ-bands respectively.

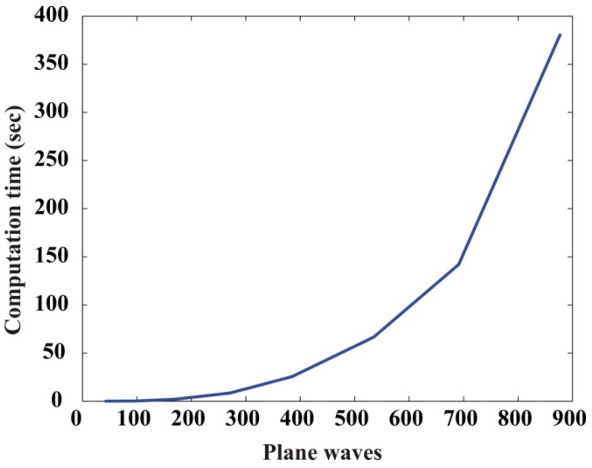

Fig. H.6. Computation time as a function of the number of plane waves employed. The time corresponds to the effective permittivity computation (the three components) for one band and one specific wave vector.

Kz	1st Band	2nd Band	3th Band
0,01	0,00%	1,82%	26,66%
0,10	0,04%	1,95%	26,32%
0,25	0,22%	2,52%	26,19%
0,50	0,80%	3,62%	93,29%
1,01	1,46%	3,03%	5,90%
2,01	0,64%	0,64%	16,72%

Table H.3.- Relative change between the ε_{zz} component value obtained by using 877 and 691 plane waves. The results are obtained in a similar way as in Eq. G4.

List of figures

Fig. 1.1 Simple forms of photonic crystals 3

Fig. 1.2 Photonic band structure of a triangular lattices of circular holes in a dielectric medium 5

Fig. 1.3 Representation of the homogenization process 6

Fig. 1.4 Artificial material created by Smith and collaborators possessing a negative refractive index 7

Fig. 2.1 Effective permittivity and permeability of arrays of circular Si rods in air and of cylindrical holes in a Si host as a function of the filling fraction 38

Fig. 2.2 Effective permittivity and effective permeability of a 3D PC of dielectric spheres in a cubic lattice as a function of the filling fraction 39

Fig. 2.3 E-mode dispersion relation for the first band and the relevant elements of the effective permittivity and permeability dyadics for a square lattice of copper wires 41

Fig. 2.4 Effective permeability and effective permittivity for the H-mode as a function of the filling fraction for a square lattice of metallic wires 42

Fig. 2.5 Effective parameters of a cubic lattice of continuous metallic wires of square cross-section 45

Fig. 2.6 Effective parameters for a PC formed of three-dimensional metallic crosses being separated by a small gap 46

Fig. 2.7 Same as Fig. 2.6 but with a larger gap between wires in neighboring cells 47

Fig. 2.8 Summary of Figs. 2.5, 2.6 and 2.7 49

Fig. 3.1 Band structure, effective parameters, and polarization for the first two band of axial propagation of a square lattice of silicon cylinders 63

Fig. 3.2 Effective permittivity as a function of the filling fraction for a triangular lattice of air-cylinder in a silicon. 66

Fig. 3.3. Effective permittivity for the first two Γ bands of a square lattice of aluminum and copper wires 67

Fig. 3.4 Comparison between the results presented in Ref. [93] and the results obtained using the homogenization process proposed in this work. 69

Fig. 4.1 Inclination of the NLC director θ versus the dimensionless radial distance for the nematic 5CB with $\eta = 1.316$ and $\sigma = 1.25$ 84

Fig. 4.2 As in Fig. 4.1 for $\sigma = 2$ and q = 0, 1, 2, 3, 4, 4.5, 4.7, 4.75 85

Fig. 4.3 As in Fig. 4.1 for $\sigma = 4$ and q = 0, 1, 2, 3, 4, 5, 6, 7, 8, 9, 11, 13, 15, 17, 19, 19.2 85

Fig. 4.4 As in Fig. 4.1 for $\sigma = 8$ and q = 0, 1, 2, 3, 4, 5, 6, 9, 11, 15, 20, 30, 40, 60, 70, 71.39...... 86

Fig. 4.5 E_0 as function of *R*. Eq. 4.32 provides the asymptotic value for E_0 88

Fig. 4.6 Polarization vectors for magnetic field, Eq. (4.46), referred to coordinate axes of photonic crystal 97

Fig. 4.7 Comparison of exact (dots) and approximate (lines and dashed lines) photonic band structures for *5CB* nematic liquid crystal cylinders forming a square lattice in a silica host, for the field parameter $q = 20$ 105

Fig. 4.8 Electrical tuning of the photonic bands for the photonic crystal considered in the previous figure. 106

Fig. 5.1 Average dielectric constants ε_E (ε_H) of a nematic liquid crystal cylinder for electric field E (magnetic field H) parallel to the cylinder, as function of the electric field parameter q 115

Fig. 5.2 PC homogenization process 116

Fig. 5.3 Relative changes of the effective refractive indices of a two-dimensional PC of NLC cylinders in a silica matrix, as the applied electric field changes from zero beyond its critical value 117

Fig. 5.4 Angles of refraction for ordinary and extraordinary rays in the homogenized medium.. 118

Fig. 5.5 Effective permittivity in a two-dimensional photonic crystal of metallic wires in a square lattice surrounded by the liquid crystal 5CB 119

Fig. F.1 Principal dielectric constants of a PC made of Si-cylinders in a square lattice as a function of the number of G values used in the computation 141

Fig. F.2 Effective permittivity as a function of the number of G values used in the computation for a system of dielectric spheres in a cubic lattice, as in Fig. 2.2. 142

Fig. F.3 Effective permeability of a square lattice of copper wires as a function of the filling fraction for the H-mode, as in Fig. 2.4 143

Fig. G.1 Band structure for the axial propagation of a square lattice of aluminum wires with a filling fraction $f = 0.01$ 146

Fig. G.2 Band structure for the axial propagation of a square lattice of copper wires with a filling fraction $f = 0.01$ 147

Fig. H.1 Out-of-plane band structure of the triangular lattice of air columns for the first three Γ band 148

Fig. H.2 Dispersion relation as a function of the number of plane waves used in the computation. 149

Fig. H.3 XX-Component of the effective permittivity as a function of the number of plane waves used in the computation 151

Fig. H.4 YY-Component of the effective permittivity as a function of the number of plane waves used in the computation 152

Fig. H.5 ZZ-Component of the effective permittivity as a function of the number of plane waves used in the computation 152

Fig. H.3 Computation time as a function of the number of plane waves employed. The time corresponds to the effective permittivity computation (the three components) for one band and one specific wave vector............................ 153

List of tables

Table H.1 Relative change between the dispersion relation value obtained by using 877 and 691 plane waves. The results correspond to Eq. Error! Reference source not found.. 150

Table H.2 Relative change between the $\varepsilon_{xx} = \varepsilon_{yy}$ component value obtained by using 877 and 691 plane waves. The results are obtained in a similar way as in Eq. Error! Reference source not found. 152

Table H.3 Relative change between the ε_{zz} component value obtained by using 877 and 691 plane waves. The results are obtained in a similar way as in Eq. Error! Reference source not found. 153

Resumen en extenso

Esta tesis se ha dedicado al estudio de cristales fotónicos (CF) bidimensionales (2D) en el límite de grandes longitudes de onda mediante la obtención de sus parámetros efectivos. Además, se ha demostrado que dichos parámetros pueden ser sintonizados mediante un campo eléctrico externo, si se usa un cristal líquido (CL) como parte de la estructura periódica. Este trabajo está basado en tres componentes principales: el proceso de homogenización, la interacción entre un campo eléctrico de DC y un CF de cilindros huecos rellenos con CL, y finalmente, la sintonización de los parámetros efectivos usando un agente externo. El estudio de cada una de estas componentes ha generado la escritura de 4 artículos en colaboración con otros autores [90, 138, 144, 145]. Cada artículo corresponde un capítulo de esta tesis.

En el capítulo 1 se ha dado una introducción general a los temas que se investigan en esta tesis. En el capítulo 2 se presenta la teoría de homogenización propuesta por P. Halevi and F. Pérez-Rodríguez. Esta teoría constituye una de las bases sobre las cuales se ha construido este trabajo. En este capítulo también se presentan los primeros resultados de esta tesis relacionados con la homogenización de CF 2D para el caso de la propagación en el plano, considerando estructuras dieléctricas y metalo-dieléctricas. En el capítulo 3 se propone una extensión a la teoría de homogenización que permite el estudio de la propagación axial en CFs 2D sin la necesidad de restringir el vector de la onda a valores muy pequeños como sucede en la teoría general [90]. En este capítulo también se incluye un estudio de la polarización de las ondas que se propagan en la dirección axial el cual es de gran ayuda para interpretar los resultados obtenidos del proceso de homogenización. En el capítulo 4 se aborda la segunda componente de esta tesis. En él se estudia la configuración que adoptan las moléculas de un CL nemático dentro de un cilindro circular y su interacción con un campo eléctrico externo. También se muestra como un CF formado de cilindros huecos rellenos de CL, cambia su estructura de bandas fotónica cuando se aplica un campo eléctrico externo. Finalmente, el tercer componente de esta tesis se presenta en el capítulo 5. En este capítulo se muestra cómo se puede sintonizar los parámetros efectivos de un CF 2D formado de cilindros huecos rellenos de CL. Un campo eléctrico externo modifica la dirección de las moléculas y en consecuencia la permitividad efectiva que caracteriza al CF. Finalmente en el capítulo 6 se dan las conclusiones de esta tesis. A continuación se presenta un resumen de los aspectos más relevantes de los capítulos 2, 3, 4 y 5 en donde se encuentran las aportaciones más importantes de esta tesis.

Capítulo 2

En este capítulo se presentó una teoría muy general de homogenización que permite calcular la respuesta electromagnética de un CF en el límite de grandes longitudes de onda. Aplicando esta teoría de campo medio se derivaron expresiones analíticas (las cuales requieren inversión de matrices) para los diádicos efectivos tanto de la respuesta dieléctrica como de la respuesta bi-anisotrópica. Las expresiones para estos diádicos han sido determinadas en términos de la celda unitaria y de la red de Bravais. La permitividad ($\overleftrightarrow{\boldsymbol{\varepsilon}}$), la permeabilidad ($\overleftrightarrow{\boldsymbol{\mu}}$), y los diádicos magneto-eléctricos ($\overleftrightarrow{\boldsymbol{\gamma}}$, $\overleftrightarrow{\boldsymbol{\delta}}$) han sido expresados en términos del diádico de la conductividad ($\overleftrightarrow{\boldsymbol{\Sigma}}$), para el cual se han incluido dos fórmulas equivalentes; una brinda una comprensión más física del proceso de homogenización y la otra es más conveniente desde el punto de vista computacional.

A diferencia de la respuesta dieléctrica no-local, la respuesta bi-anisotrópica permite emerger las propiedades magnéticas a nivel macroscópico. Esta respuesta también tiene la ventaja de que los diádicos $\overset{\leftrightarrow}{\boldsymbol{\varepsilon}}$, $\overset{\leftrightarrow}{\boldsymbol{\mu}}$, $\overset{\leftrightarrow}{\boldsymbol{\gamma}}$ y $\overset{\leftrightarrow}{\boldsymbol{\delta}}$ son independientes de la magnitud del vector de vector de onda (aunque en general dependen de su dirección). Resulta interesante que el diádico de la permeabilidad $\overset{\leftrightarrow}{\boldsymbol{\mu}}$ de la respuesta bi-anisotrópica es diagonal en un sistema de coordenadas en el cual uno de sus ejes es paralelo al vector de onda k. En consecuencia, en general los ejes principales del diádico de la permitividad $\overset{\leftrightarrow}{\boldsymbol{\varepsilon}}$ y de la permeabilidad $\overset{\leftrightarrow}{\boldsymbol{\mu}}$ no coinciden, siendo la excepción configuraciones de alta simetría. Esta situación podría generar nuevos resultados en la óptica cristalina de estructuras periódicas.

Dentro de esta teoría de homogenización, los diádicos cruzados ($\overset{\leftrightarrow}{\boldsymbol{\gamma}}$, $\overset{\leftrightarrow}{\boldsymbol{\delta}}$) de la respuesta bi-anisotrópica desaparecen en el límite $k \rightarrow 0$ si la celda unitaria posee simetría de inversión. Por lo tanto, en este importante escenario la respuesta está exclusivamente en dada en términos de $\overset{\leftrightarrow}{\boldsymbol{\varepsilon}}$ y $\overset{\leftrightarrow}{\boldsymbol{\mu}}$. Aún en esta simple situación, la física de los materiales anisotrópicos es muy rica (ver por ejemplo, Rosa et al [53, 63]).

Esta teoría fue verificada reduciendo los resultados generales a algunos resultados obtenidos en trabajos previos: analíticamente, a la formula de Maxwell-Garnett para esferas pequeñas y a la permitividad efectiva calculada por Pendy para un sistema 3D de alambres metálicos ("cruces 3D") y numéricamente, para cilindros dieléctricos 2D y esferas dieléctricas 3D. Además, fueron presentados resultados numéricos para cristales metalo-dieléctricos. En contraste con el caso de estructuras puramente dieléctricas donde no existen efectos magnéticos, se ha encontrado comportamiento paramagnético y diamagnético en CF 2D de alambres metálicos. El comportamiento es paramagnético si la polarización del campo eléctrico de la onda es paralela a los alambres o diamagnético si la polarización del campo eléctrico es transversal a los alambres. También fueron estudiados en detalle sistemas 3D de alambres mutuamente perpendiculares (cruces 3D), enfocándose en la transición de alambres continuos a alambres cortados y determinando el efecto del espacio entre los alambres cortados. Este corte lleva a la desaparición de la banda prohibida que se observa para alambres continuos y a la aparición de una banda de paso acústica para el caso de alambres cortados. La segunda banda de paso muestra un valor negativo tanto en la permitividad como en la permeabilidad. Este comportamiento metamaterial proviene de la capacitancia creada en los espacios entre los alambres cortados y las corrientes de eddy inducidas por el campo magnético.

La teoría que se presenta en este capítulo parte de la descripción a nivel-mico o del cristal fotónico y llega a la descripción a nivel-macro o de un medio homogéneo. La teoría está basada en principios fundamentales, caracterizando el CF por medio de una conductividad generalizada que es función de la posición. En principio, las formulas finales de la respuesta bi-anisotrópica ($\overleftrightarrow{\boldsymbol{\varepsilon}}$, $\overleftrightarrow{\boldsymbol{\mu}}$, $\overleftrightarrow{\boldsymbol{\gamma}}$ y $\overleftrightarrow{\boldsymbol{\delta}}$) pueden ser aplicadas a cristales fotónicos con periodicidad en una, dos, o tres dimensiones con cualquier red de Bravais y cualquier celda unitaria. El trabajo numérico involucra inversión de matrices y sumatoria sobre vectores de la red recíproca. El inconveniente que puede presentar este método es que la convergencia puede ser lenta, la capacidad de memoria en la computadora puede ser insuficiente y los tiempos de cómputos pueden ser largos.

Finalmente, se debe mencionar que la aplicación de esta teoría a la respuesta óptica también requiere que la frecuencia sea pequeña ($2\pi c/\omega \gg a$), además de que el vector de la onda también debe ser pequeño ($2\pi/k \gg a$).

Capítulo 3

Este capítulo se dedica al estudio de la propagación axial de ondas electromagnéticas en CF 2D en el límite de grandes longitudes de onda mediante la obtención de sus parámetros efectivos. Como consecuencia de la simetría de translación que existe para esta dirección de propagación, se debe poner especial atención a la naturaleza del vector de onda **k**. En contraste con el caso de la propagación en el plano donde **k** es un vector de onda de Bloch, para la propagación axial, **k** es un vector de onda ordinario sin ninguna restricción en su magnitud. Tomando en cuenta este punto importante y usando la conductividad generalizada $\hat{\boldsymbol{\sigma}}(\mathbf{r})$ como el único parámetro describiendo la celda unitaria se ha desarrollado una expresión general para la permitividad efectiva de manera similar a como fue hecho en el capítulo 2. Esta fórmula general puede ser usada para estudiar estructuras dieléctricas y metalo-dieléctricas sin la necesidad de restringir el estudio a valores pequeños del vector de onda.

Con la finalidad de dar una descripción completa para esta dirección de propagación, se ha llevado a cabo un estudio de la polarización para las 3 primeras bandas. El análisis consistió en graficar las tres componentes del campo eléctrico y del campo magnético dentro de la celda unitaria. Este procedimiento determina cuál de las tres componentes del diádico dieléctrico está involucrado en la propagación de la onda. Los resultados muestran que en el límite de grandes longitudes de onda, la primera banda muestra una polarización transversal, mientras que la segunda banda muestra una polarización longitudinal.

En el caso de estructuras dieléctricas se analizó una red cuadrada de cilindros de silicio, una red triangular cilindros de silicio y una red triangular de cilindros huecos en silicio. La permitividad efectiva obtenida para la primera banda en estas estructuras muestra un buen acuerdo con los resultados derivados de la relación de dispersión. Por otra parte, el proceso de homogenización falla para la segunda banda como consecuencia de las fuertes oscilaciones que muestra el campo eléctrico dentro de la celda unitaria. Sin embargo, el estudio de la polarización llevado a cabo para la segunda banda muestra que el valor de la permitividad efectiva debe ser igual a cero tal y como corresponde a una polarización longitudinal.

En el caso de estructuras metalo-dieléctricas se analizó una red cuadrada de alambres de cobre y una red cuadra de alambres de aluminio. La fracción de llenado se escogió muy pequeña para mantener una frecuencia baja en la segunda banda. Esta selección reduce las oscilaciones del campo eléctrico dentro de la celda unitaria y en consecuencia el proceso de homogenización da el resultado esperado $\varepsilon_{zz} = 0$. Como se mencionó anteriormente, la primera banda tiene una polarización transversal con su campo eléctrico oscilando en el plano de la periodicidad. Como consecuencia de una fracción de llenado tan pequeña, el campo eléctrico no interactúa con los alambres metálicos y la permitividad efectiva es muy cercana a la del vacío.

Finalmente, los resultados de esta teoría fueron comparados con un experimento reportado en la literatura [93]. Aunque el experimento fue realizado sobre una oblea delgada de silicio (lo que no corresponde a un CF), la permitividad efectiva obtenida a través de esta teoría es congruente con los resultados experimentales.

Capítulo 4

En este capítulo se lleva a cabo el estudio de la sintonización eléctrica de un CF 2D infiltrado con el cristal líquido nemático (CLN) 5CB. El CLN es caracterizado por un conjunto completo de parámetros elásticos de bulto y superficie. El efecto de sintonización se obtiene al aplicar un campo eléctrico de DC en la dirección axial. Minimizando la energía libre total (elástica más electromagnética), se obtiene la configuración de los directores de las moléculas del CLN en función de la distancia radial. Se consideraron tres posibles configuraciones: la escapada radial, la planar radial y la configuración axial. Se encontró que en general, la configuración escapada radial es la adoptada por las moléculas. Sin embargo, cuando se aplican campos eléctricos lo suficientemente grandes, ocurre una transición a la configuración axial. Por ejemplo, en el caso del CLN 5CB, esta transición se obtiene cuando se aplica un campo eléctrico aproximadamente de 14 V/μm, siempre y cuando el radio de los cilindros sea mayor que 50nm. La configuración de los directores del CLN determina el tensor dieléctrico dentro de los cilindros como una función de la distancia radia, y este a su vez, es usado para obtener la estructura de bandas del CF.

En este capítulo se presentan dos ecuaciones para realizar el cálculo de la estructura de bandas: una exacta y otra aproximada. La ecuación de eigenvalores exacta toma en cuenta por completo el comportamiento anisotrópico del tensor dieléctrico dentro de los cilindros. Esta anisotropía no permite llevar a cabo la separación usual a modos-E y modos-H en un CF 2D. La ecuación aproximada se obtiene a través de promediar el tensor dieléctrico sobre la sección transversal del cilindro. Este proceso de promediado permite la separación usual en modos-E y modos-H que tienen su campo eléctrico respectivamente, perpendicular y paralelo a los cilindros. El cálculo de la estructura de bandas por ambos métodos muestra que el cálculo aproximado funciona muy bien para cilindros de CLN 5CB en una matriz de oxido de silicio. El cálculo aproximado permite introducir la terminología “polarización cuasi-E” y “polarización cuasi-H” para describir a los modos separados artificialmente por el proceso de promediado.

Los resultados numéricos muestran que la estructura de bandas puede ser sintonizada aplicando un campo eléctrico externo. En particular, la banda prohibida fotónica que se observa para la polarización cuasi-E puede ser cerrada por completo cuando se aplica un campo eléctrico lo suficientemente grande. En consecuencia, el paso de luz incidente polarizada con su campo eléctrico en la dirección paralela a los cilindros puede ser permitido ó evitado por medio del campo externo. El sistema que se ha estudiado puede servir como un filtro de polarización controlado eléctricamente, permitiendo únicamente la transmisión de la componente cuasi-H de la luz incidente cuando el campo eléctrico esta encendido.

Capítulo 5

En este capítulo se conjugan la teoría de homogenización presentada en al capítulo 2 y la sintonización de las propiedades ópticas presentada en el capítulo 4. Aquí se propone un novedoso sistema electro-óptico que tiene aplicaciones potenciales para controlar la dirección de haces de luz, como un multiplexor óptico, como una compuerta óptica lógica o como un interruptor óptico. La idea se basa en la sintonización eléctrica de la refracción en un cristal fotónico bidimensional de cilindros huecos infiltrados con cristal líquido cuando un campo eléctrico de DC es aplicado de forma paralela a los cilindros.

El cálculo del ángulo de refracción se ha llevado a cabo usando un proceso de homogenización de dos etapas. En primero, el tensor dieléctrico que caracteriza a los cilindros de CL es promediado sobre la sección transversal de los mismos. Este procedimiento permite caracterizar a los cilindros mediante dos constantes dieléctricas para un valor dado del campo eléctrico externo: la constante dieléctrica para los modos-E y la constante dieléctrica para los modos-H. El segundo paso completa el proceso de homogenización y permite representar a la estructura periódica a través de un índice de refracción efectivo para cada polarización.

Debido a la naturaliza uni-axial del medio homogenizado, la onda electromagnética incidente se divide en dos rayos: el ordinario y el extraordinario. Los ángulos de refracción de ambos haces se pueden variar continuamente hasta en un 6% en comparación con el caso donde no se aplica campo externo (considerando un ángulo de incidencia de 60°). Como se mostró el capítulo 2, el segundo proceso de homogenización requiere que $\lambda \gg a$, esto es, la región lineal de la estructura de bandas del CF en donde $\omega \simeq kc/n_{o,e}(q)$. Lo anterior implica típicamente el régimen infrarrojo. Sí el CF es colocado en un capacitor con una distancia de separación entre placas aproximada de ~ 15 μm, la sintonización de la estructura se puede alcanzar usando valores máximos de 70 V.

El sistema propuesto puede ser usado para el direccionamiento de haces de luz usando por ejemplo un prisma hecho de CF como es propuesto en la Ref. (140). Otra aplicación potencial se encuentra en lentes hechas de CF como se sugiere en la Ref. [139], pero con la posibilidad de controlar su foco. Una aplicación más se puede encontrar en la fabricación de multiplexores ópticos en los cuales la trayectoria del haz de luz puede ser seleccionada mediante un agente externo. Este sistema también abre la puerta a la fabricación de compuertas ópticas lógica e interruptores ópticos.

Conclusión final

En este trabajo de tesis tesis se ha llevado a cabo un estudio sobre cristales fotónicos bidimensionales en el límite de grandes longitudes de onda y la sintonización de sus parámetros efectivos. La teoría de homogenización general en la cual se basa este trabajo puede ser usada para calcular los parámetros efectivos tanto para la respuesta dieléctrica como para la respuesta bi-anisotrópica. Esta teoría general se puede aplicar a sistemas con periodicidad en una, dos o tres dimensiones con cualquier forma de la celda unitaria. En el caso de la propagación axial en cristales fotónicos bidimensionales, se ha propuesto una extensión a la teoría general que permite el cálculo de la permitividad efectiva sin la necesidad de restringir el vector de la onda a valores muy pequeños. Sin embargo es importante recalcar que existe una restricción indirecta a su magnitud ya que la frecuencia de la onda no puede ser arbitrariamente grande.

En este trabajo se muestra cómo se pueden modificar los parámetros efectivos mediante la incorporación de un cristal líquido como parte de la estructura periódica. Los resultados muestran que las moléculas de un cristal líquido nemático dentro de un cilindro hueco adoptan la configuración escapada radial cuando no existe un campo eléctrico aplicado. Cuando se aplica un campo eléctrico externo paralelo a los cilindros, las moléculas se alienan paulatinamente con el campo conforme incrementa su magnitud. Para campos suficientemente grandes, el cristal líquido adopta la configuración axial. Este cambio en la dirección de las moléculas se traduce en un cambio de los parámetros efectivos. Además, usando un proceso de homogenización de dos pasos, se muestra que para frecuencias lo suficientemente bajas, tal estructura puede ser representada por dos índices de refracción que dependen del campo eléctrico. Se demuestra que la dirección de los haces refractados (ordinario y extraordinario) pueden ser modificados cuando se varía la magnitud del campo aplicado.

Los resultados que se presentan en esta tesis pueden ser usados como base para la fabricación de dispositivos destinados a controlar el flujo de la luz. Por otro lado, la homogenización que se presenta en este trabajo es sin duda una herramienta valiosa para el estudio de metamateriales cuyo comportamiento es un tópico de gran interés en la comunidad científica.

REFERENCES

[1] J.D. Jackson, *Classical electrodynamics*, John Wiley & Sons, New York, 1975.

[2] E. U. Condon, Rev. Mod. Phys. 9, **432**(1937).

[3] J.D. Joannopoulos, R.D. Meade, and J.N.Winn, *Photonic Crystals: Molding the Flow of Light*, *2nd Edition*, Princeton University Press, Princeton, NJ, 2008.

[4] Y. Fink, Joshua N. Winn, Shanhui Fan, Chiping Chen, Jurgen Michel, John D. Joannopoulos, and Edwin L. Thomas, Science **282**, 1679 (1998).

[5] E. Chow, S. Y. Lin, J. R. Wendt, S. G. Johnson, and J. D. Joannopoulos, *Opt. Lett.* **26**, 286 (2001).

[6] K. Asakawa, Y. Sugimoto, Y. Watanabe, N. Ozaki, A. Mizutani, Y. Takata, Y. Kitagawa, H. Ishikawa, N. Ikeda, K. Awazu, X. Wang, A. Watanabe, S. Nakamura, S. Ohkouchi, K. Inoue, M. Kristensen, O. Sigmund, P. I. Borel and R. Baets, New J. Phys. **8**, 208 (2006).

[7] M. Loncar, T. Yoshie, A. Scherer, P. Gogna, and Y. Qiu, Appl. Phys. Lett. **81**, 2680 (2002).

[8] S. –Y. Lin, V. M. Hietala, L. Wang, and E. D. Jones, Opt. Lett. **21**, 1771 (1996).

[9] H. Kosaka, T. Kawashima, A. Tomitama, M. Notomi,. Tamamura, T. Sato, and S. Kawakami, Phys. Rev. B **58**, R10096 (1998).

[10] P. Halevi, A.A. Krokhin, and J. Arriaga, Phys. Rev. Lett. **82**, 719 (1999).

[11] D. R. Smith, Willie J. Padilla, D. C. Vier, S. C. Nemat-Nasser, and S. Schultz, Phys. Rev. Lett. **84**, 4184 (2000).

[12] R. A. Shelby, D. R. Smith, S. C. Nemat-Nasser, and S. Schultz, Appl. Phys. Lett. **78**, 489 (2001).

[13] R. A. Shelby, D. R. Smith, and S. Schultz, Science **292**, 77 (2001).

[14] J. B. Pendry and D.R. Smith, Phys. Today **57**, 37(2004).

[15] J. B. Pendry, Phys. Rev. Lett. **85**, 3966 (2000).

[16] A. A. Houck, J. B. Brock, and I. L. Chuang, Phys. Rev. Lett. **90**, 137401 (2003).

[17] Z. Jian and D. M. Mittleman, Appl. Phys. Lett. **87**, 191113 (2005).

[18] D. R. Smith, D. C. Vier, Th. Koschny, and C. M. Soukoulis, Phys. Rev. E **71**, 036617 (2005).

[19] T. Koschny, P. Markoš, E. N. Economou, D. R. Smith, D. C. Vier, and C. M. Soukoulis, Phys. Rev. B **71**, 245105 (2005).

[20] X. Chen, B. Wu, J. Kong, and T. M. Grzegorczyk, Phys. Rev. E **71**, 046610 (2005).

[21] D.R. Smith, D. C. Vier, N. Kroll, and S. Schultz, Appl. Phys. Lett. **77**, 2246 (2000).

[22] D.R. Smith and J. B. Pendry, J. Opt. Soc. Am. B **23**, 391 (2006).

[23] R. Tao, Z. Chen, and P. Sheng, Phys. Rev. B **41**, 2417 (1990).

[24] S. Datta, C. T. Chan, K. M. Ho, and C. M. Soukoulis, Phys. Rev. B **48**, 14936 (1993).

[25] A. A. Krokhin, P. Halevi, and J. Arriaga, Phys. Rev. B **65**, 115208 (2002).

[26] A. A. Krokhin, E. Reyes, and L. Gumen, Phys. Rev. B **75**, 045131 (2007).

[27] S.T. Chui and Zhifang Lin, Phys. Rev. E **78**, 065601(R) (2008).

[28] K. Yoshino, Y Kawagishi, M. Ozaki, and A. Kose, J. Appl. Phys. **38**, 786L (1999).

[29] S. Kim and V. Gopalan, Appl. Phys. Lett. **78**, 3015 (2001).

[30] A. Figotin, Y. A. Godin, and I. Vitebski, Phys. Rev. B **66**, 195108 (2002).

[31] P. Halevi and F. Ramos-Mendieta, Phys. Rev. Lett. **85**, 1875 (2000).

[32] S. W. Leonard, J. P. Mondia, A. M. Van Driel, O. Toader, s. Jhon, K. Busch, A. Birner, V. Gosele, and V. Lehmann, Phys. Rev. B **61**, R2389 (2000).

[33] K. Busch and S. John, Phys. Rev. Lett. **85**, 5 (1999).

[34] D. Scrymgeour, N. Malkova, S. Kim, and V. Gopalan, Appl. Phys. Lett. **82**, 3176 (2003);

[35] S. Xiong and H. Fukshima, J. Appl. Phys. **94**, 1286(2003);

[36] W. Park and J. Lee, Appl. Phys. Lett. **85**, 4845 (2004);

[37] L. Feng, X. Liu, Y. Tang, Y. Chen, J. Zi, S. Zhu, and Y. Zhu, Phys. Rev. B **71**, 195106 (2005).

[38] H. Takeda and K. Yoshino, Phys. Rev. E **67**, 056607(2003).

[39] L.D. Landau and E.M. Lifshitz, *Electrodynamics of Continuous Media*, Elsevier Butterworth-Heinemann, Amsterdam, 2004.

[40] V. M. Agranovich and Yu. N. Gartstein, Phys. Usp. **49**, 1029 (2006).

[41] A. Schuster, *An Introduction to the Theory of Optics 2nd ed.* (London: E. Arnold, 1909).

[42] L. I. Mandel'shtam, Zh. Eksp. Teor. Fiz. **15,** 475 (1945).

[43] L. I. Mandel'shtam, *Lektsii po Optike, Teorii Otnositel'nosti i Kvantovoi Mekhanike* (Lectures on Optics, Relativity, and Quantum Mechanics) (Moscow: Nauka, 1972).

[44] D. V. Sivukhin, Opt. Spectrosc. **3**, 308 (1957).

[45] V. E. Pafomov, Zh. Eksp. Teor. Fiz. **30** 761 (1956) [Sov. Phys. JETP **5**, 597 (1956)].

[46] V. E. Pafomov, Zh. Eksp. Teor. Fiz. **33**, 1074 (1957) [Sov. Phys. JETP **6**, 806 (1958)].

[47] V. E. Pafomov, Zh. Eksp. Teor. Fiz. **36**, 1853 (1959) [Sov. Phys. JETP **9,** 1321 (1959)].

[48] V. G. Veselago, Usp. Fiz. Nauk **92**, 517 (1967) [Sov. Phys. Usp. **10**, 509 (1968)].

[49] J. B. Pendry, A. J. Holden, W. J. Stewart, and I. Youngs, Phys. Rev. Lett. **76**, 4773 (1996).

[50] J. B. Pendry**,** A. J. Holden, D. J. Robbins, and W. J. Stewart, IEEE Trans. Microw. Theory Tech. **47**, 2075 (1999).

[51] A. Ishimaru, S.Lee, Y. Kuga, and V. Jandhyala, IEEE Trans. Ant. Prop. **51**, 2551(2003).

[52] P. A. Belov and C.R. Simovski, Phys. Rev. E **72**, 026615 (2005).

[53] W. Lamb, D. M. Wood, and N. W. Ashcroft, Phys. Rev. B **21**, 2248 (1980).

[54] D. Felbacq and G. Bouchitté, Opt. Lett. **30**, 1189 (2005).

[55] G.V. Eleftheriades and P.C. Kremer, IEEE Trans. Microw. Theo. Tech. **50**, 2703 (2002).

[56] M.G. Silveirinha and C.A. Fernandes, IEEE Trans. Ant. Prop. **53**, 59 (2005).

[57] M.G. Silveirinha and C.A. Fernandes, IEEE Trans. Microw. Theo. Tech. **53**, 1418 (2005).

[58] Mario G. Silveirinha, Phys. Rev. E **73**, 046612 (2006).

[59] Mario G. Silveirinha, Phys. Rev. B **75**, 115104 (2007).

[60] Mario G. Silveirinha, Phys. Rev. B **76**, 245117 (2007).

[61] J.T. Costa, M.G. Silveirinha, and S. I. Maslovski, Phys. Rev. B **80**, 235124 (2009).

[62] T.G. Mackay, A. Lakhtakia, and W.S. Weiglhofer, Phys. Rev E **62**, 6052 (2000).

[63] J.P. Eberhard, Phys. Rev. E **72**, 036616 (2005).

[64] W.L. Mochán and R.G. Barrera, Phys. Rev. B **32**, 4984 (1985).

[65] G. P. Ortiz, B. E. Martínez-Zérega, B. S. Mendoza, and W. L. Mochán, Phys. Rev. B **79**, 245132 (2009).

[66] C. Fietz and G. Shvets, Physica B **405**, 2930 (2010).

[67] R.M. Hornreich and S. Shtrikman, Phys. Rev. **171**, 1065 (1968).

[68] F. S. S. Rosa, D. A. R. Dalvit, and P. W. Milonni, Phys. Rev. A **78**, 032117 (2008).

[69] V. Cerdán-Ramírez, B. Zenteno-Mateo, M. P. Sampedro, M. A. Palomino-Ovando, B. Flores-Desirena, and F. Pérez-Rodríguez, J. Appl. Phys., **106**, 103520 (2009).

[70] V.M. Agranovich and V.L. Ginzburg, *Crystal Optics with Spatial Dispersion, and Exitons*, Springer Series in Solid State Sciences **42**, Springer-Verlag, Berlin, 1984.

[71] V. M. Agranovich, Y. R. Shen, R. H. Baughman, and A. A. Zakhidov, Phys. Rev. B **69**, 165112 (2004).

[72] R. Fuchs and P. Halevi, introductory chapter in *Spatial Dispersion in Solids and Plasmas*, ed. P. Halevi, North-Holland/Elsevier, Amsterdam, 1992.

[73] L.D. Landau and E.M. Lifshitz, *Statistical Physics* (Course of Theoretical Physics Vol. 5 by Landau and Lifshitz), Elsevier Butterworth-Heinemann, Oxford, UK, 1984.

[74] V. Amirkhizi and S. Nemat-Nasser, C. R. Mecanique **336**, 24 (2008).

[75] J. B. Pendry, AJ Holden, DJ Robbins, and WJ Stewart, J. Phys. Cond. Matt., **10**, 4785 (1998).

[76] Mario G. Silveirinha, Phys. Rev. B **79**, 035118 (2009).

[77] J.-M. Lourtioz, H. Benisty, V. Berger, J.-M. Gérard, D. Maystre, and A. Tchelnokov, *Photonic Crystals: Towards Nanoscale Photonic Devices,* Springer, 2005.

[78] P. Halevi, J. A. Reyes-Avendaño, and J. A. Reyes-Cervantes, Phys. Rev. E **73**, 040701R (2006).

[79] A. Maradudin and A. R. McGurn, J. of Mod. Opt. 41, 275 (1994).

[80] M. M. Sigalas, R. Biswas, K. M. Ho, and C. M. Soukoulis, Phys. Rev. B **58**, 6791(1998).

[81] Ph. Lalanne and H. Benisty, J. Appl. Phys. **89**, 1512 (2001).

[82] S. Foteinopoulou, A. Rosenberg, M. M. Sigalas and C. M. Soukoulis, J. Appl. Phys. **89**, 824 (2001).

[83] M. Qiu, and S. He, Phys. Lett. A **278**, 348 (2001).

[84] G. Alagappan, X. W. Sun, M. B. Yu, and P. Shum, Phys. Rev. B **75**, 113104 (2007).

[85] X.-P. Feng and Y. Arakawa, IEEE, J. Quantum Electron, **32**, 535 (1996).

[86] Z.-Y. Li and Y. Xia, Phys. Rev. B **64**, 153108 (2001).

[87] T. Haas, A. Hesse and T. Doll, Phys. Rev. B **73**, 045130 (2006).

[88] P. A. Belov, R. Marqués, S. I. Maslovski, I. S. Nefedov, M. Silveirinha, C. R. Simovski, and S. A. Tretyakov, Phys. Rev. B **67**, 113103 (2003).

[89] P. Halevi and F. Pérez-Rodríguez, Proc. SPIE, **6320**, 63200T (2006).

[90] J.A. Reyes-Avendaño, U. Algredo-Badillo, P. Halevi, and F. Pérez-Rodríguez, (submitted to New J. Phys.).

[91] X. Chen, B. Wu, J. Kong, and T. M. Grzegorczyk, Phys. Rev. E **71**, 046610 (2005).

[92] Aaswath Raman and Shanhui Fan, Phys. Rev. Lett. **104**, 087401 (2010).

[93] Zhongping Jian and Daniel M. Mittleman, Appl. Phys. Lett. **87**, 191113 (2005).

[94] S.G. Johnson, J.D. Joannopoulos, *Photonic Crystals – The Road from Theory to Practice*, Springer, 2002;

[95] S. Noda, T. Baba (Eds.), *Roadmap on Photonic Crystals*, Kluwer,2003;

[96] K. Busch, S. Lölkes, R.B. Wehrspohn, H. Fö ll (Eds.), *Photonic Crystals: Advances in Design, Fabrication, and Characterization*, Wiley, 2004;

[97] L. Liebert, *Liquid Crystals*, first ed., Academic, 1978;

[98] I.-C. Khoo, S.-T. Wu, *Optics and Nonlinear Optics of Liquid Crystals*, World Scientific, 1993;

[99] G.P. Crawford, S. Zumer (Eds.), *Liquid Crystals in Complex Geometries*, Taylor & Francis, 1996;

[100] S. Singh, *Liquid Crystals – Fundamentals*, World Scientific, 2002;

[101] M. Kleman, O.D. Lavrentovich, *Soft Matter Physics – An Introduction*, Springer, 2003.

[102] K. Busch, S. John, Phys. Rev. Lett. **83**, 967 (1999);

[103] S. John, K. Busch, J. Lightwave Technol. **17**, 1931 (1999).

[104] H.-S. Kitzerow, J.P. Reithaimer, Ref. [1, third part], Chapter 9, p.174.

[105] P.M. Fauchet, P.V. Braun (Eds.) Proceedings of the SPIE **5511**, p. 156 (2004).

[106] C.-S. Kee, H. Lim, Y.-K. Ha, J.-E. Kim, H.Y. Park, Phys. Rev. B **64**, 085114 (2001).

[107] H. Takeda, K. Yoshino, Phys. Rev. E **70**, 026601 (2004).

[108] C.-Y. Liu, L.-W. Chen, Phys. Rev. B **72**, 045133 (2005).

[109] H. Takeda, K. Yoshino, Phys. Rev. E **67**, 056607 (2003);

[110] G. Alagappan, X.W. Sun, P. Shum, M.B. Yu, Opt. Lett. **31**, 1109 (2006);

[111] G. Alagappan, X.W. Sun, M.B. Yu, P. Shum, D. den Engelsen, IEEE J. Quantum Elect. **42**, 404 (2006).

[112] M.J. Escuti, J. Qi, G.P. Crawford, Appl. Phys. Lett. **83**, 1131 (2003).

[113] T. Larsen, A. Bjarklev, D. Hermann, J. Broeng, Opt. Exp. **11**, 2589 (2003);

[114] T.T. Larsen, J. Broeng, D.S. Hermann, A. Bjarklev, Elec. Lett. **39**, 1719 (2003).

[115] F. Du, Y.-Q. Lu, S.-T. Wu, Appl. Phys. Lett. **85**, 2181 (2004).

[116] T. Alkeskjold, J. Laegsgaard, A. Bjarklev, D. Hermann, A. Anawati, J. Broeng, J. Li, S.-T. Wu, Opt. Exp. **12**, 5857 (2004).

[117] L. Scolari, T. Alkeskjold, J. Riishede, A. Bjarklev, D. Hermann, A. Anawati, M. Nielsen, P. Bassi, Opt. Exp. **13**, 7483 (2005).

[118] K. Yoshino, Y. Shimoda, Y. Kawagishi, K. Nakayama, M. Ozaki, Appl. Phys. Lett. **75**, 932 (1999).

[119] D. Kang, J.E. Maclennan, N.A. Clark, A.A. Zakhidov, R.H. Baughman, Phys. Rev. Lett. **86**, 4052 (2001);

[120] Q.-B. Meng, C.-H. Fu, S. Hayami, Z.-Z. Gu, O. Sato, A. Fujishima, J. Appl. Phys. **89**, 5794 (2001).

[121] G. Mertens, T. Röder, R. Schweins, K. Huber, H.-S. Kitzerow, Appl. Phys. Lett. **80**, 1885 (2002).

[122] S. Gottardo, M. Burresi, F. Geobaldo, L. Pallavidino, F. Giorgis, D.S. Wiersma, Phys. Rev. E **74**, 040702(R) (2006).

[123] M.J. Escuti, J. Qi, J.P. Crawford, Opt. Lett. **28**, 522 (2003).

[124] Y.-Ki. Ha, Y.-C. Yang, J.-E. Kim, H.Y. Park, C.-S. Kee, H. Lim, J.-C. Lee, Appl. Phys. Lett. **79**, 15 (2001).

[125] C. Schuller, F. Klopf, J.P. Reithaimer, M. Kamp, A. Forchel, Appl. Phys. Lett. 82, **2767** (2003).

[126] H. Takeda, K. Yoshino, Phys. Rev. E **68**, 046602 (2003).

[127] H. Takeda, K. Yoshino, Phys. Rev. B **67**, 073106 (2003).

[128] B. Maune, M. Loncar, J. Witzens, M. Hochberg, T. Baehr-Jones, D. Psaltis, A. Scherer, Y. Qiu, Appl. Phys. Lett. **85**, 360 (2004).

[129] S.V. Burylov, Zh. Eksp. Teor. Fiz. **112**, 1603 (1997); S.V. Burylov, JETP **85**, 873 (1997).

[130] J.L. Troutman, *Variational Calculus and Optimal Control*, second ed., Springer, NY, 1996, p. 60.

[131] Willian H. Press et al., Numerical Recipes: *The Art of Scientific Computing*, Cambridge, 1986.

[132] G.P. Crawford, D.W. Allender, J.W. Doane, Phys. Rev. A **45**, 8693 (1992).

[133] C.M. Bender, M.C. Arszog, *Advanced Mathematical Methods for Scientists and Engineers*, McGraw-Hill, New York, 1978.

[134] R.M. Hornreich, S. Shtrikman, C. Sommers, Phys. Rev. E **47**, 2067 (1993).

[135] Y. Shimoda, M. Ozaki, and K. Yoshino, Appl. Phys. Lett. **79**, 3627(2001).

[136] Dennis McPhail, Martin Straub, and Min Gu, Appl. Phys. Lett. **86**, 051103 (2005).

[137] M. Haurylau, S. P. Anderson, K. L. Marshall and P. M. Fauchet, Appl. Phys. Lett. **88**, 061103 (2006).

[138] J.A. Reyes-Cervantes, J.A. Reyes-Avendaño, and P. Halevi, Opt. Commun., **281**, 2535(2008).

[139] P. Halevi, A.A. Krokhin, and J. Arriaga, Appl. Phys. Lett. **75**, 2725(1999).

[140] Iam-Choon Khoo and Shin-Tson Wu, (World Scientific 1993).

[141] I. H. Malitson, J. Opt. Soc. Am. A. **55**, 10(1965).

[142] J. Manzanares-Martínez, F. Ramos-Mendieta and, P. Halevi, Phys. Rev. B **72**, 035336 (2005).

[143] V. Kuzmiak, A. A. Maradudin, and F. Pincemin, Phys. Rev. B **50**, 16835 (1994).

[144] J.A. Reyes-Avendaño and P. Halevi, “Mean-field description of two-dimensional photonic crystals: Axial propagation.” (in preparation)

[145] J.A. Reyes-Avendaño and P. Halevi, Rev. Mex. Fís. **54**(6), 407-410(2008).